Simulation and characterization of the RF system and global stability analysis at the REGAE linear electron accelerator

Master thesis
by
Frank Mayet

Universität Hamburg
Department Physik
30. Oktober 2012

Gutachter: Prof. Dr. Florian Grüner
Zweitgutachter: Dr. Klaus Flöttmann

Abstract

LAOLA (**LA**boratory f**or** **L**aser- and beam-driven plasma **A**cceleration), is a collaboration between groups from DESY and the University of Hamburg. Its mission is to complement basic research in the relatively new field of plasma wakefield acceleration (PWA) by an explicit combination with DESY's conventional, modern accelerators.

The linear electron accelerator REGAE is designed to produce sub 10 fs low charge electron bunches with ultra-low emittance at a repetition rate of 50 Hz. The planned experiments include femtosecond electron diffraction (R.J. Dwayne Miller), as well as the probing of laser induced plasma wakefields with well characterized bunches (LAOLA). They all require high bunch time of flight stability down to 10 fs. The REGAE machine consists of two RF cavities, both fed by a single klystron. While the first one — the gun cavity — is used for acceleration of the electrons, the second one — the buncher cavity — can be used to reduce the electron bunch length. This scheme only works for a specific RF phase relation between the two cavities.

This thesis is split into two parts. In the first one the implications of the unique two cavity design on day-to-day machine operation are analyzed. To this end an analytical model of the RF system is developed, which is necessary for understanding how to individually adjust the cavity phases. In the second part the influence of the setup on time of flight stability is discussed with an emphasis on phase jitter compensation. RF phase stability measurements reveal that the current machine setup allows for a time of flight stability down to 50 fs right after the gun.

Zusammenfassung

LAOLA (**LA**boratory f**o**r **L**aser- and beam-driven plasma **A**cceleration) ist eine Kollaboration zwischen Gruppen des DESY und der Universität Hamburg. Ihre Aufgabe ist es, die Grundlagenforschung im relativ neuen Feld der Plasma Wakefield Beschleunigung (PWA) durch Kombination mit DESYs konventionellen, modernen Beschleunigern zu ergänzen.

Das Design des Elektronenbschleunigers REGAE sieht die Erzeugung von sub 10 fs Elektronenpaketen mit niedriger Ladung und Emittanz bei einer Frequenz von 50 Hz vor. Die geplanten Experimente beinhalten *Femtosekunden Elektronenbeugung* (R.J. Dwayne Miller), sowie das Abtasten einer lasererzeugten Plasmawelle (LAOLA). Für die Experimente ist eine Flugzeitstabilität der Elektronenpakete von bis zu 10 fs notwendig. Die REGAE Maschine beeinhaltet zwei HF Kavitäten, welche beide von einem einzigen Klystron gespeist werden. Während die erste — die Gun Cavity — zur Beschleunigung der Elektronen eingesetzt wird, kann die zweite — die Buncher Cavity — zur Reduktion der Länge der Pakete eingesetzt werden. Dies funktioniert nur für eine bestimmte HF Phasenbeziehung zwischen den zwei Kavitäten.

Diese Arbeit ist in zwei Teile aufgeteilt. Im ersten Teil werden die Implikationen der Implementation zweier Kavitäten im Bezug auf den alltäglichen Betrieb analysiert. Zu diesem Zweck wird ein theoretisches Modell des HF Systems entwickelt, welches zum Verstehen der individuellen Einstellung der Phasen notwendig ist. Im zweiten Teil wird der Einfluss des Aufbaus auf die Flugzeitstabilität mit Schwerpunkt auf eine Phasenjitterkompensation diskutiert. HF Phasenstabilitätsmessungen zeigen, dass der aktuelle Maschinenaufbau eine Flugzeitstabilität von 50 fs direkt hinter der Gun erlaubt.

Contents

List of Figures

List of Tables

1

Introduction

The linear electron accelerator REGAE is designed to produce sub 10 fs low charge electron bunches with ultra-low emittance at a repetition rate of 50 Hz. These specifications allow for time resolved detection of transition states in complex chemical systems via femtosecond electron diffraction, which could be an important step towards recording chemical reactions at their characteristic time scales. In addition to that, the bunch parameters permit the external injection of electrons into laser induced plasma wakefields. Even though plasma wakefields can nowadays be simulated using sophisticated particle-in-cell codes, direct measurement of the wakefield properties is difficult. The external injection of well characterized electron bunches into a laser induced plasma wakefield as a means to probe the wakefield structure is one of the main goals of the REGAE experiment. One of the main challenges at REGAE is to achieve the required $\sim$10 fs electron bunch time of flight stability.

In order to be able to provide the required bunch parameters and timing stability, a deep understanding of the RF system is necessary. At REGAE the high power RF system consists of a 1.5 cell gun cavity and a four cell buncher cavity, which are both fed by a single klystron. The subject of this thesis is to investigate the behavior of this unique RF setup, as well as to perform a global stability analysis. In order to do so, this thesis is split into three chapters, where the first one will give a short introduction to the REGAE facility and the two main experiments. The remaining two chapters will then focus on the main topics of this thesis and will be followed by a short outlook that will be focusing on stating the current status of the REGAE accelerator and possible optimizations in terms of stability.

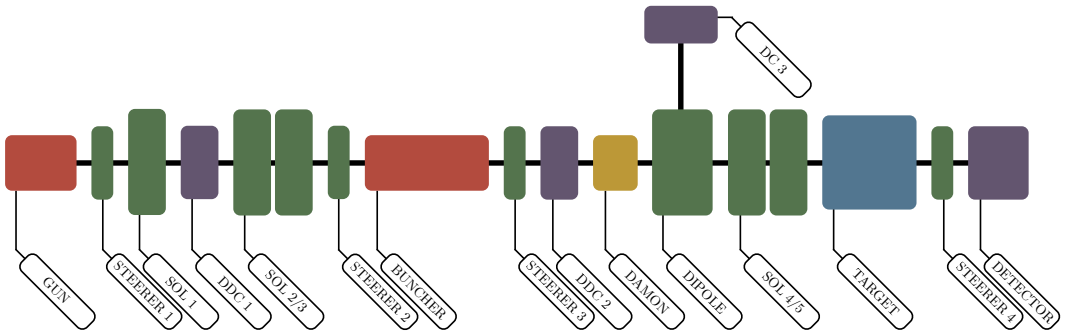

Figure 1.1: Schematic of the REGAE linear electron accelerator.

1.1 REGAE

The REGAE (**R**elativistic **E**lectron **G**un **F**or **A**tomic **E**xploration) machine is a small linear electron accelerator situated at the DESY campus in Hamburg. It is mainly comprised of an S-band (3 GHz) 1.5 cell standing-wave RF gun and an additional S-band 4 cell standing-wave buncher cavity. A simple schematic of the experimental assembly can be seen in figure 1.1. The RF system feeds the cavities with up to 6 μs long RF pulses with a design repetition rate of 50 Hz. Its unique features compared to other RF systems will be discussed in detail in chapter 2. In order to inject the electrons into the gun cavity the 266 nm harmonic of a pulsed Ti:Sapphire laser is directed onto a Cesium Telluride (Cs_2Te) photo cathode, which is situated at the back of the gun cavity. Electrons are then emitted into the RF-field at a phase, where the electrons are accelerated most efficiently (*on-crest*). It is immediately clear that this injection process can only be performed successfully, if both the laser and the RF pulses are synchronized. Knowing this, it is also clear that the properties of the electron bunch distribution crucially depend on the stability and properties of both the laser and the RF parameters at the time of injection. This circumstance will be discussed in more detail in chapter 3. Successfully accelerated electrons then pass several beam optics components (see figure 1.1). At REGAE there are three different kinds of beam optics elements:

- Single solenoid
- Double solenoid
- Steerer magnets

Solenoids act like lenses in an optical setup and the focusing strength is proportional to the integral over the squared magnetic field strength. The main difference

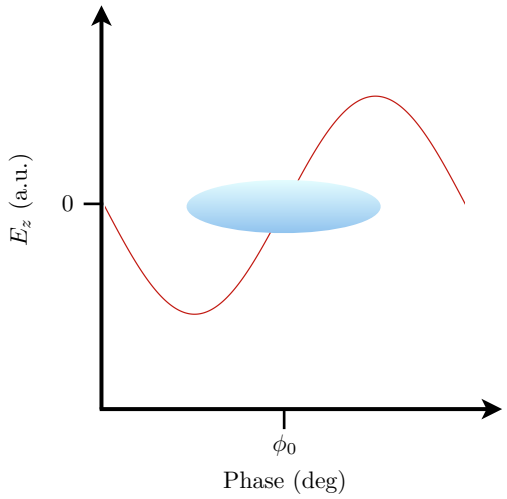

Figure 1.2: Schematic of the velocity bunching scheme. The electron bunch is depicted by the light blue ellipse. Electrons in the front of the bunch arrive at a lower phase, where they are decelerated by the E_z of the buncher cavity. Electrons in the back of the bunch arrive at a higher phase and are thus accelerated.

to an optical lens is the fact that due to radial components of the magnetic field the electrons are in fact focused, but also rotated around the longitudinal axis of the solenoid. Using a second solenoid with reversed field direction, one can circumvent this problem, as the electrons are then rotated back to their initial position. This works under the assumption that the offset between the electron beam and the longitudinal axis of the solenoid is sufficiently small (*paraxial approximation*). In this case only linear forces act on the particles. Another means to affect the electron beam orbit are so called steerer magnets. At REGAE the steerer magnets described in [2] are being used, which are basically two small dipole magnets that are arranged orthogonally and can impose a field strength dependent kick onto the passing electrons. These steerers are for example used to avoid the problems explained above (i.e. compensating alignment errors and therefore entering a solenoid on-axis), or to steer the electron beam onto a specific target. Having passed these beam optics, the electrons then enter the buncher cavity. It has been stated above that in order to get optimal acceleration (this will also be discussed in more detail in chapter 3) the electrons have to be injected *on-crest*. For maximum bunching inside the buncher cavity the electrons have to be injected *off-crest* into the so called *bunching phase*, i.e. the phase where the field has its zero-crossing. The underlying concept is the so called *velocity bunching scheme* ([3]). Electrons

in the front of a bunch arrive at a phase where they are decelerated, whereas electrons in the back arrive at a phase, where they are accelerated (see figure 1.2). This way an additional energy spread is imposed onto the electron bunch and after a certain distance the electron bunch length reaches a minimum due to the fact that the accelerated electrons in the back of the bunch now overtake the decelerated electrons in the front. It is now easy to understand why the electron bunch length increases again after having reached its minimum. The design minimum bunch length for REGAE is 7 fs RMS (cf. [4]). In addition to the experimental

Figure 1.3: Photo of the REGAE linear electron accelerator. On the left: the target chamber, on the right: the accelerator section.

setup itself, the REGAE assembly also contains five diagnostics stations (DDC1, DDC2, DC3, TARGET and DETECTOR). The first three feature a Faraday cup for charge measurements and a motorized LYSO scintillator screen that can be looked at using a CCD camera. DC3 includes a dipole magnet that bends the electron orbit according to the electron energy and thus can be used as a dispersive element for energy and energy spread measurements. The detector, which is situated at the far end of the beam line includes a highly sensitive scintillator screen that can detect single electrons ([5]) when being cooled down in order to suppress noise. All of the screens are motorized. As the charge measurement using a Faraday cup is destructive (i. e. the diagnostics interrupts normal operation), the REGAE beam line also incorporates a so called non-invasive *DaMon* (dark current monitor) cavity. Every electron bunch that is directed through the DaMon cavity induces a voltage that can be related to the bunch charge.

1.2 Experiments at the REGAE Facility

In this section an overview of the two main experiments that will be conducted at the REGAE facility will be given. The main motivation to build the REGAE accelerator, is the notion of recording the so called *molecular movie* using femtosecond electron diffraction, as it has been proposed by Dwayne Miller et al. in [6] in 2006. The second experiment will be conducted by the LAOLA collaboration between DESY and the University of Hamburg. Here the properties of a plasma wakefield excited by a high power laser are probed by the well characterized REGAE electron bunch. This concept is called *external injection scheme*.

1.2.1 Femtosecond Electron Diffraction

One of the main goals at REGAE is to use the ultra-short electron bunches for *femtosecond electron diffraction* (FED) experiments. FED enables the time resolved detection of transition states in complex chemical systems ([6]), which is often also paraphrased as "making the molecular movie". The main advantage of this method compared to molecular beam techniques for example is the fact that FED captures reactions inside a three-dimensional volume. This way multiple reaction coordinates inside a complex chemical system can be taken into account. Through the use of relativistic electrons, atomic resolution is possible. The timescale of two atoms moving approximately one bond length inside a molecular system is on the order of 100 fs ([6]). This defines the minimal time resolution requirement for conducting a time resolved measurement and with that defines the limits of pulse length and timing jitter, which need to be well below this threshold. Both X-ray and electron pulses are suitable for these kind of spatial and temporal requirements, but electrons have the advantage of a six orders of magnitude larger scattering cross-section ([7]). This is because X-rays are only scattered by the electron distribution of the sample (*Thompson scattering*), whereas electron are scattered by both the electron distribution and the atomic nuclei (*Coulomb scattering*). This leads to improved contrast in the resulting diffraction patterns and the possibility reduce the pulse length in order to improve the temporal resolution. In addition to that, electrons cause less damage to the samples, as the inelastic to elastic scattering ratio is much less compared to X-ray pulses ([7]). This is important for the study of fragile biological samples.

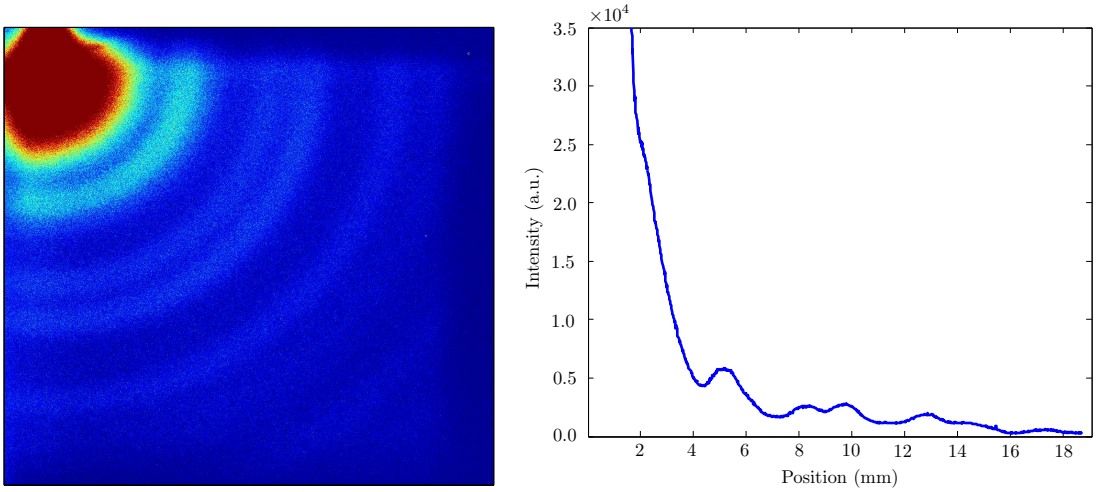

Figure 1.4: One of the first diffraction patterns detected at REGAE. The pattern has been recorded using a gold 50 nm sample at 4.1 MeV mean beam energy. The plot on the right shows the angular integration of the image. *Data courtesy of Stephanie Manz (CFEL Hamburg)*

1.2.2 External Injection of Electrons into a Plasma Wakefield

In plasma accelerators electrons are accelerated inside a so called *plasma wakefield*, which is created either by a high power laser pulse (*laser driven*), or an electron beam (*beam driven*). One of the most important questions in plasma accelerator physics is the actual structure of the plasma wakefield. Plasma wakefields can be simulated using so called *particle-in-cell* codes, but direct measurement of the fields is difficult. One way to overcome this problem and to gain more knowledge on the actual field distributions inside the plasma wake is the so called *external injection scheme* ([8]). Here a well characterized electron bunch is injected into a plasma wakefield in order to study the electron beam dynamics. The effect of the plasma wakefield on the bunch parameters of the previously injected electrons (like emittance) can be used to infer the wakefield structure. The wakefield can then be mapped by varying the time delay between the externally injected electron bunches and the laser pulse that excites the wakefield inside the plasma. Figure 1.5 shows a simulation of a quasi linear plasma wakefield. One of the main challenges at REGAE is to achieve the required ~ 10 fs synchronization of the drive laser to the electron beam.

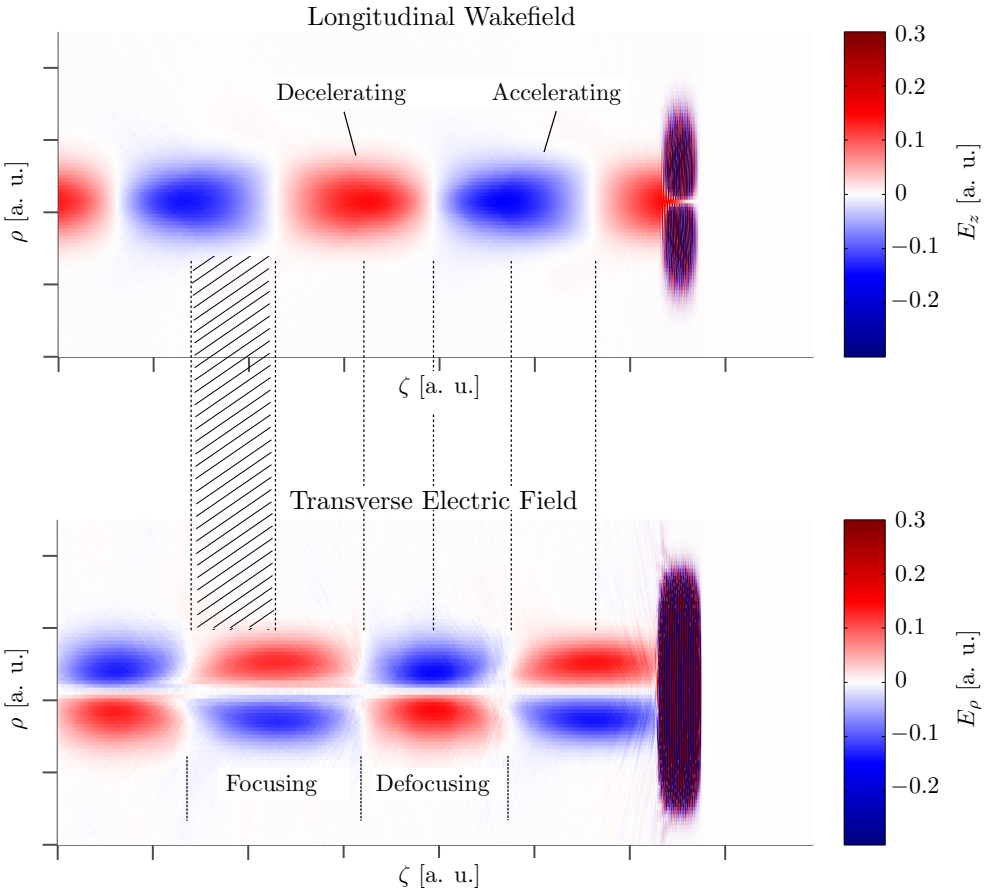

Figure 1.5: Simulation of a quasi linear plasma wakefield. The shaded area marks the part of the wake, where electrons are both accelerated and focused. *Figure courtesy of Benno Zeitler (CFEL Hamburg)*

2

The REGAE RF System

In this chapter the REGAE high power RF (*radio frequency*) system will be discussed in more detail. The first part will give a short introduction into the relevant microwave circuit and cavity/resonator theory. Then the unique setup at REGAE is discussed and a simple yet powerful analytical model based on the scattering matrix formalism will be developed in order to gain a deeper understanding as to how the RF system behaves in operation. An algorithm for arbitrary and independent phase control for both cavities based on the analytical model will also be proposed. In addition to that, numerical simulations using *CST Microwave Studio* ([9]) will be presented and compared to actual measurements. The goal of this chapter is to provide an extensive overview of the REGAE high power RF system, as well as a usage guide for operators.

2.1 Microwave Circuit and Resonator Theory

In order to understand the behavior and the functionality of the RF system, it is important to quickly summarize the fundamental concepts of waveguides and resonators. Starting from *Maxwell's equations* the most important equation can be derived, which is the *wave equation* for the electric and the magnetic field ([10]). Assuming $\nabla \cdot \mathbf{E} = 0$ (i. e. charge-free space) the wave equations then read:

$$\begin{aligned} \Delta\mathbf{E} - \frac{\epsilon_r \mu_r}{c^2} \cdot \partial_t^2 \mathbf{E} = 0 \\ \Delta\mathbf{H} - \frac{\epsilon_r \mu_r}{c^2} \cdot \partial_t^2 \mathbf{B} = 0. \end{aligned} \tag{2.1}$$

Also assuming free space and wave propagation in z direction, we then get the plane wave solution

$$E_\perp = E_0 \cdot \exp[i(\omega t - kz)], \tag{2.2}$$

where $k = \sqrt{\epsilon_r \mu_r} \cdot \omega/c$. The fact that in this case $\partial_x = \partial_y = 0$ has also been used. It has to be noted that these plane waves do not have electrical field components in the direction of propagation, which is a necessary condition for successful particle acceleration. This problem can be avoided by imposing proper boundary conditions as it will be described in the following section.

2.1.1 Rectangular Waveguide

In order to find solutions with non-zero longitudinal field components, let us first consider boundary conditions in the form of metallic boundaries, as it is the case for rectangular waveguides. Let $E_z = F_x(x) \cdot F_y(y) \cdot F_z(z)$ be a non-zero combination of functions that obey equation 2.1. Inserting this ansatz into the wave equation gives:

$$\begin{aligned}
\Delta E_z - \frac{\epsilon_r \mu_r}{c^2} \cdot \partial_t^2 E_z &= 0 \\
\nabla \begin{pmatrix} \partial_x F_x(x) \cdot F_y(y) \cdot F_z(z) \\ F_x(x) \cdot \partial_y F_y(y) \cdot F_z(z) \\ F_x(x) \cdot F_y(y) \cdot \partial_z F_z(z) \end{pmatrix} &= -k^2 (F_x(x) \cdot F_y(y) \cdot F_z(z)) \\
\frac{\partial_x^2 F_x(x)}{F_x(x)} + \frac{\partial_y^2 F_y(y)}{F_y(y)} + \frac{\partial_z^2 F_z(z)}{F_z(z)} &= -k^2.
\end{aligned}$$

From this it is easy to see, since k is constant that every term on the l.h.s. must be constant as well and therefore

$$k^2 \equiv k_x^2 + k_y^2 + k_z^2. \tag{2.3}$$

With the definition $k_c^2 = k_x^2 + k_y^2$ it follows that $k_z = \sqrt{k^2 - k_c^2}$. The phase velocity of the longitudinal electric field component is then given by

$$v_{ph} = \frac{\omega}{k_z} = \frac{\omega}{\sqrt{k^2 - k_c^2}}. \tag{2.4}$$

If $k_c > k$, the phase velocity becomes imaginary, which leads to an exponential decay of E_z, or a so called *evanescent wave*. This is why k_c is called the *cut-off wavenumber*. Let us now try to relate the cut-off wavenumber to geometrical properties of a rectangular waveguide with metallic boundaries (see figure 2.1). Having metallic boundaries leads to the condition that the tangential components

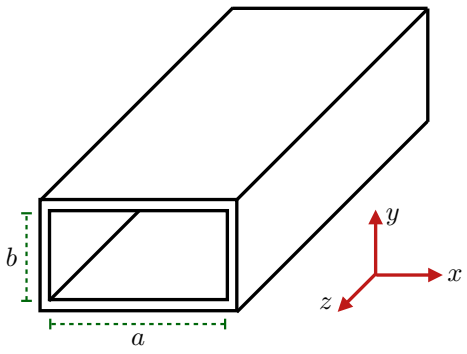

Figure 2.1: Schematic of a rectangular waveguide.

of the electric field must vanish. Thus only cosine functions can be correct solutions for $F_x(x)$ and $F_y(y)$. The final solution for the longitudinal electric field is now given by

$$E_z = E_0 \cos\left(\frac{m\pi x}{a}\right) \cos\left(\frac{n\pi y}{b}\right) \exp[i(\omega t - k_z z)], \tag{2.5}$$

where $m, n \in \mathbb{N}$ define the so called *transverse field modes* (since the system is now subject to boundary conditions, only discrete solutions are allowed). The solution for the magnetic field component reads

$$B_z = B_0 \sin\left(\frac{m\pi x}{a}\right) \sin\left(\frac{n\pi y}{b}\right) \exp[i(\omega t - k_z z)]. \tag{2.6}$$

Having found these solutions and recalling that $k_c^2 = k_x^2 + k_y^2$, it can now be seen that

$$k_c = \sqrt{\left(\frac{m\pi}{a}\right)^2 + \left(\frac{n\pi}{b}\right)^2}, \tag{2.7}$$

which can be used to determine the cut-off frequency (or wavelength) of a particular waveguide mode. Using the wave equation 2.1 and the solutions 2.5 and 2.6, it is possible to write down E_x and E_y in terms of E_z. Inserting the solutions we get:

$$\begin{aligned} E_x &= i(k_z \partial_x E_z + c k_0 \partial_y B_z)/(k_z^2 - k^2), \\ E_y &= i(k_z \partial_y E_z - c k_0 \partial_x B_z)/(k_z^2 - k^2), \\ B_x &= i(c k_z \partial_x B_z - \epsilon\mu k_0 \partial_y E_z)/c(k_z^2 - k^2), \\ B_y &= i(c k_z \partial_y B_z + \epsilon\mu k_0 \partial_x E_z)/c(k_z^2 - k^2), \end{aligned} \tag{2.8}$$

where $k_0 = \omega/c$ is the vacuum wavenumber. Looking at equation 2.8 three fundamental classes of field configurations can be distinguished:

(1) $E_z = 0$ TE$_{mn}$-modes (*transverse electric*)

(2) $B_z = 0$ TM$_{mn}$-modes (*transverse magnetic*)

(3) $E_z = B_z = 0$ TEM$_{mn}$-modes (*transverse electromagnetic*)

Since $E_z = 0$ for TE- and TEM-modes, it is clear that the most important modes for particle acceleration are TM-modes. The indices m, n can be understood physically as the number of half-wavelengths along the $x-$ and $y-$axis respectively. From equation 2.5 it follows that the lowest TM-mode is the TM$_{11}$ mode. Figure 2.2 shows the field configuration for two modes in a rectangular waveguide. It is now possible to calculate all possible modes in a particular rectangular waveguide. A sample calculation can be seen in table 2.1. Every waveguide has a so called *dominant mode*. The dominant mode is the mode with the smallest cut-off frequency, or in other words the mode which supports the broadest range of frequencies. For rectangular waveguides the TE$_{10}$ is the dominant mode, which can be seen from equation 2.7 (TE$_{11}$ for cylindrical waveguides, see below). Another

Table 2.1: TM-modes for a rectangular waveguide with $a = 7.0\,\text{cm}$ and $b = 3.2\,\text{cm}$, which corresponds to a WR-284 S-band waveguide (EIA (The Electronic Industries Alliance) specifications). The cut-off frequency has been calculated using equation 2.7 and the assumption that the wave travels in vacuum.

m	n	$f_{c,mn}$ (GHz)
1	1	5.15
1	2	9.61
2	2	10.3

important quantity for rectangular waveguides is the *waveguide wavelength* λ_g. From the usual definition $\lambda = 2\pi/k$ we get:

$$\lambda_g = \frac{2\pi}{k_z} = \frac{2\pi}{\sqrt{k^2 - k_c^2}}. \tag{2.9}$$

It is important to note that $\lambda_g > \lambda$, where λ is the free space wavelength.

2.1.2 Cylindrical Waveguide

At REGAE (as it has been stated in chapter 1) the electrons are accelerated using a standing-wave 1.5 cell RF cavity. Since this cavity, as well as the buncher

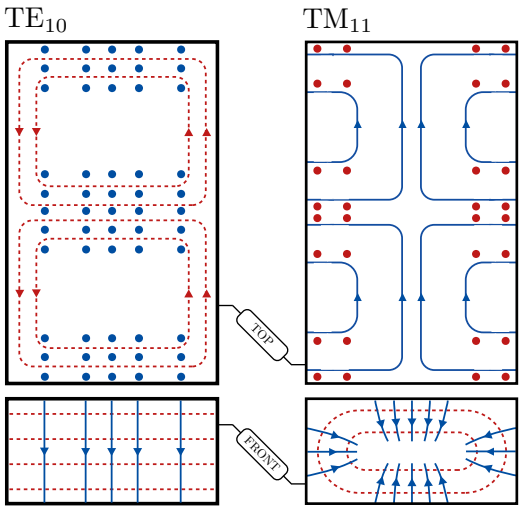

Figure 2.2: Electric and magnetic field configuration of the TE_{10} and TM_{11} mode in a rectangular waveguide. The blue solid lines depict the electric field lines and the red dashed lines the magnetic field lines. The top view is a cut through the waveguide at $y = b/2$ as defined in figure 2.1.

cavity are cylindrical, it is useful to quickly review the waveguide quantities that have been derived above for cylindrical waveguides. For the derivation of these properties it makes sense to switch to cylindrical coordinates. As a matter of fact this is the only difference, which has to be taken into account. The wave equation for the z-component in cylindrical coordinates is given by

$$\partial_r^2 E_z + \frac{\partial_r E_z}{r} + \frac{\partial_\phi^2 E_z}{r^2} + \partial_z^2 E_z + \frac{\epsilon_r \mu_r}{c^2} E_z = 0. \tag{2.10}$$

The solution of the equation can be found using Bessel's functions of the first kind $J_\alpha(x)$ in integer order (cylindrical symmetry):

$$E_z = E_0 J_m(k_c r) \exp[i(\omega t - m\phi - k_z z)]. \tag{2.11}$$

Due to metallic surfaces, the boundary condition is $E_z = 0$ at the boundary of the waveguide. Looking at the solution, it is clear that in order to satisfy this condition at all times, it is necessary to find the roots of the Bessel functions $J_\alpha(k_c a)$, where a is the radius of the waveguide pipe. This also defines the cut-off wavenumber, which now depends on the radius of the waveguide in a way that waves with a wavelength smaller than the pipe diameter cannot be guided. The cut-off wavenumber for TM modes is now defined as

$$k_c = \frac{j_{\alpha,\beta}}{a}, \tag{2.12}$$

where $j_{\alpha,\beta}$ is the β-th root of the Bessel function of the first kind of order α. Therefore the modes for cylindrical waveguides are now called $\mathrm{TE}_{\alpha,\beta}$ and $\mathrm{TM}_{\alpha,\beta}$. Physically the two indices describe the number of half-wavelengths along one half-circumference (α) and the radius (β) respectively. Figure 2.3 shows the field configuration for two modes in a cylindrical waveguide.

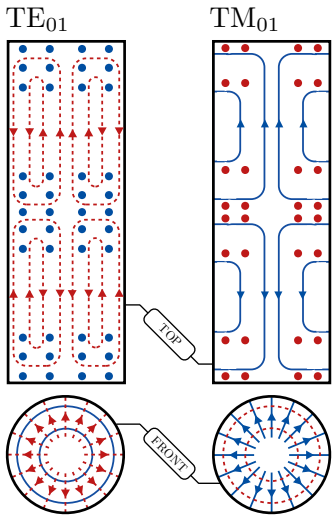

Figure 2.3: Electric and magnetic field configuration of the TE_{01} and TM_{01} mode in a cylindrical waveguide. The blue solid lines depict the electric field lines and the red dashed lines the magnetic field lines. The top view is a cut through the waveguide at $a = 0$.

2.1.3 Standing Wave Cavity

Since for both the rectangular and the cylindrical waveguides the phase velocity v_{ph} exceeds the speed of light, both structures are not suitable for particle acceleration, because the particles would be overrun by the wave. One way to overcome this problem is to use standing waves in an (in the case of REGAE) cylindrical RF cavity (or *pillbox cavity*). The simplest cavity resonator would be a waveguide with a short circuit termination at each end. In the ideal case the walls are perfect conductors, which leads to the boundary conditions that have also been used above: Electrical field lines end perpendicular to the cavity walls and the magnetic field lines are parallel close to the walls. If $L = p \cdot \lambda_g/2$, where L is the cavity length, $p \in \mathbb{N}$ and λ_g the guide wavelength as defined in equation 2.9, the condition for standing waves is fulfilled and the z-component of the electric field is then a superposition of E_z and E_{-z} from equation 2.11. Due to the fact that

the system is now bounded in the z-direction, an additional index is added to the mode specification. For a cylindrical cavity the modes are now called $\mathrm{TE}_{\alpha\beta p}$ and $\mathrm{TM}_{\alpha\beta p}$. The so called HEM (hybrid EM) modes are superpositions of the two. All of the modes are now characterized by their azimuthal (α), radial (β) and longitudinal (p) field configuration. In accelerator physics the usual nomenclature for the azimuthal modes is *monopol* ($\alpha = 0$), *dipole* ($\alpha = 1$), *quadrupole* ($\alpha = 2$) and so on ([11]).

Taking the resonance condition $L = p \cdot \lambda_g/2$, it is possible to calculate the resonant frequencies for TM modes of a cylindrical single cell cavity in the following way. Noticing that

$$\lambda_g = \frac{2L}{p} = \frac{2\pi}{\sqrt{k_r^2 - k_c^2}}, \tag{2.13}$$

where equation 2.9 has been used, it is possible to solve for k_r, which is the wavenumber that fulfills the resonance condition:

$$k_r^2 = \frac{\pi^2 p^2}{L^2} + k_c^2. \tag{2.14}$$

Inserting equation 2.12 yields

$$f_r = \frac{c}{2\pi} \cdot \sqrt{\frac{j_{\alpha\beta}^2}{a^2} + \frac{\pi^2 p^2}{L^2}}. \tag{2.15}$$

For TM-modes the special case $p = 0$ is the case where E_z has no longitudinal dependence. This implies that the resonant frequency — in this case — does not depend on the length of the cavity. Therefore for this special case

$$f_r(\mathrm{TM}_{\alpha\beta 0}) = \frac{c}{2\pi} \cdot \sqrt{\frac{j_{\alpha\beta}^2}{a^2}}. \tag{2.16}$$

The lowest monopole mode is called the *fundamental mode* and in the case of a cylindrical single cell cavity it is the TM_{010} mode (see figure 2.4). Setting $\alpha = 0$, $\beta = 1$ and $p = 0$, the resonant frequency of this mode can readily be computed using equation 2.15 and $j_{0,1} = 2.4048$:

$$f_r(\mathrm{TM}_{010}) = \frac{c}{2\pi} \cdot \frac{2.4048}{a}. \tag{2.17}$$

So in order to build an S-band TM_{010} resonator cavity, the radius of the cavity would need to be $a_{3\mathrm{GHz}} = 3.83\,\mathrm{cm}$ (REGAE: $a = 3.93\,\mathrm{cm}$). All other modes except for the fundamental mode are called HOMs, or *higher order modes*. These modes

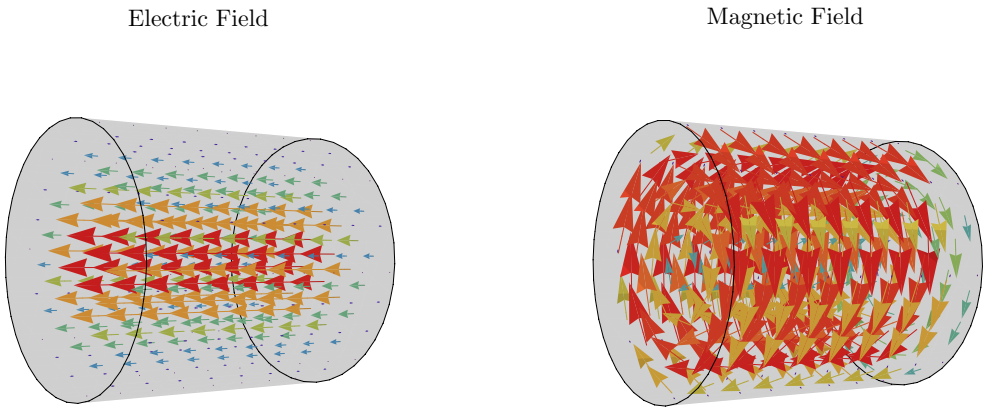

Figure 2.4: Numerical simulation of the TM_{010} mode for a cylindrical single cell cavity.

are not desirable for particle acceleration, because they can lead to deflection of particles due to their azimuthal fields. Even without exciting them actively they can however be excited by the electron beam itself. The REGAE gun cavity is a 1.5 cell resonator cavity, which means that a single and a half cell are coupled to form one cavity. This half cell configuration has been developed to enable the injection of the electrons that are created at the photo cathode into the maximum of the field (see section 2.6.4 for field measurements). Newly emitted electrons have to be accelerated first to an energy where they are synchronized with the field. During this period phase slippage occurs and the electrons are not accelerated properly. It can be shown that the electrons are synchronized with the field after the first cell ([12]). Inside of the second cell the electrons now do not experience phase slippage any more and are thus accelerated properly. This system of coupled cavities can be understood as two coupled electrical resonators. The equivalent circuit is shown in figure 2.5. As a result of this coupling, the azimuthal modes are now split into

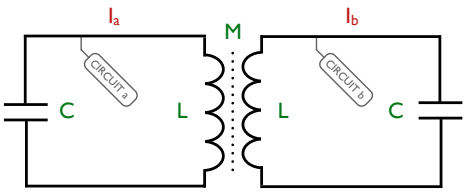

Figure 2.5: Simple equivalent circuit for two coupled resonator cavities.

$N+1$ sub-modes, where $N+1$ is the number of coupled resonator cavities. The usual nomenclature in accelerator physics is to add the phase advance between each cell in multiples of π to the original azimuthal mode specification ([11]). So the fundamental modes of a system of two coupled cylindric resonator cavities would now be the TM_{010} 0 mode and the TM_{010} π mode. The latter is often simply called the *monopole π mode*. So why does this splitting occur? Assuming that both cells have the same resonant frequency $\omega_{0,1} = \omega_{0,2} = \omega_0$ (and therefore $L_1 = L_2 = L$ and $C_1 = C_2 = C$), the system can be analyzed easily using *Kirchoff's law*. Referring to figure 2.5 we get for circuit a and b:

$$\left(\sum U\right)_{a/b} = I_{a/b}(i\Omega L) + \frac{I_{a/b}}{i\Omega C} + I_{b/a}(i\Omega M) = 0, \tag{2.18}$$

where $M = k \cdot \sqrt{L_1 L_2} = k \cdot L$ is the mutual inductance between the two circuits and $k \in [0,1]$ is the *coupling coefficient* of the two circuits. This can be simplified the following way:

$$\begin{aligned} & I_{a/b}(i\Omega L) + \frac{I_{a/b}}{i\Omega C} + I_{b/a}(i\Omega M) = 0 \\ \iff & I_{a/b}\left(\Omega L - \frac{1}{\Omega C}\right) + I_{b/a}\Omega M = 0 \\ \iff & I_{a/b}\left(1 - \frac{1}{\Omega^2 LC}\right) + I_{b/a}\frac{M}{L} = 0 \\ \iff & I_{a/b}\left(1 - \frac{\omega_0^2}{\Omega^2}\right) + I_{b/a}k = 0 \end{aligned} \tag{2.19}$$

where $\omega_0 = 1/\sqrt{LC}$ for electrical circuits. This set of equations can be brought into matrix form which leads to the following eigenvalue problem

$$\begin{pmatrix} 1/\omega_0^2 & k/\omega_0^2 \\ k/\omega_0^2 & 1/\omega_0^2 \end{pmatrix} \cdot \begin{pmatrix} I_a \\ I_b \end{pmatrix} = \frac{1}{\Omega^2} \cdot \begin{pmatrix} I_a \\ I_b \end{pmatrix} \tag{2.20}$$

with eigenvalues

$$\Omega_{0/\pi} = \frac{\omega_0}{\sqrt{1 \pm k}} \tag{2.21}$$

and eigenvectors

$$\mathbf{v}_{0/\pi} = \begin{pmatrix} 1 \\ \pm 1 \end{pmatrix}, \tag{2.22}$$

which correspond to the in phase (0 mode) and out of phase (π mode) normal modes of the system. Expanding this to an arbitrary number of $N+1$ cells and

assuming nearest neighbor coupling, equation 2.18 then becomes

$$I_n \left(1 - \frac{\omega_0^2}{\Omega^2}\right) + \kappa(I_{n-1} + I_{n+1}) = 0, \tag{2.23}$$

where $\kappa = k/2$. This equation can now be solved by imposing periodic boundary conditions and using *Floquet's theorem* ([13]), which states that

$$\begin{aligned} I_{n+1} &= I_n \cdot \exp(i\phi) \\ I_{n-1} &= I_n \cdot \exp(-i\phi), \end{aligned} \tag{2.24}$$

or in other words: Because of the spatial periodicity of the system, the individual functions I_n differ only by a phase factor $\exp(i\phi)$. It is interesting to note that this property of periodic structures is very common for example in solid state physics (see *Bloch's theorem*). Inserting equation 2.24 into 2.23 yields

$$\begin{aligned} & I_n \left(1 - \frac{\omega_0^2}{\Omega^2}\right) + \kappa(I_n \exp(-i\phi) + I_n \exp(i\phi)) = 0 \\ \iff & \left(1 - \frac{\omega_0^2}{\Omega^2}\right) + 2\kappa\cos(\phi) = 0 \\ \iff & \frac{1}{\Omega^2} = \frac{1 + 2\kappa\cos\phi}{\omega^2} \\ \iff & \Omega = \frac{\omega}{\sqrt{1 + 2\kappa\cos(\phi)}}. \end{aligned} \tag{2.25}$$

Using the result 2.21 it can be seen that $\phi = \pi q/N$, where $q \in [0, N]$ is the mode number. Therefore the dispersion relation for the normal modes is now given by

$$\Omega_q = \frac{\omega_0}{\sqrt{1 \pm k\cos(\pi q/N)}}, \tag{2.26}$$

where the sign of k depends on whether the cells are coupled magnetically ($\mathrm{sgn}(k) = -1$), or electrically ($\mathrm{sgn}(k) = +1$). The original derivation where the authors use a slightly different approach can be found in [14]. A more detailed derivation of equation 2.26 which also includes losses can be found in [13]. For particle acceleration π mode is the most used modes because of their particularly useful phase advance. Figure 2.6 shows the dispersion relation for seven magnetically coupled cells. From the plot one can immediately see one important aspect of coupled resonant structures, namely the mode spacing. In the vicinity of the 0 and π the mode spacing is smaller. For a large number of cells (typically > 9) this can lead to the so called *instability* of the π-mode, since adjacent modes begin to overlap.

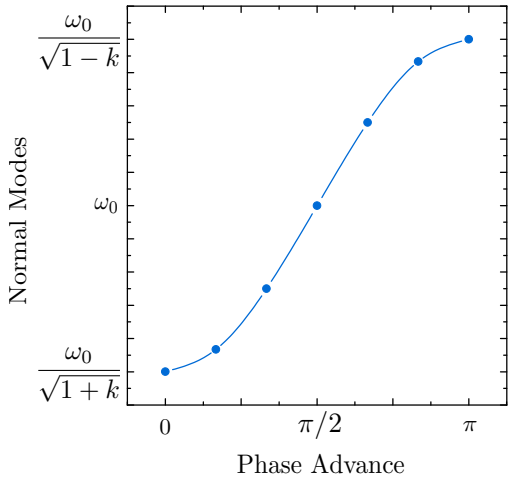

Figure 2.6: Dispersion relation for 7 magnetically coupled cells. The values have been calculated using equation 2.26.

It is important to note that due to the cosine term in the denominator, the dispersion curve shown in figure 2.6 can be extended for arbitrary values for the phase advance. This results in a sinusoidal shape of the dispersion curve and an infinite number of so called *spatial harmonics* for a given allowed frequency. Spatial harmonics on the positive slope can be attributed to forward waves, the ones on the negative slope are the backward wave spatial harmonics. The total electric field can then be understood as a sum over all the spatial harmonics.

2.1.4 Figures of Merit

Having established the basic concepts of waveguides and standing wave resonant cavities, the following section will highlight some of the important figures of merit of an RF cavity. The first important quantity is the so called *shunt impedance*, which is defined as

$$R_S = \frac{|U_{\mathrm{acc}}|^2}{P_d} \tag{2.27}$$

where U_{acc} is the effective accelerating voltage and P_d is the power loss, or the dissipated power. The effective accelerating voltage is defined by

$$U_{\mathrm{acc}} = \int E_z(z) e^{i\frac{\omega}{\beta c}z} \mathrm{d}z, \tag{2.28}$$

i. e. the voltage a particle with velocity βc experiences during its transit through the cavity, subject to time variations of the field. Therefore the proportionality factor, which connects U_{acc} with the time-independent accelerating voltage U_0 is called the *transit time factor* T_β. It is defined by

$$U_{\mathrm{acc}} = T_\beta \cdot U_0 = \frac{\int E_z(z) e^{i\frac{\omega}{\beta c}z} \mathrm{d}z}{U_0} \cdot U_0 = \frac{\int E_z(z) e^{i\frac{\omega}{\beta c}z} \mathrm{d}z}{\int E_z(z) \mathrm{d}z} \cdot U_0. \tag{2.29}$$

For the TM_{010}-mode $E_z(z) = E_0$ is not not a function of z, therefore the transit time factor can be calculated by noticing that the integral in the numerator is now just the Fourier transform of a box function. If $z \in [-L/2, L/2]$, then

$$T_\beta(\mathrm{TM}_{010}) = \frac{\sin\left(\frac{L}{\beta\lambda}\right)}{\frac{L}{\beta\lambda}}, \tag{2.30}$$

where $\omega/\beta c = 2\pi/\beta\lambda$ has been used. The cavity length L must now be chosen according to the free space wavelength λ and β (hence the particle type), such that T_β is maximized. This is called *β-matching* and the resulting mode is the *synchronous mode*. From this it can be concluded that all other spatial harmonics of the synchronous mode do not contribute to the net accelerating field, since they are not $\beta-$matched (recall figure 2.6).

The shunt impedance can be understood as the quantity that defines the efficiency of power transfer to the electron beam through $P_b = R_S \cdot I^2$. Knowing this, it is clear that R_S needs to be maximized. Power losses inside the cavity occur due to the finite conductivity of the cavity walls, which has been neglected in the calculations above. In fact the fields and surface currents penetrate into the cavity walls as deep as the so called *skin depth* ([15])

$$\delta_s = \sqrt{\frac{2}{\mu_0 \mu_w \sigma_w \cdot \omega}}, \tag{2.31}$$

where μ_w and σ_w are the wall permeability and conductivity respectively. The power loss is directly proportional to the skin depth and the square of the cavity voltage [15]. Therefore the shunt impedance is mostly influenced by the choice of material and the cavity shape. It is also important to note that the power loss depends on the particular cavity mode. In accelerator physics it is common to quote the shunt impedance per unit length, or the so called *specific shunt impedance*. As a rule of thumb the following formula can be used to estimate the specific shunt impedance for a copper cavity [15]:

$$r_s(\mathrm{M\Omega/m}) \approx 1.28 \cdot \sqrt{f_{\mathrm{rf}}(\mathrm{MHz})}. \tag{2.32}$$

Another important property of a resonator cavity is the *quality factor*. Resonator cavities can be thought of as damped oscillators with external excitation. The damping is again due to power losses in the cavity walls, but also due to the energy transfer from the field to the electron beam. Starting from the well known ODE for the damped harmonic oscillator

$$\ddot{x} + 2\alpha\dot{x} + \omega_0^2 = A_{\text{ext}} \exp(i\omega_{\text{ext}} t), \tag{2.33}$$

where α is the damping coefficient, one finds [15] solutions of the form $x = A\exp(i\omega_{\text{ext}}t)$. The amplitude A is then given by

$$A = a\exp(i\Psi) = \frac{A_{\text{ext}}}{\sqrt{(\omega_0^2 - \omega_{\text{ext}}^2)^2 + 4\alpha^2\omega_{\text{ext}}^2}} \exp(i\Psi), \tag{2.34}$$

where Ψ describes the phase shift between the external excitation and the oscillator and is often called the *tuning angle*, because its magnitude is a measure for the detuning of the system. The maximum of the amplitude is reached for the perturbed resonant frequency

$$\omega_{\text{ext}} = \sqrt{\omega_0^2 - 2\alpha^2}. \tag{2.35}$$

One can see that this frequency depends on the damping of the system. Without any damping the frequency response of the system would correspond to a δ-peak, but in reality the damping leads to broadening. The amount of broadening, or in other words the width of the resonance curve determines the quality factor of the system. It is defined as

$$Q = \frac{\omega_{\text{res}}}{2\alpha}. \tag{2.36}$$

Another definition relates the stored energy to the energy loss:

$$Q = \frac{\omega_{\text{res}} W_{\text{sto}}}{W_{\text{los}}}. \tag{2.37}$$

Knowing the quality factor of the system, the tuning angle near the resonance can be found using the following formula [15]:

$$\cot\Psi \approx 2Q\frac{\omega - \omega_{\text{res}}}{\omega_{\text{res}}}. \tag{2.38}$$

It is important to note that in reality due to lossy coupling between the waveguides and the cavity and in the case of an accelerator cavity the electron beam itself (*beam loading*), additional damping is introduced. Therefore two different factors exist for such cavities: The *loaded quality factor* Q (with beam and a coupling

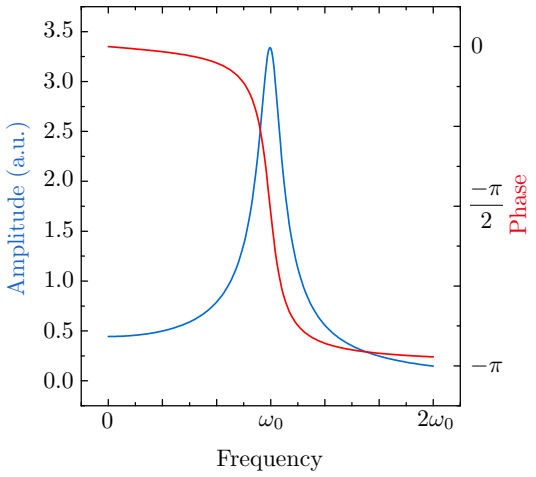

Figure 2.7: Amplitude and tuning angle for an externally excited damped resonator.

coefficient smaller than one) and the *unloaded quality factor* Q_0 (without beam and critical coupling). Looking at the definitions of both the shunt impedance and the quality factor, one notices that both depend on the power loss in the system, which is connected to the material properties. A more general figure of merit can be found by looking at the ratio between the shunt impedance and the quality factor R/Q, which is hence called *R over Q*. It is given as

$$\frac{R}{Q} = \frac{U_{\mathrm{acc}}^2}{\omega_{\mathrm{res}} W_{\mathrm{sto}}}. \tag{2.39}$$

R over Q only depends on the shape of the cavity and is therefore a useful characteristic quantity for resonator cavities.

2.2 CST Simulations

In the last section the basic theory of RF waveguides and standing wave cavities has been discussed. This section will focus on numerical simulations of the cavity modes for both the gun and the buncher using *CST Microwave Studio 2012*. The numerical calculations are based on three dimensional CAD drawings of the two cavities, as well as the coaxial coupler courtesy of Marcus Barenscheer (DESY). These calculations should show how the electric field configurations look like in the highly optimized cavities, which have been developed for REGAE. The results will

then be compared to actual RF measurements, which will be presented in section 2.6.1 in more detail.

2.2.1 Gun Cavity

The gun cavity used at REGAE is based on a 1.5 cell design. Table 2.2 shows the dimensions of the individual cells. Looking at the actual CAD drawing (see figure 2.8), it can be seen that the cells are tapered towards the ends. This leads to a reduction of peak electric fields and surface losses due to the high magnetic fields (recall figure 2.4). In addition to that, the iris (coupling hole between the cells) edges are shaped according to a circle arc, which reduces the non-linear components of the electric field in the gap region ([12]). The iris radius determines the coupling strength between the two cells. Since this system comprises two coupled resonators, the modes are expected to split into the 0- and the $\pi-$modes. Recalling the last chapter, the fundamental mode is the TM_{010}-mode, which now is split, due to the coupling. Figure 2.8 shows the simulation results for the TM_{010} modes. The RF signal is coupled into the cavity — like in the real experiment — using a coaxial coupling antenna. The coaxial design of the coupler avoids potential field asymmetries that would arise from other coupling schemes, like a simple coupling loop ([16]). One can see that the longitudinal fields inside the individual resonators are indeed in phase for the 0-mode as expected. The TM_{010} π-mode is also shown in figure 2.8. Here the fields — again as expected from the theory — differ in phase by π. Table 2.3 shows the calculated, as well as the measured mode frequencies. It can be seen that the frequencies are the same for the 0-mode, in the case of the π-mode there is a difference of approximately 1 MHz. Therefore the mode-spacing does not exactly correspond. This mismatch can have two reasons. The first could be inaccuracies in the three dimensional drawings. The second could be the tuning of the gun, as well as a slightly different position of the antenna due to a different gasket between the gun and antenna part. In addition to that the calculation has been performed using a dummy model of the cathode, which is different from the real cathode.

Table 2.2: Dimensions of the REGAE gun cavity (taken from the CAD drawings).

	Length (mm)	**Radius at center (mm)**
Half cell	23.83	39.33
Full cell	43.33	39.33
Iris gap	10.00	10.83

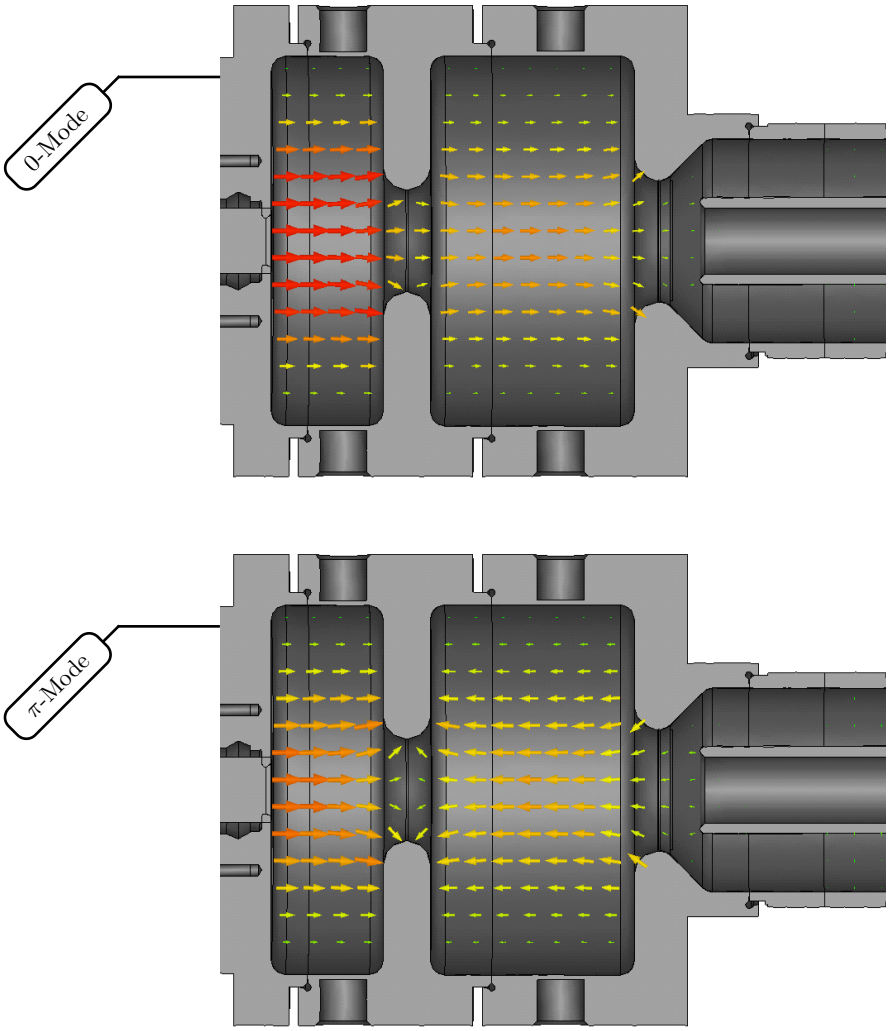

Figure 2.8: Numerical simulation of the electric field of the TM_{010} modes inside the REGAE gun cavity.

Table 2.3: Calculated and measured frequencies for the gun TM_{010} modes. All values are given in GHz.

	0-mode	**π-mode**
Microwave Studio	2.989	2.997
Measurement	2.989	2.998

2.2.2 Buncher Cavity

The buncher cavity comprises four full cells. The dimensions of the individual cells are shown in table 2.4. It can be seen that the cells are only tapered towards one end. This is due to the modular design of the cavity, which allows stacking of individual cell modules. Since the cavity contains four cells, the expected fundamental modes are the TM_{010} 0, TM_{010} $\pi/3$, TM_{010} $2\pi/3$ and TM_{010} π-mode. Figure 2.9 shows all of the TM_{010} modes for the buncher cavity. Again, the phase relations are as expected. Table 2.5 shows the calculated, as well as the measured mode frequencies. It can be seen that the spacing between the adjacent modes is — bearing in mind the accuracy of both the RF measurements and the simulations — in good agreement, except for the spacing between the 0-mode and its adjacent mode. The measured 0-mode is 1 MHz lower than the simulated one. The difference between the actual values is again due to additional tuning of the cavity and possible inaccuracies in the three dimensional mesh of the CAD drawing. Recalling the dispersion curve (figure 2.6) for coupled resonators, one might ask why the modes spacing the 0- and its adjacent mode is not the same as the spacing between the π-mode and its adjacent mode. It has to be noted here, that the derivation of equation 2.26 — which has been used to calculate the disperion curve — is based on the assumption of identical cell to cell coupling coefficients. Numerical simulations using Microwave Studio take these factors and the actual cavity shape into account.

Table 2.4: Dimensions of the REGAE buncher cavity (taken from the CAD drawings).

	Length (mm)	**Radius at center (mm)**
Full cells	40.00	39.33
Iris gap	10.00	10.83

Table 2.5: Calculated and measured frequencies for the buncher TM_{010} modes. All values are given in GHz.

	0-mode	**$\pi/3$-mode**	**$2\pi/3$-mode**	**π-mode**
Microwave Studio	2.983	2.988	2.993	2.995
Measurement	2.985	2.991	2.996	2.998

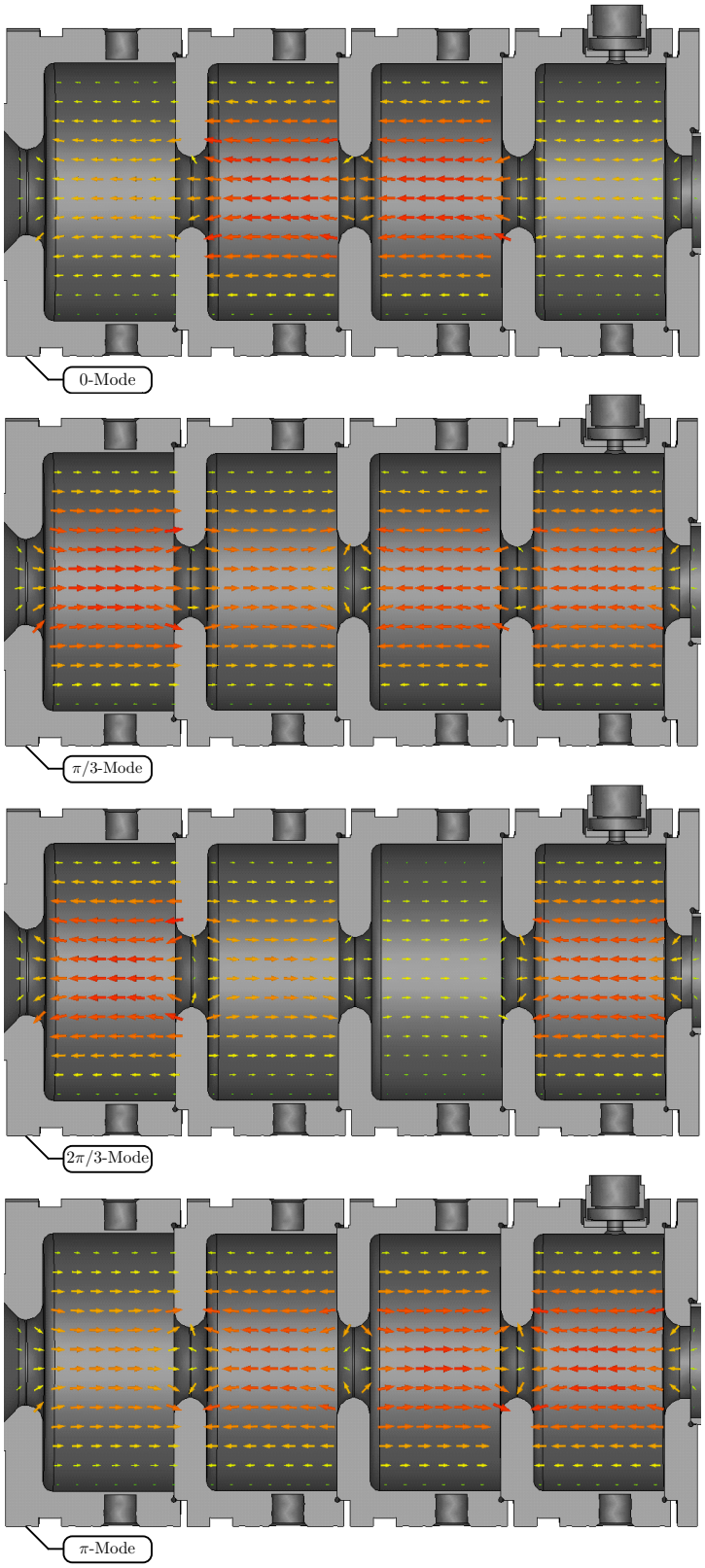

Figure 2.9: Numerical simulation of the electric field of the TM_{010} modes inside the REGAE buncher cavity.

2.3 Analytical Description of the RF System

In the preceding sections the basic properties of RF waveguides and resonator cavities, as well as numerical simulations of the actual REGAE gun and buncher cavity fields using CST Microwave Studio have been presented. This section will focus on the unique RF setup at the REGAE facility. At REGAE both cavities are fed by a single klystron. Figure 2.10 shows a simple schematic of the setup. The signal is first split by the *shunt-T* and then delivered via the two waveguide arms to the individual cavities. On the gun arm a phase shifter has been implemented. This device enables the operators to adjust both phases (gun, buncher) independently, since any adjustments to the klystron phase affect both cavities at the same time. The phase shifter can also be used to alter the power distribution in the system, which would otherwise be fixed by the shunt-T. In reality, the cavities will always reflect a portion of the incoming wave. Hence the two cavities by design of the RF system are prone to crosstalk effects. These crosstalk effects also alter the behavior of the phase shifter. Using the so called *S-Matrix formalism*, an analytical model will now be developed, in order to understand how the system reacts to adjustments of the phase shifter settings.

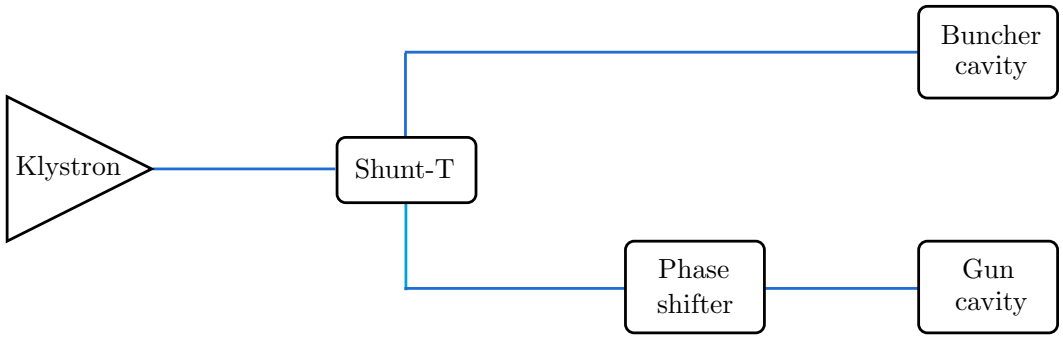

Figure 2.10: Simple schematic of the REGAE RF system.

2.3.1 S-Matrix Formalism

The behavior of an n-port network of RF devices can be described using the so called *S- or Scattering-Matrix* formalism. What this matrix essentially describes is the reaction of the system to incoming waves a_i onto either of the n ports. Using this formalism, it is easy to calculate the outgoing waves b_i for all the n ports. The

general formulation for an n-port reads:

$$\mathbf{b} = \hat{\mathbf{S}} \cdot \mathbf{a} \tag{2.40}$$

where both $\mathbf{a}$ and $\mathbf{b}$ are n-dimensional vectors and $\hat{\mathbf{S}}$ is an $n \times n$ matrix. The matrix elements S_{ij} — or *S-parameters* are unique for every element in the network and have to be calculated. For most of the commonly used elements there are tables of S-parameters available ([17]). The diagonal elements of the S-matrix are called *reflection coefficients*. In the case of a 2-port device, the off-diagonal matrix elements are called the *forward gain coefficients*. The S-matrix of a simple transmission line (and hence a 2-port) is given by:

$$\hat{\mathbf{S}}_T = \begin{pmatrix} 0 & e^{-\underline{\gamma} L} \\ e^{-\underline{\gamma} L} & 0 \end{pmatrix}, \tag{2.41}$$

where L is the length of the transmission line and $\underline{\gamma} = \alpha + ik$, with the attenuation factor α and the wave number k is called the *propagation factor*. Looking at the matrix elements, one can immediately see the effect of the transmission line on an incoming wave. In the case of the transmission line, a phase factor plus a possible attenuation is added and no reflections at the ports occur, which is the expected result for a transmission line element.

Figure 2.11: A two-port device.

Phase Shifter

The RF system at the REGAE facility incorporates a two-arm mechanical phase shifter (see figure 2.12), where the phase shift can be adjusted by altering the lengths of the two arms, which are both terminated critically and hence have a reflection coefficient $r = 1$. Adjustment of the length is achieved using stepper motors, which can be remotely controlled from the control room. The phase shifter is essentially a 2-port device, but the theoretical treatment has to be done using 4-port network theory. Every n-port device can be broken down into an arbitrary

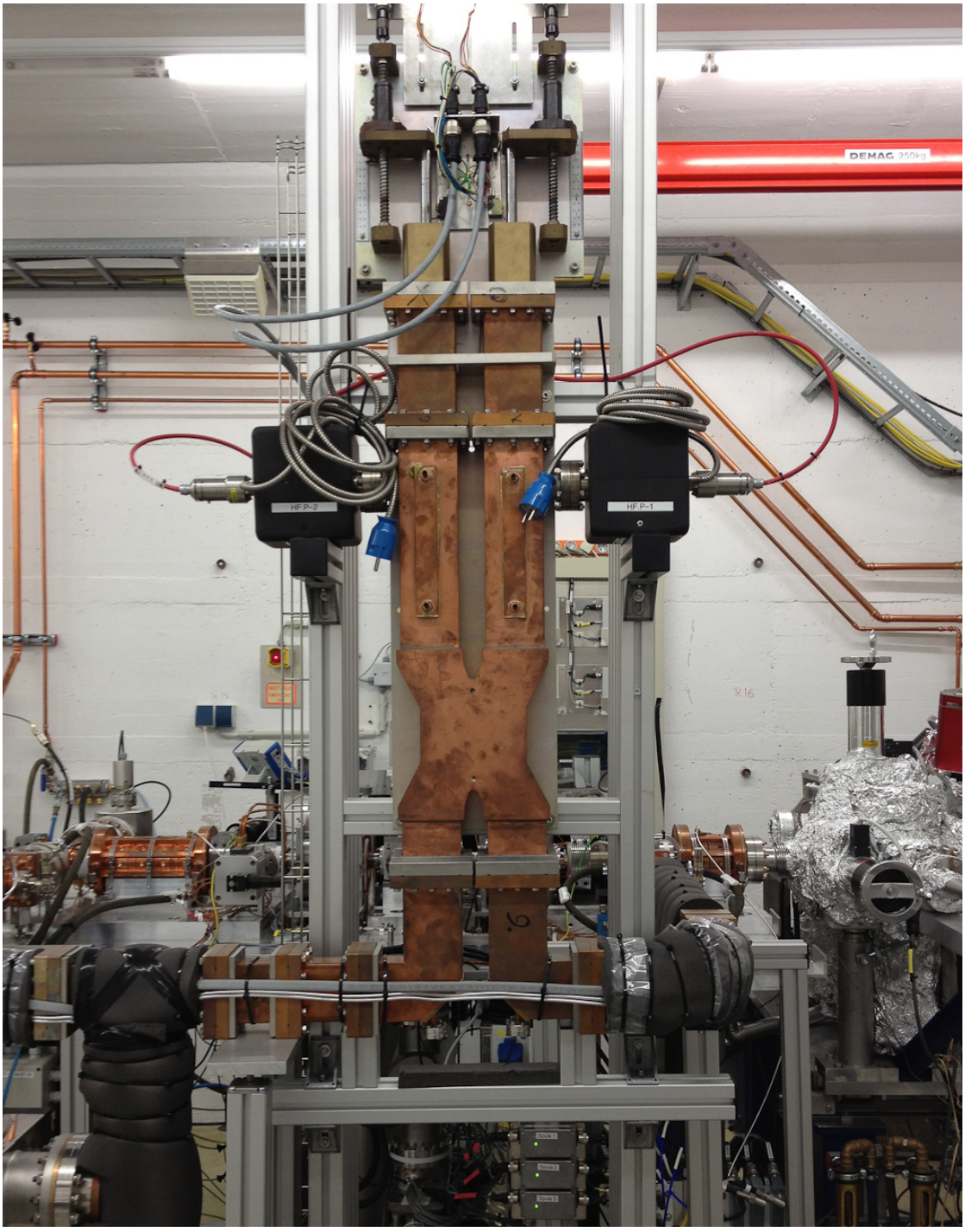

Figure 2.12: Photo of the REGAE phase shifter.

amount of concatenated sub-devices ([17]). In the case of the REGAE phase shifter, the network contains a so called *4-port 3 dB coupler* and two transmission lines with lengths L_2 and L_4 (the two arms) (see figure 2.10). As it has been

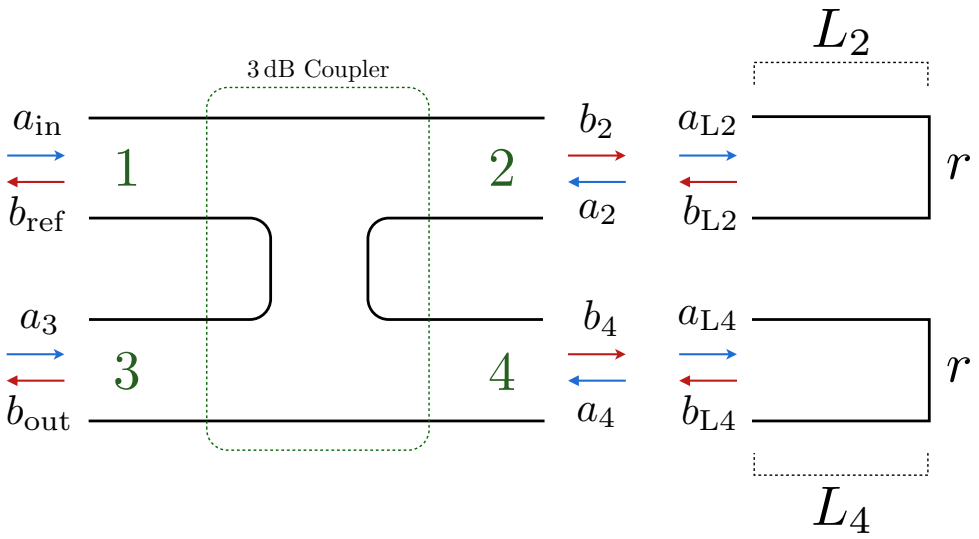

Figure 2.13: Schematic of the REGAE phase shifter.

mentioned above, the transmission lines are both terminated with $r = 1$. The S-matrix of the transmission lines can be found in equation 2.41, the matrix of a 3 dB coupler looks as follows ([17]):

$$\hat{\mathbf{S}}_{\text{3db}} = \frac{1}{\sqrt{2}} \cdot \begin{pmatrix} 0 & 1 & 0 & i \\ 1 & 0 & i & 0 \\ 0 & i & 0 & 1 \\ i & 0 & 1 & 0 \end{pmatrix} \tag{2.42}$$

In the following calculations it is assumed that there is no input at port 3 (see figure 2.13). Using equations 2.42, 2.41 and 2.40 and $a_3 = 0$ we get:

$$\begin{aligned} b_1 &= S_{3dB,12} \cdot a_2 + S_{3dB,14} \cdot a_4 \equiv b_{\text{ref}} \\ b_2 &= S_{3dB,21} \cdot a_1 \\ b_3 &= S_{3dB,32} \cdot a_2 + S_{3dB,34} \cdot a_4 \equiv b_{\text{out}} \\ b_4 &= S_{3dB,41} \cdot a_1 \end{aligned} \tag{2.43}$$

The input signals to ports 2 and 4 must be calculated using the S-matrix of a transmission line:

$$\begin{aligned} a_2 &= e^{-2\underline{\gamma}L_2} \cdot b_2 = e^{-2\underline{\gamma}L_2} \cdot \frac{a_1}{\sqrt{2}} \\ a_4 &= e^{-2\underline{\gamma}L_4} \cdot b_4 = e^{-2\underline{\gamma}L_4} \cdot \frac{a_1}{\sqrt{2}} \cdot i, \end{aligned} \tag{2.44}$$

where in figure 2.13 $a_1 = a_{\text{in}}$, $b_1 = b_{\text{ref}}$ and $b_3 = b_{\text{out}}$. It is now easy to calculate the output wave and the reflected wave:

$$\begin{aligned} b_{\text{out}} &= \frac{a_4 + ia_2}{\sqrt{2}} \\ b_{\text{ref}} &= \frac{a_2 + ia_4}{\sqrt{2}}. \end{aligned} \tag{2.45}$$

In order to check conservation of power, it is necessary to check if the modulus squared of the input is equal to the sum of the modulus squared of output and reflected wave:

$$|b_{\text{out}}|^2 + |b_{\text{ref}}|^2 = b_{\text{out}}^\star b_{\text{out}} + b_{\text{ref}}^\star b_{\text{ref}} = \frac{|a_{\text{in}}|^2}{2} + \frac{|a_{\text{in}}|^2}{2} = |a_{\text{in}}|^2. \tag{2.46}$$

The system as calculated satisfies the conservation of power.

The Phase Shifter as a 2-Port Device

As it has been stated above, the phase shifter is essentially a 2-port device. Therefore it must be possible to describe the system using a 2×2 scattering matrix. Assuming again that $a_3 = 0$, i.e. that the load is perfectly matched, we immediately get using equation 2.40:

$$\hat{\mathbf{S}}_{\text{2portPS}} = \frac{1}{2} \cdot \begin{pmatrix} \left[e^{-2\underline{\gamma}L_2} - e^{-2\underline{\gamma}L_4}\right] & 0 \\ i \cdot \left[e^{-2\underline{\gamma}L_4} + e^{-2\underline{\gamma}L_2}\right] & 0 \end{pmatrix}. \tag{2.47}$$

In the above calculations it has always been assumed that $a_3 = 0$ in order to keep the calculations simple. This in fact leads to a scattering matrix 2.47 that is not completely correct, as such a device violates *reciprocity*. A network that contains only transmission lines and a phase shifter must be reciprocal. Reciprocity describes the fact that the behavior of the system does not depend on the direction of the signal, or in other words that it must be possible to exchange input and output without changing the effect of the device on the signal. Mathematically

this means that the scattering matrix must be equal to its transpose, i.e. $\hat{\mathbf{S}} = \hat{\mathbf{S}}^T$. Therefore the reciprocal 2-port scattering matrix for the phase shifter must be:

$$\hat{\mathbf{S}}_{\text{2portPS}} = \frac{1}{2} \cdot \begin{pmatrix} \left[e^{-2\underline{\gamma}L_2} - e^{-2\underline{\gamma}L_4}\right] & i \cdot \left[e^{-2\underline{\gamma}L_4} + e^{-2\underline{\gamma}L_2}\right] \\ i \cdot \left[e^{-2\underline{\gamma}L_4} + e^{-2\underline{\gamma}L_2}\right] & \left[e^{-2\underline{\gamma}L_2} - e^{-2\underline{\gamma}L_4}\right] \end{pmatrix} \tag{2.48}$$

This is now the final S-matrix for the REGAE phase shifter. The next device it is necessary to find an S-matrix for, is the shunt-T power divider.

Shunt-T Power Divider

A power divider is a 3-port device, which splits the incoming power P_1 at port 1 into P_2 at port 2 and P_3 at port 3. The division factor $\alpha = P_2/P_3$ is not fixed to 0.5, but the device can be constructed to accomplish any factor from 0 to 1. It can be shown that it is physically not possible to construct a 3-port device that is at the same time matched, lossless and reciprocal. For the calculations a so called *resistive power divider* will be used, which is assumed to be matched, reciprocal, but lossy.

Due to the assumption that all ports are matched, the diagonal elements of the scattering matrix vanish and therefore

$$S_{11} = S_{22} = S_{33} = 0. \tag{2.49}$$

Another assumption of this model is efficient devision of the power, or in other words that the division process does not result in any power loss. This immediately yields

$$|S_{11}|^2 + |S_{21}|^2 + |S_{31}|^2 = 1. \tag{2.50}$$

and hence $|S_{21}|^2 = \alpha$ as well as $|S_{31}|^2 = 1 - \alpha$. The third assumption (which is cleary unrealistic and needs to be addressed) is that there is no crosstalk between port 2 and 3:

$$S_{23} = S_{32} = 0. \tag{2.51}$$

From the reciprocity condition the last matrix elements are:

$$\begin{aligned} S_{12} &= S_{21} \\ S_{13} &= S_{31}. \end{aligned} \tag{2.52}$$

Now the scattering matrix for the resistive power divider can be written as:

$$\hat{\mathbf{S}}_{\text{ShuntT}} = -i \cdot \begin{pmatrix} 0 & \sqrt{\alpha} & \sqrt{1-\alpha} \\ \sqrt{\alpha} & 0 & 0 \\ \sqrt{1-\alpha} & 0 & 0 \end{pmatrix}. \tag{2.53}$$

In order to address the crosstalk between the two arms the following matrix has to be used:

$$\hat{\mathbf{S}}_{\mathrm{ShuntT}} = -i \cdot \begin{pmatrix} 0 & \sqrt{\alpha} & \sqrt{1-\alpha} \\ \sqrt{\alpha} & 0 & \sqrt{\alpha} \\ \sqrt{1-\alpha} & \sqrt{1-\alpha} & 0 \end{pmatrix}. \tag{2.54}$$

One immediately sees that this modification breaks the reciprocity of the matrix for $\alpha \neq 0.5$. This is the expected result, because as soon as the power is not distributed evenly, the choice of ports does indeed matter.

Cavity Couplers

At REGAE the RF waves are coupled into the cavity using a coaxial coupler. The coupling can essentially be described by one single quantity, namely the *coupling coefficient* β. A coupling coefficient equal to unity would correspond to a perfect coupling and hence complete transmission of the wave. In scattering matrix formalism this device can be described as a 2-port. The coupling matrix is therefore given by

$$\hat{\mathbf{S}}_{\mathrm{Coupler}} = -i \cdot \begin{pmatrix} \sqrt{1-\beta} & \sqrt{\beta} \\ \sqrt{\beta} & \sqrt{1-\beta} \end{pmatrix}. \tag{2.55}$$

2.3.2 The T-Matrix

In the previous sections the S-matrices of the RF devices used in the REGAE RF system have been calculated and discussed. The advantage of the S-matrix approach is that it reduces the description of a rather complex system to a simple matrix multiplication. One disadvantage however is that it is not possible to concatenate these matrices. For a chain of an arbitrary number of 2-port devices the so called *T-matrices* can be used. The T-matrices (or transfer matrices) of 2-port devices can be concatenated in order to describe the whole system with one matrix. This total transfer matrix then takes all reflections into account. The T-matrix of a 2-port device is defined by

$$\begin{pmatrix} b_1 \\ a_1 \end{pmatrix} = \begin{pmatrix} T_{11} & T_{12} \\ T_{21} & T_{22} \end{pmatrix} \cdot \begin{pmatrix} a_2 \\ b_2 \end{pmatrix} = \hat{T} \cdot \begin{pmatrix} a_2 \\ b_2 \end{pmatrix}. \tag{2.56}$$

A chain of 2-port devices can then be described by the total transfer matrix

$$\hat{T}_{\mathrm{tot}} = \hat{T}_n \cdot \hat{T}_{n-1} \cdots \hat{T}_2 \cdot T_1. \tag{2.57}$$

Conversion between S- and T-matrices can be done using the following formulae ([17]):

$$
\begin{aligned}
T_{11} &= -\frac{\det(\hat{\mathbf{S}})}{S_{21}} & S_{11} &= \frac{T_{12}}{T_{22}} \\
T_{12} &= \frac{S_{11}}{S_{21}} & S_{12} &= \frac{\det(\hat{\mathbf{T}})}{T_{22}} \\
T_{21} &= -\frac{S_{22}}{S_{21}} & S_{21} &= \frac{1}{T_{22}} \\
T_{22} &= \frac{1}{S_{21}} & S_{22} &= -\frac{T_{21}}{T_{22}}
\end{aligned}
$$

This way it is possible to calculate an S-matrix for a chain of devices. It has to be noted though that this approach is only valid for a chain of 2-port devices ([18]). For the REGAE RF system the T-matrix approach will be applied to both the gun- and the buncher-arm. The whole system can then be calculated by solving equation 2.40 using 2.54.

Combining all Devices

Having calculated all the relevant scattering matrices, it is now possible to combine them using the T-matrix approach. In addition to that, it is useful to note that both arms (gun- and buncher-arm respectively) are effectively 1-port devices and can be described by a time and frequency dependent reflection coefficient $r(t, \omega)$. Using this and the assumption that the connections to the shunt-T are matched, it is possible to solve the set of equations for the scattering matrix 2.54.

$$
\begin{aligned}
b_1 &= \sqrt{\alpha} \cdot a_2 + \sqrt{1-\alpha} \cdot a_3, \\
b_2 &= \sqrt{\alpha} \cdot a_1 + \sqrt{\alpha} \cdot a_3, \\
b_3 &= \sqrt{1-\alpha} \cdot a_1 + \sqrt{1-\alpha} \cdot a_2,
\end{aligned}
\tag{2.58}
$$

where $a_2 = r_b(t, \omega) \cdot b_2$ and $a_3 = r_g(t, \omega) \cdot b_3$. Solving this set of equations yields

$$
\begin{aligned}
b_1 &= \frac{a_1 r_b \alpha^2 + a_1 r_b r_g \alpha^2 \beta + a_1 r_g \beta^2 + a_1 r_b r_g \alpha \beta^2}{r_b r_g \alpha \beta - 1}, \\
b_2 &= -\frac{a_1 \alpha + a_1 r_g \alpha \beta}{r_b r_g \alpha \beta - 1}, \\
b_3 &= -\frac{a_1 \beta + a_1 r_b \alpha \beta}{r_b r_g \alpha \beta - 1},
\end{aligned}
\tag{2.59}
$$

where $\beta = 1 - \alpha$. In order to get the reflection coefficients for the arms one just has to use the fact that $b_{\text{ref}} = r(t, \omega) \cdot a_{\text{in}}$, where b_{ref} can be calculated using the total

S-matrix of the arm and the reflection coefficient of the cavity coupler. Therefore:

$$r_i(t,\omega) = \frac{b_{\mathrm{ref},i}}{a_{\mathrm{in}}} \tag{2.60}$$

These sets of equations can now be used as a model for the behavior of the phase shifter. In the next section the model will be compared to actual RF measurements that have been conducted at REGAE.

2.4 Phase Shifter Measurements

In the preceding section an analytical description of the RF system at REGAE has been developed using the S-matrix formalism. The main motivation for this is the need to be able to gain an understanding of how the phase shifter acts on the cavity phases and amplitudes during machine operation. Ideally — which means without any crosstalk between the cavities — the phase shifter just acts on the gun phase. In order to test this and the analytical model, an automated phase shifter scan procedure has been implemented as a MATLAB ([19]) stand-alone tool. There are three questions that need to be answered now:

(1) How does the phase shifter act on the machine, when both arms are moved at the same time?

(2) How can the power distribution be altered by moving the arms independently?

(3) Can these behaviors be described by the analytical model?

Using the phase shifter scan tool the following measurements have been conducted.

Both Arms at the same Time

Figure 2.14 shows the results of a phase shifter scan, where both arms have been moved at the same time over the whole possible travel range. The recorded data is the gun forward phase, i. e. the phase measured at a directional coupler right before the gun cavity. Two theoretical curves that have been calculated using the theoretical model are also shown. Several things can now be extracted here. First of all, the measurement shows that the gun phase can be shifted at a rate of approximately 5.15 deg/mm. This result should be connected to the guide wavelength λ_{g} as defined in equation 2.9. Taking the two arm design of the phase

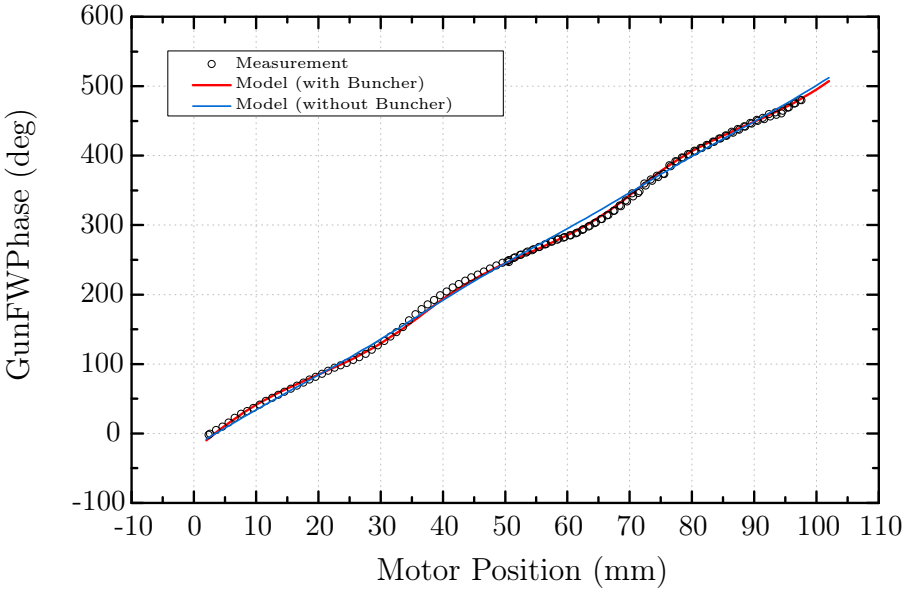

Figure 2.14: Comparison between measurement and simulation of the gun forward phase for a simultaneous scan of both phase shifter motor positions.

shifter into account, a travel distance of λ_g results in a phase shift of $2 \cdot 360\,\mathrm{deg}$. Therefore the theoretical rate is given by

$$\frac{\Delta\phi}{\Delta z} = \frac{720\,\mathrm{deg}}{\lambda_g}. \tag{2.61}$$

The guide wavelength for the fundamental mode of the REGAE waveguides can be calculated using equations 2.7 and 2.9 to be $\lambda_g = 13.9\,\mathrm{cm}$, where the waveguide dimensions $a = 7.2\,\mathrm{cm}$ and $b = 3.4\,\mathrm{cm}$ have been used. Inserting this result into equation 2.61 yields the theoretical phase shift rate of $5.18\,\mathrm{deg/mm}$, which differs from the measured value by only 0.6 %. The second insight that can be extracted is the fact that the phase change is subject to a slight periodicity. Comparison with the theoretical model shows that the measured signal can be described by the model as soon as the buncher arm is added to the model. Two things can therefore be concluded:

(1) The effect of the phase shifter on the machine parameters is altered by the cross-talk between the gun and buncher cavities.

(2) The measurement can be described by the simple theoretical model.

Since the periodicity in the phase signal seems to stem from the cross-talk between the cavities, another measurement has been conducted with a 20 mm offset between

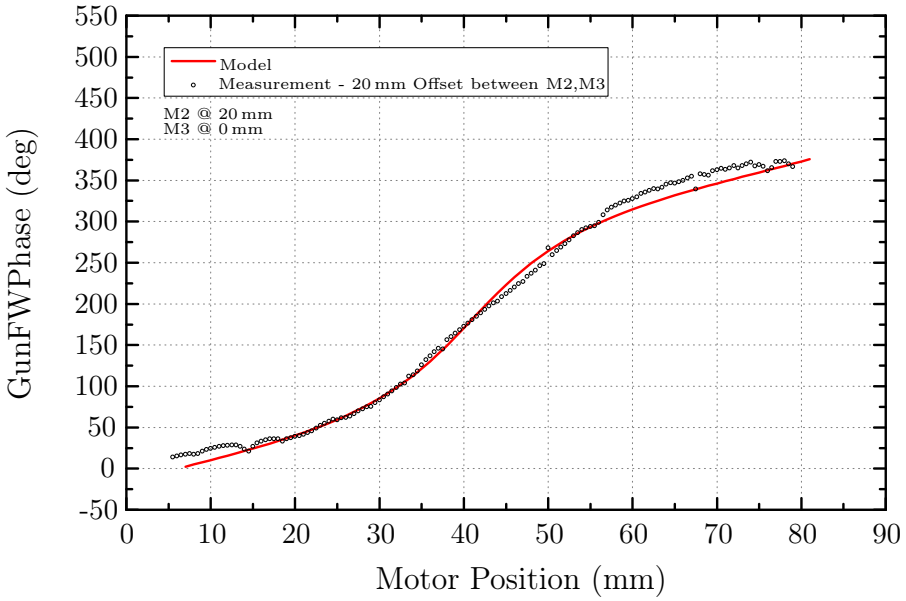

Figure 2.15: Comparison between measurement and simulation of the gun forward phase for a simultaneous scan of both phase shifter motor positions with an offset of 20 mm.

the motor positions. This way the power distribution and hence the strength of the cross-talk can be altered. Figure 2.15 shows the results of this measurement compared to the theoretical model. It can be seen that the periodicity has changed substantially due to the offset. This is an important result, because it has to be taken in account by the operator, when the power distribution needs to be changed with respect to the design setting. From both measurements it is now clear that the phase shifter not only acts on the gun phase, but also on the buncher and vice versa. Figure 2.16 shows the behavior of the buncher forward amplitude and phase for a simultaneous scan of both phase shifter motor positions without any offset. Once again, the data can be described by the analytical model.

Moving the Arms independently

As it has already been stated above, the power distribution between the two cavities can be adjusted using the phase shifter, by varying the offset between the motor positions. This effect is simply due to the additional reflections one introduces at the phase shifter ports. Figure 2.17 shows the result of a measurement of the gun forward amplitude as a function of the displacement of the two motor positions. Again, the scan can be described by the theoretical model nearly flawlessly. Only the dip on the first peak (between -60 and -40 mm) does not lie on the

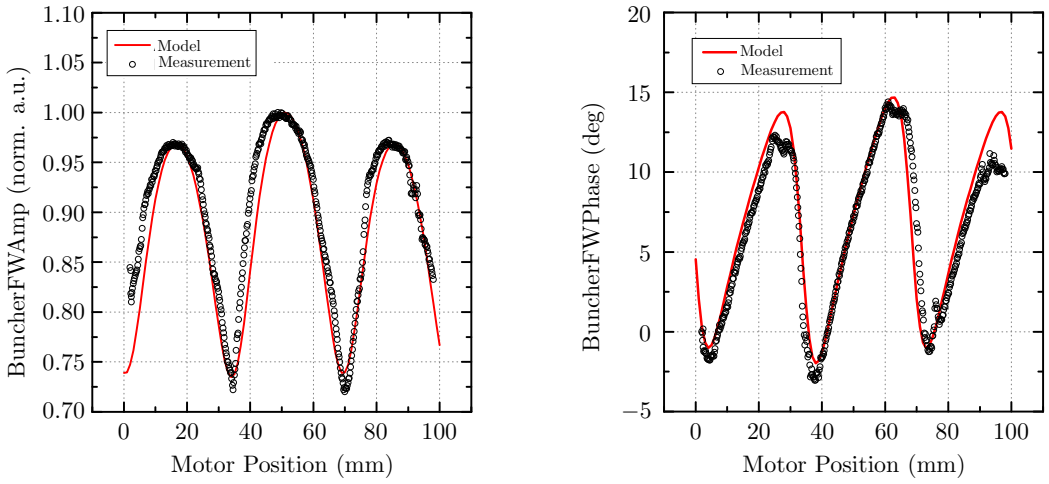

Figure 2.16: Comparison between measurement and simulation of the buncher forward amplitude (left plot) and phase (right plot) during a scan of the phase shifter (both arms at the same time) over the full travel range.

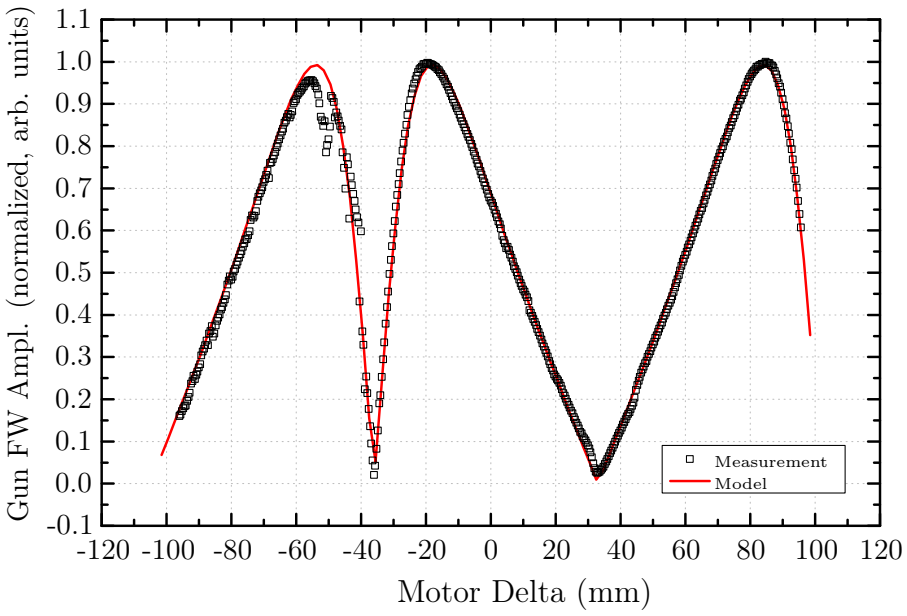

Figure 2.17: Comparison between measurement and simulation of the gun forward amplitude for a scan of the difference between the phase shifter motor positions. "Motor Delta" $\equiv x_{M3} - x_{M2}$.

theoretical curve. This dip might be caused by damages in the phase shifter arms. This can be concluded from the fact that the effect has been observed in later measurements as well for similar phase shifter settings. From the measurement and the model it can be seen that it is indeed possible to lower the gun amplitude to almost zero, or in other words introduce near total reflection on the phase shifter. This way the power division can be altered substantially.

Concluding Remarks

In this section the effect of the phase shifter on the amplitude and phase have been discussed. In addition to that, the analytical model has been proven to be able to describe the behavior of the cavity phases and amplitudes qualitatively, even though it is based on very basic assumptions.

The measurement also showed how the power division can be adjusted using the phase shifter, but they also reveal the fact that it would have been possible to basically disable the buncher, if the phase shifter would have been installed on the buncher arm. Being able to disable the buncher — or lower its effect on the beam – is important for many characterization measurements, like a phase scan for the gun energy. In addition to that, emittance measurements using solenoid scans also require the buncher to be turned off (see [20]). The initial motivation to implement the phase shifter in the gun arm however is to account for the fact that the reflected power on the shunt-T is larger for the buncher port than for the gun port. Therefore the phase shifter has been implemented on the gun arm, in order to minimize unwanted effects on the cavities due to changing phase shifter settings.

It has also been shown that operating the phase shifter at REGAE is not a trivial task. In the following section a useful future application of the analytical model will be presented, which could alleviate the operation of the phase shifter in the future.

2.5 Arbitrary Phase Tool

One of the most important features of the REGAE setup is the combination of gun and buncher cavity. Since the two cavities are both fed by one klystron, the mechanical phase shifter has been included in the RF design in order to be able to adjust the phases of both cavities independently. Unfortunately the last section has shown that due to cross-talk effects the operation of the phase shifter is not trivial.

2.5.1 Arbitrary Phase Algorithm

In this section an algorithm based on the analytical model shown in the preceding section will be developed. It will help the REGAE operators in the future with the usage of the phase shifter by determining the two setpoints (ψ, L) for the klystron phase and the phase shifter motor setting respectively for a given energy. The dependence of the setpoints on the beam energy is due to the energy dependence of the time of flight of the electron bunch between the two cavities. This then results in an additional phase factor $\Delta\tilde{\phi}(E)$ that needs to be taken into account. A more thorough derivation of the bunch time of flight can be found in section 3.2. Figure 2.18 shows the algorithm in form of an UML (Unified Modeling Language) diagram. The algorithm consists of three main blocks:

(1) Calculation of the phase correction factor $\Delta\tilde{\phi}(E)$ using theoretical considerations and ASTRA tables

(2) Coarse adjustment of (ψ, L) via previously calculated tables and the analytical model in a small setpoint space volume

(3) Fine tuning of (ψ, L).

In the first part the phase correction due to the energy dependence of the bunch time of flight has to be calculated. This factor needs to be considered, because the calibration of the buncher phase (see next section) is only valid for one fixed energy. The phase correction can be split into two main contributions. We have

$$\Delta\tilde{\phi}(E) = \delta\phi_{\mathrm{TOF}}(E) + \delta\phi_{\mathrm{gun}}(E). \tag{2.62}$$

The first contribution is the phase difference due to the time of flight difference between the gun and the buncher. For two electron bunches the time of flight difference after a drift section can be described by

$$\Delta T = \frac{d}{c}\left(\frac{1}{\beta_2} - \frac{1}{\beta_1}\right), \tag{2.63}$$

where d is the distance of the drift, c is the speed of light and β_i is the normalized velocity of the respective electron bunch. The phase difference is then given by

$$\Delta\phi = \beta_2 ck \cdot \Delta T = kd\left(1 - \frac{\beta_2}{\beta_1}\right), \tag{2.64}$$

where $k = 2\pi f/c$. The second contribution stems from the time of flight difference that occurs inside of the gun cavity. This cannot be computed easily, but it can be

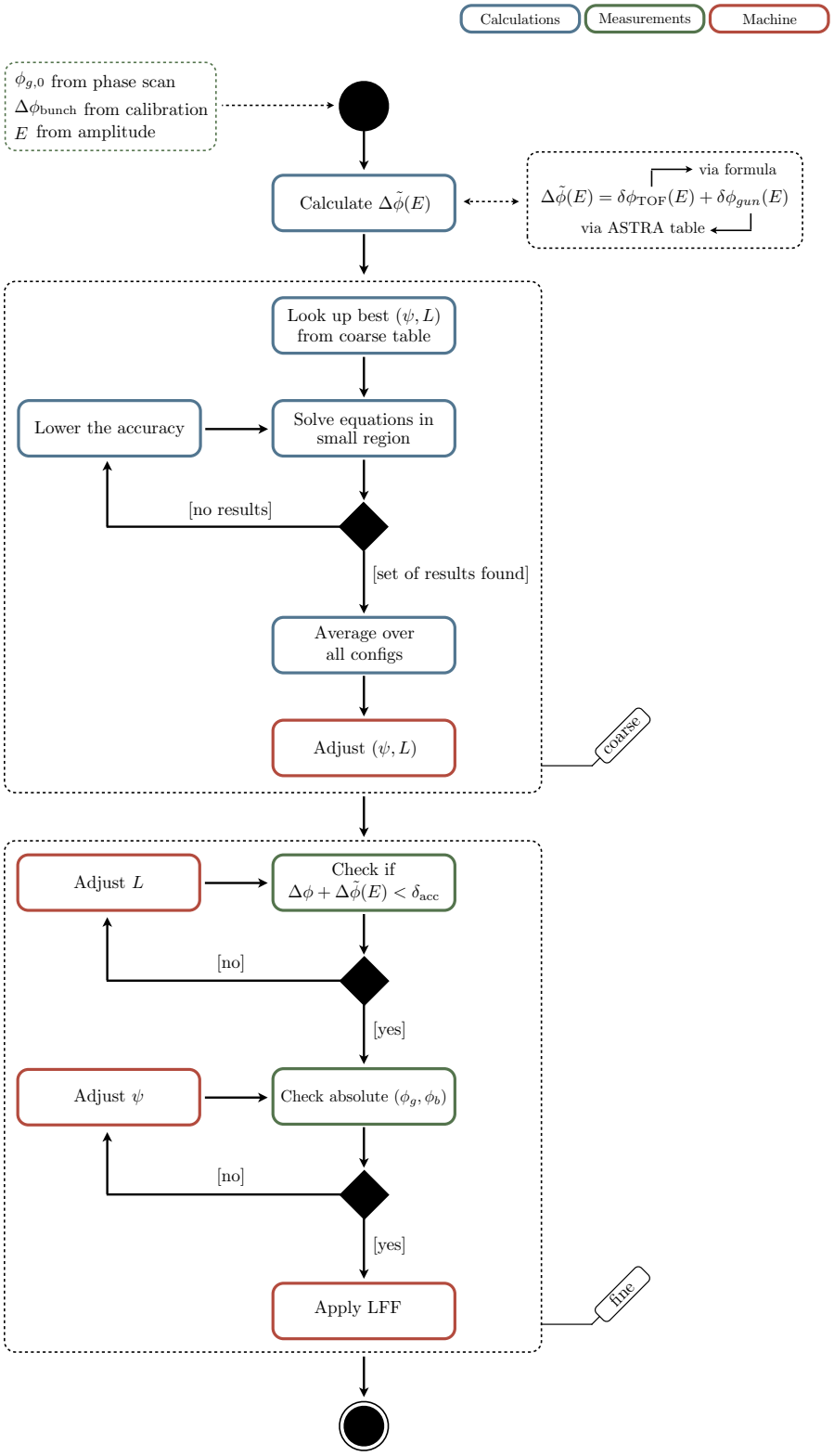

Figure 2.18: Enhanced UML diagram of the arbitrary phase algorithm.

calculated numerically using the equation that will be derived in section 3.2, or by using an *ASTRA* simulation. ASTRA (**A** **S**pace **C**harge **T**racking **A**lgorithm) is a numerical particle tracking algorithm, that has been developed at DESY ([21]). This way a table of arbitrary accuracy can be included into the program using equation 2.64.

In the second block the best (ψ, L) will be picked from a previously calculated table of configurations (using the analytical model of the phase shifter) based on the two input phases (ϕ_g, ϕ_b), $\Delta\tilde{\phi}(E)$ and the zero phases that have been determined through calibration (see next section).

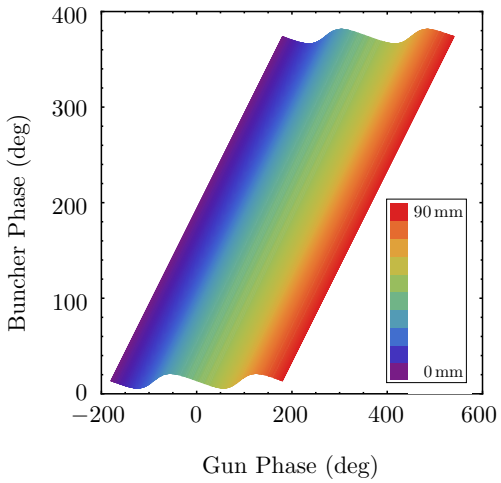

Figure 2.19: Parametric plot of the cavity phase configuration space, that can be explored using the klystron phase setting and the phase shifter (phases are arbitrary).

The last part of the algorithm is the fine tuning part, which is necessary due to inaccuracies in the analytical model and the mechanical damages in the phase shifter that have been discussed above. Fine tuning has to be applied also due the fact that the vector modulator slightly couples amplitude and phase (or in other words: changes in phase result in a small change in amplitude and vice versa). As the final step the so called *learning feed forward* will be applied, which is an adaptive feed forward system that has been implemented as part of the low level RF system (LLRF).

2.5.2 Finding the Zero Phases

In order for the algorithm to work, the two cavities need to be calibrated in terms of phase dependent energy gain. This is a procedure that needs to be performed — at least for the gun cavity — prior to every measurement, even when the algorithm is not to be used.

Gun Cavity

The main tool for this calibration is the *phase scan tool*, that has been implemented in the REGAE consoles as a MATLAB tool. The tool scans the klystron phase and simultaneously records the charge that is measured via a Faraday cup. For the calibration of the gun phase, the DDC1 cup right after the gun is used. Figure 2.20 shows such a phase scan. The blue curve represents the recorded charge at DDC1. The exact shape of the resulting curve will be discussed in more detail in the next chapter. During operation, this measurement is a standard tool for determining the maximum energy gain phase for the gun cavity, as it can be performed even with enough accuracy in under a minute. In order to determine the maximum energy gain phase — or *zero phase* — a phase scan has been performed whilst measuring the mean beam energy using the dipole spectrometer. Since the dipole spectrometer is installed behind the buncher cavity, it had been detuned during the scan in order to be able to just record the gun cavity's contribution to the beam energy. The results are also shown in figure 2.20. It can be seen that the maximum energy gain occurs at +40 deg from the phase, where the first charge can be detected on the Faraday cup. As this kind of measurement requires the buncher to be detuned and in addition to that has to be performed manually using the dipole spectrometer (which is not yet automated), this kind of measurement cannot be part of day to day operation. However knowing the phase dependence of both the charge and the energy gain, the fast phase scan tool described above can be used. Having scanned the phase, the operator then just needs to adjust the phase +40 deg from the phase where the first charge is detected. This is then the phase for maximum energy gain.

Buncher Cavity

Calibration of the buncher phase essentially means finding the phase difference $\Delta\phi$ between gun and buncher for maximum energy and maximum bunching respectively. To this end a $\Delta\phi$ scan needs to be performed using the phase shifter, whilst measuring the energy gain due to the buncher cavity at constant gun amplitude and phase. From the phase shifter characterization measurements shown above

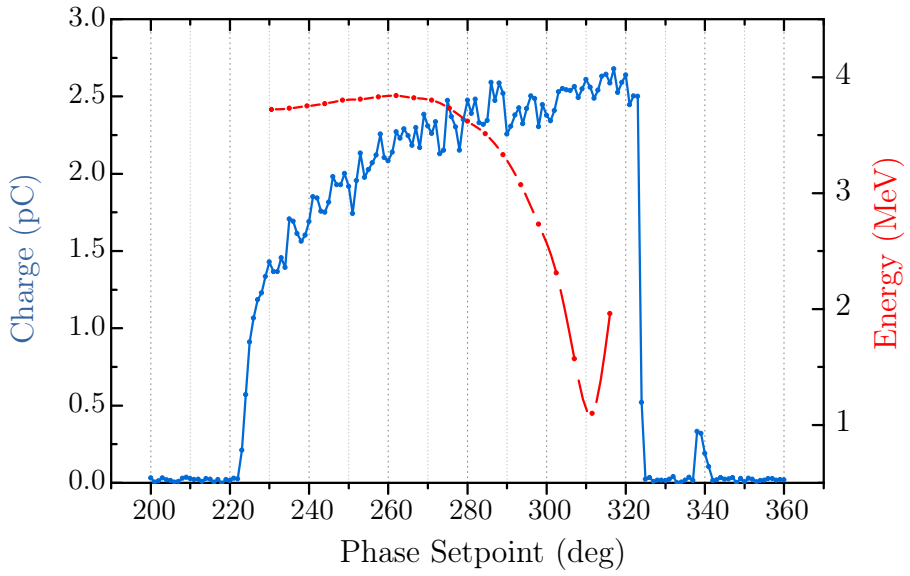

Figure 2.20: Phase scan for both the charge at the DDC1 Faraday cup and the mean beam energy, measured using the spectrometer arm. The buncher had been detuned during the energy measurements. Hence effects due to the buncher have been minimized.

it is now known that all of the four important parameters for this measurement (amplitude and phase for each cavity) are altered when the phase shifter is used. Therefore in order to keep the gun parameters constant, the klystron settings need to be adjusted for every scan step. Figure 2.21 shows the results of such a measurement. The black data points correspond to the raw measurement data. Since the buncher amplitude changed during the measurement, the data needed to be corrected using the knowledge of the phase shifter behavior. This corrected data now represents the phase dependent energy gain due to the buncher cavity at constant amplitude. It can be seen that the data fits the expected sine shape (see section 3.2.1). Using this measurement, the $\Delta\phi$ for maximum energy gain can now be determined. For the gun energy of 2.96 MeV that was used for this measurement $\Delta\phi_{\mathrm{max}} = -197\,\mathrm{deg}$, which corresponds to a phase shifter setting of 39.5 mm for both arms. The bunching phase is then $\Delta\phi_{\mathrm{max}} - 90\,\mathrm{deg}$.

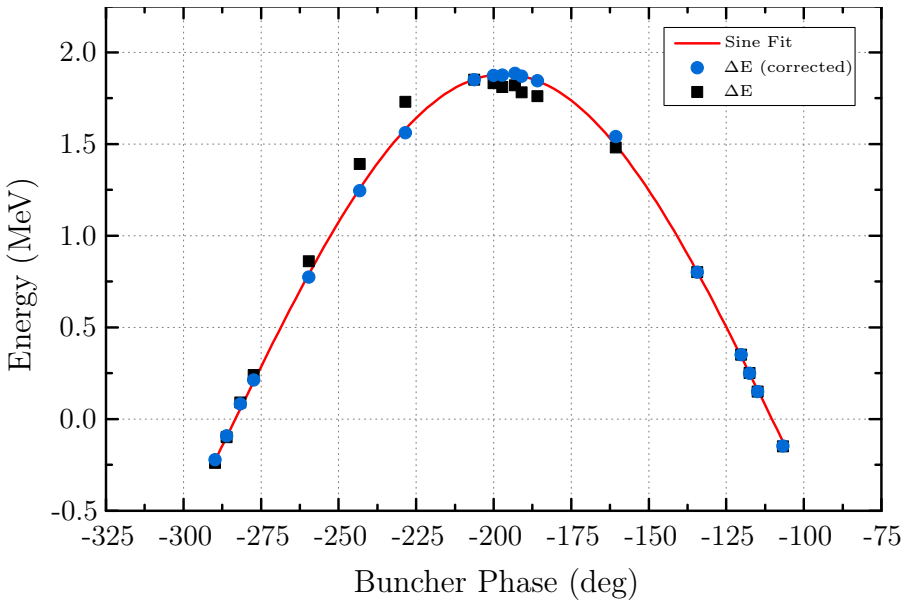

Figure 2.21: Phase scan for the energy gain due to the buncher cavity. Gun amplitude and phase have been kept constant during the scan. The corrected values have been corrected according to the change in buncher amplitude during the scan.

2.6 RF System Characterization Measurements

2.6.1 Measurement of the Cavity Mode Spectra

In order to characterize how both the gun and buncher cavity behave inside the REGAE setup it is important to know their mode spectra. To this end the forward gain (S21) parameter has been measured using a network analyzer (NWA). The amplified signal has been coupled into the respective cavity using the reflected power port of the directional coupler, which is installed right before the cavity. The scattering parameter S21 has then been measured via the probe antenna. This is also the reason for the need of amplification of the NWA signal. The forward port of the directional coupler was closed with a short. All recorded data presented in the following are averaged over 64 consecutive measurements. Figures 2.22 and 2.23 show the results of an NWA frequency sweep for the gun and the buncher respectively. For the gun one can identify the two fundamental modes (0- and π-mode) at 2988.5 Mhz and 2998.0 MHz. Please note that the accuracy is limited by the NWA. Looking closer at the data, another mode close to the π-mode can be found at 2999.0 MHz (highlighted in green). Figure 2.24 shows the results of two measurements closer around this frequency region (blue curve:

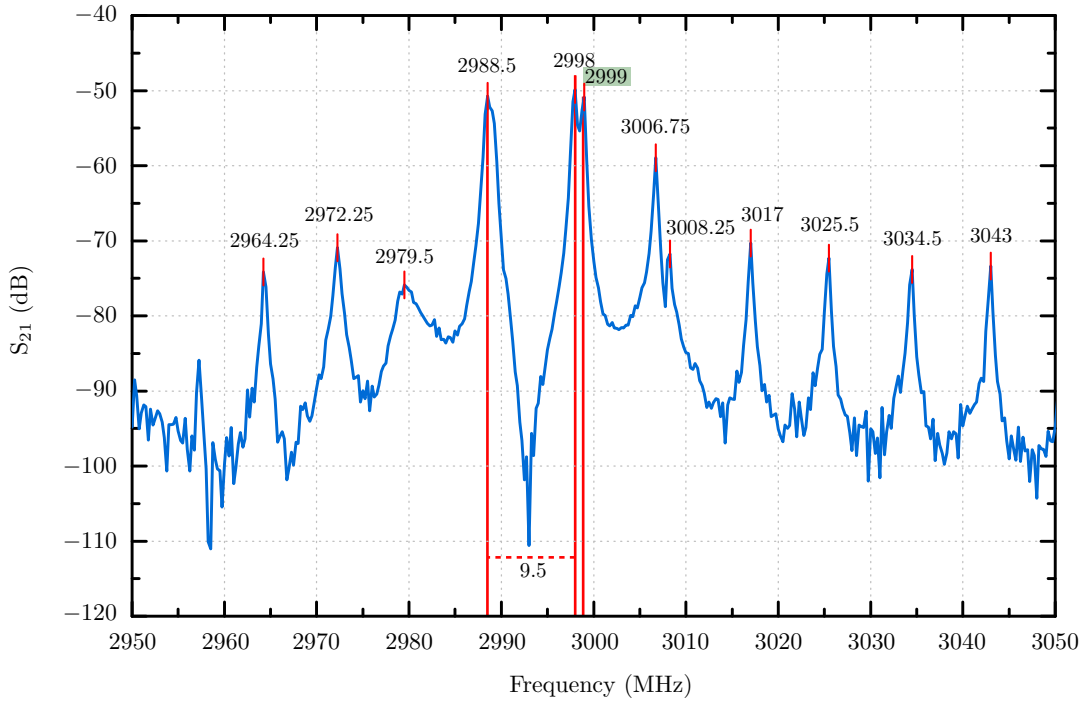

Figure 2.22: Frequency dependent forward gain of the gun cavity.

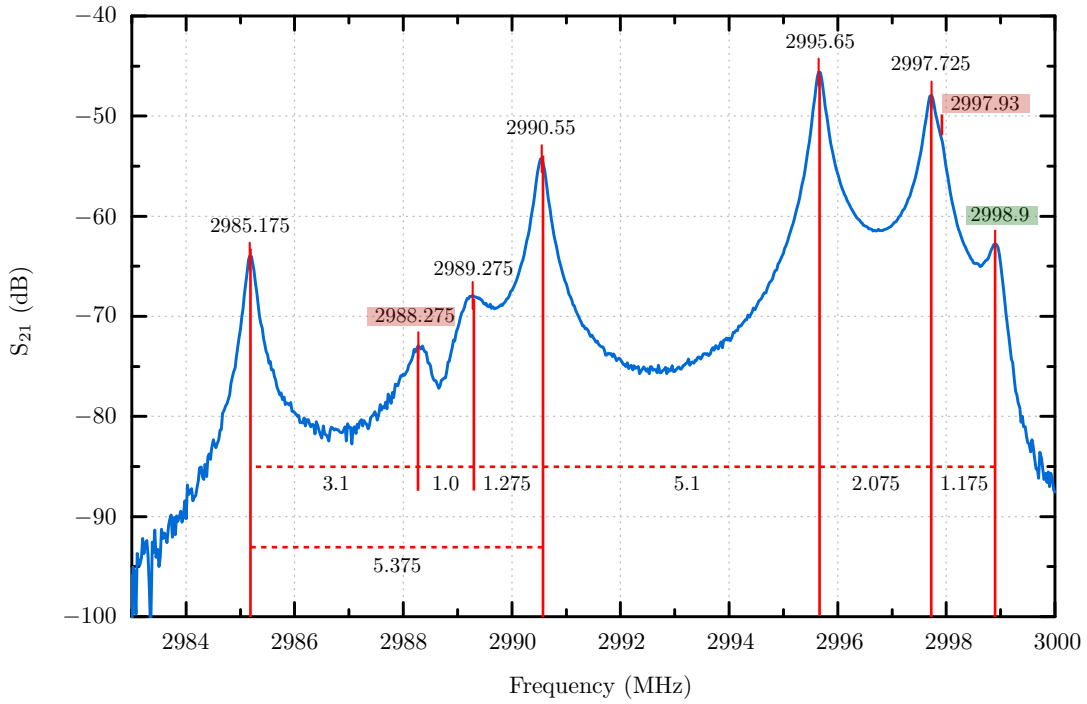

Figure 2.23: Frequency dependent forward gain of the buncher cavity.

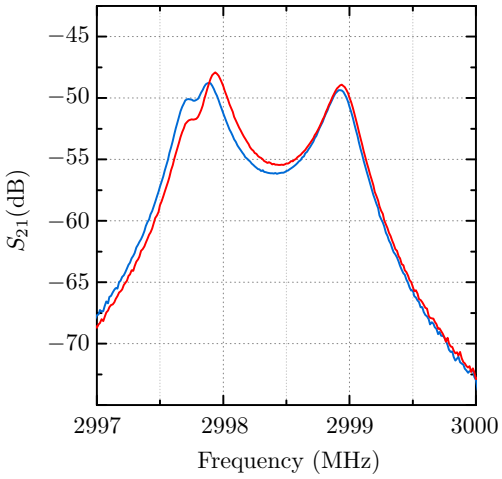

Figure 2.24: Comparison of two frequency sweeps for different gun temperatures. Red curve: Cavity temperature reduced by 1 °C.

first measurement, red curve: second measurement). For the second measurement the gun temperature had been reduced by 1 deg. It can be seen that the lower frequency mode shifts to higher frequencies for lower temperatures (from the data: approximately 50 kHz/deg). The higher frequency mode does however not move. Therefore this resonance must stem from the klystron itself. In addition to the gun modes and the klystron resonance the measurement also reveals a number of other modes, which occur in a periodicity of approximately 8 MHz. In order to understand this structure, it is useful to look at the dependence of the so called *input impedance* $Z_{\mathrm{in}}(\omega)$ on the load impedance Z_{L} (klystron) and the waveguide impedance Z_0. It reads

$$Z_{\mathrm{in}}(\omega) = \frac{Z_{\mathrm{L}} + i \cdot Z_0 \tan(l \cdot \frac{\omega}{c})}{1 + i \cdot \tan(l \cdot \frac{\omega}{c}) \cdot \frac{Z_{\mathrm{L}}}{Z_0}}, \tag{2.65}$$

where l is the length of the waveguide. It can be derived using basic (lossless) transmission line theory ([17]). The Impedance along a transmission line is given by the usual expression

$$Z(z) = \frac{V(z)}{I(z)}. \tag{2.66}$$

The voltage and current can be obtained as solutions to the wave equations 2.1, with a forward traveling and a backward traveling part. Therefore

$$V(z) = V_{0,+}e^{-ikz} + V_{0,-}e^{ikz} = V_{0,+}(e^{-ikz} + \Gamma e^{ikz}), \tag{2.67}$$

where $V_{0,-} = \Gamma V_{0,+}$ with

$$\Gamma = \frac{Z_L - Z_0}{Z_L + Z_0} \tag{2.68}$$

the *reflection coefficient*. Note that for a matched impedance $\Gamma = 0$ and hence no reflection occurs. The current is then given by

$$I(z) = \frac{V_{0,+}}{Z_0}(e^{-ikz} - \Gamma e^{ikz}). \tag{2.69}$$

It is now possible to calculate $Z(z)$ using equation 2.68 and *Euler's formula*.

$$\begin{aligned} Z(z) &= Z_0 \cdot \frac{V_{0,+}(e^{-ikz} + \Gamma e^{ikz})}{V_{0,-}(e^{-ikz} - \Gamma e^{ikz})} \\ &= Z_0 \cdot \frac{(Z_L + Z_0)e^{-ikz} + (Z_L - Z_0)e^{ikz}}{(Z_L + Z_0)e^{-ikz} - (Z_L - Z_0)e^{ikz}} \\ &= Z_0 \cdot \frac{Z_L \cos(kz) - i \cdot Z_0 \sin(kz)}{Z_0 \cos(kz) - i \cdot Z_L \sin(kz)} \\ &= \frac{Z_L - i \cdot Z_0 \tan(kz)}{1 - i \cdot \tan(kz) \cdot \frac{Z_{\mathrm{L}}}{Z_0}}. \end{aligned} \tag{2.70}$$

Inserting $k = \omega/c$ and $z = -l$ (which is the usual definition for the input impedance) yields equation 2.65. If waveguide and klystron impedances are not matched, a periodic structure on the input impedance results. Therefore the periodic occurrence of the peaks in figure 2.22 might be due to an impedance mismatch between klystron and waveguide during the measurement.

The buncher cavity measurements have been conducted the same way as the gun cavity measurements. They reveal the four fundamental modes at 2985.2 MHz (0), 2990.6 MHz ($\pi/3$), 2995.7 MHz ($2\pi/3$) and 2997.7 MHz (π). In addition to that, the two gun modes are also visible in the spectrum (highlighted in red), which is a sign of crosstalk between the cavities. The klystron resonance is again visible at approximately 2999 MHz (highlighted in green). It can be seen that the π- and $2\pi/3$-modes are only separated by approximately 2 MHz (as it has already been seen in the CST simulations). The next sections will focus on the implications of this circumstance and the crosstalk between the two cavities.

2.6.2 REGAE RF Pulses

In the preceding section the measurement of the cavity modes has been discussed. In normal operation, the cavities are driven in their π-mode, the mode with the highest frequency. Unfortunately due to the short RF pulses, which have — at the time of this thesis — a configured length of 6 μs, the adjacent other modes can be excited. This is because a short pulse has a large bandwidth and is hence capable of exciting multiple modes. Another effect that has to be taken into account is the fact that a small mode spacing can result in an overlap of the tails of the adjacent resonance curves and hence a perturbation of the individual modes. Figure 2.25 shows an actual measurement of the temporal RF pulse shape for both the gun and the buncher cavity using the probe antennas. In addition to that, a small section of the decaying part of the pulse is also shown. Here the exponential part of the pulse has been removed, in order to isolate the oscillations. When two oscillations with close frequencies ν_1 and ν_2 are super-imposed, the frequency of the envelope of the resulting oscillation is then given by

$$\nu_B = |\nu_2 - \nu_1|. \tag{2.71}$$

This phenomenon is called *beat* and ν_B is the *beat frequency*. The oscillations on the pulses can now be interpreted as a beat between several adjacent modes and is most prominent in the filling and the decay part of the pulse. Using FFT, the beat frequencies can be identified and compared to the modes found in the preceding section. The expected result would be frequencies corresponding to the mode spacing between the π-mode and the other cavity modes. Table 2.6

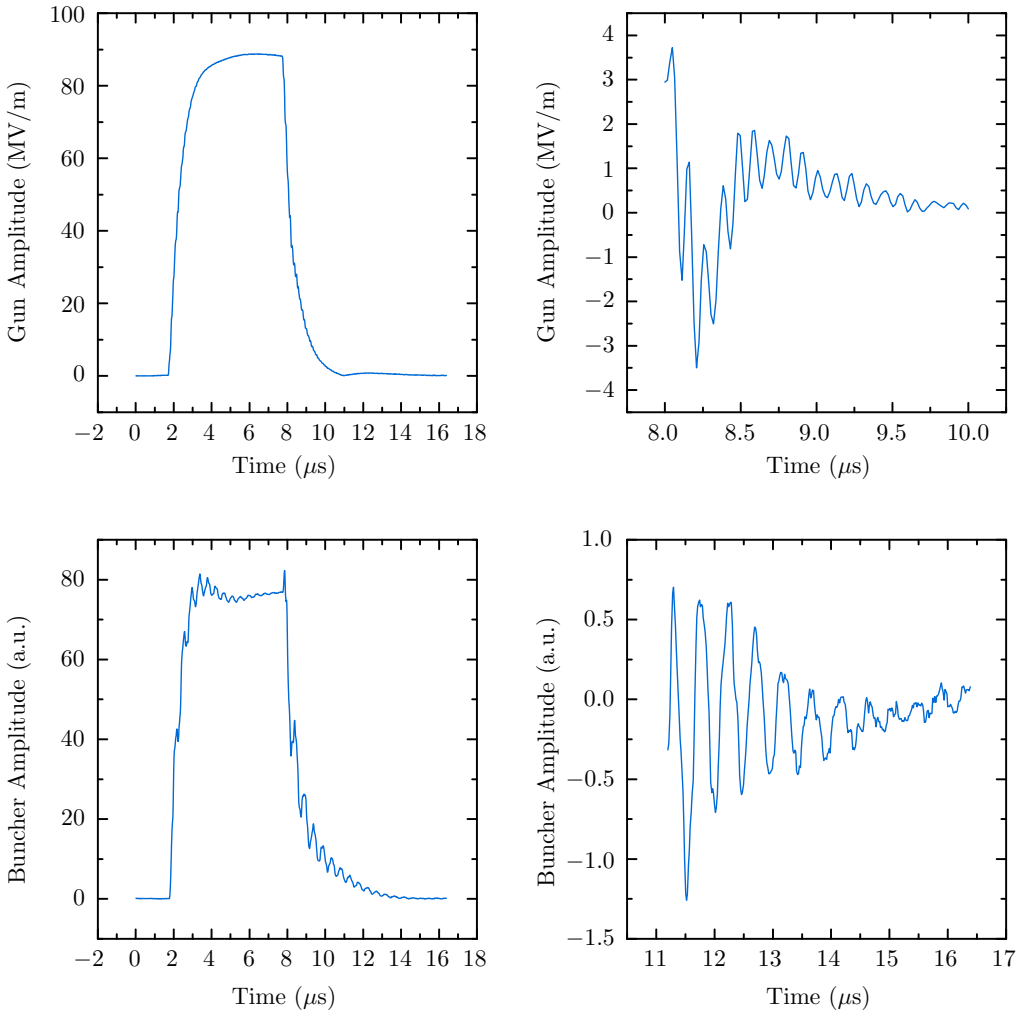

Figure 2.25: Measurement of the time dependent cavity field amplitude via the probe antenna for the gun (top) and the buncher (bottom).

Table 2.6: Dominant beat frequencies extracted from the pulse data shown in figure 2.25 via FFT analysis.

Gun		**Buncher**	
ν_B (MHz)	Rel. Amplitude	ν_B (MHz)	Rel. Amplitude
1.49	1.00	2.11	1.00
9.42	0.80	7.21	0.13
		9.62	0.08

shows the results of an FFT analysis of the pulse data. This data can now be compared to the RF measurements above (fig. 2.22 and 2.23). The gun pulse contains two main frequencies at 1.49 MHz and 9.42 MHz, where the lower one can be attributed to the mode spacing between the gun π-mode and the klystron, the second one corresponds to the mode spacing between the gun's two main modes and is the dominant frequency. For the buncher three frequencies can be identified and the most dominant is the 2.11 MHz, which corresponds to the spacing between the buncher's π-mode and its adjacent mode. The next frequency component, 7.21 MHz, can be attributed to the spacing between the π-mode and the buncher's third mode. Since the last contribution at 9.62 MHz corresponds to the spacing between the buncher π-mode and the gun $0-$mode, even the crosstalk between the cavities can be identified. It has to be noted that the frequencies do not exactly match the ones measured using the NWA. This has several reasons.

- The beat structure on the pulses is strongly dependent on the individual tuning of the cavities.
- The cavities could have been tuned differently during the RF measurements.
- The temporal resolution of the pulse data is limited to 1024 samples at 62.5 MHz, which also limits the FFT resolution.
- The resolution of the NWA measurements has been limited due to the large frequency span.

Analytical Description of the Phenomenon

In order to understand this beat phenomenon, one can describe the multi-mode cavity by a series of parallel RLC-circuits, which represent the individual cavity modes ([22]). Using Kirchoff's law, the differential equation for an externally

driven RLC-circuit is given by

$$C\partial_t^2 V + \frac{\partial_t V}{R} + \frac{V}{L} = \partial_t I_d, \tag{2.72}$$

where $\partial_t I_d$ is the driving term. The quality factor of a parallel RLC-circuit is given by

$$Q = R\sqrt{\frac{C}{L}}. \tag{2.73}$$

Therefore equation 2.72 can be expressed as

$$\partial_t^2 V + \frac{\omega_m}{Q}\partial_t V + \omega_m^2 V = -\frac{\omega_m}{Q} V_d, \tag{2.74}$$

where $\omega_m = 1/\sqrt{LC}$ is the resonant frequency of the mode. The driving voltage V_d is the voltage as observed in the cavity, which can be related to the voltage supplied by the klystron by the so called *transformer ratio*

$$n = \sqrt{\frac{R_s}{2Z_c\beta}}, \tag{2.75}$$

where R_S is the shunt impedance, β is the coupling coefficient and Z_c is the impedance of the waveguide mode. The voltage is then given by $V_d = n \cdot V_{ext}$. Now the voltage in the oscillation resonant mode can be related to the common quantities that have been derived in section 2.1. Assuming that the mode separations are larger than the width of the individual resonance curves, the overall cavity voltage can be expressed as the sum of the mode contributions that can be calculated using equation 2.74. In [23] the differential equation has been solved for a flat-top input pulse of length T, which is defined by

$$\frac{V(t)}{V_0} = H(t) \cdot \left(1 - e^{-t/\tau}\right) - H(t-T) \cdot \left(1 - e^{-(t-T)/\tau}\right), \tag{2.76}$$

where $H(t)$ is the *Heaviside step function*, τ is the rise/fall time and V_0 is the maximum voltage. The lengthy result of the calculation can be found in [23] and is omitted here for brevity. The mode voltage is then a function of $n, \beta, \Psi, Q, \omega_m$ and ω_d, where Ψ is the tuning angle as defined in equation 2.38 and ω_d is the frequency of the driving signal. Figure 2.26 shows the calculated pulse shapes for the gun and buncher cavity. The parameters have been extracted from the Microwave Studio simulations that have been discussed in section 2.2. In order to estimate the detuning of the cavities on the day the pulses shown in figure 2.25 have been recorded, the cavity temperatures have been taken from the archive. It

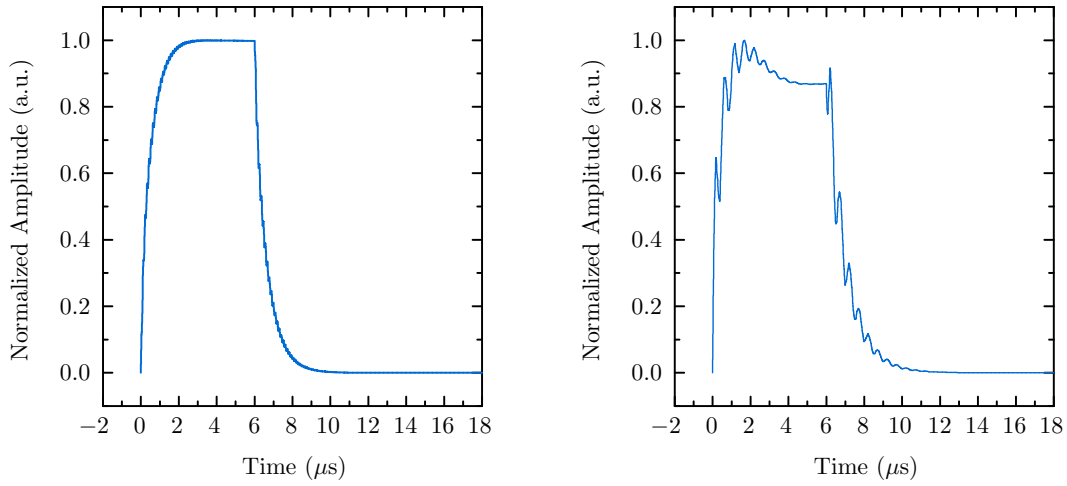

Figure 2.26: Calculated pulses shapes for the gun (left plot) and buncher (right plot). The pulses have been calculated using the solution to equation 2.74 and RF parameters from the simulations shown in section 2.2. Cavity detuning has been estimated using archived cavity temperature data.

is important to note that the calculations are based on a perfect flat top, whereas the real REGAE pulse might not have been perfectly flat. It can be seen that the analytically calculated pulses are very close to the measured pulse shapes. This leads to the conclusion that the beat structure indeed stems from contributions of adjacent oscillating modes.

Effect of the Beats on the Electron Bunch

As it has been stated above, the total field in the cavity is the sum of the fields of the excited modes. This total field, as a result, has now a slightly different phase advance between the cavity cells compared to single mode operation. This can have an effect on transverse, as well as longitudinal beam parameters and dynamics. Since the investigation of these effects is not in the scope of this thesis, two effects will be presented that have been observed by other groups.

At the SLAC Gun Test Facility (see [24]) it has been measured that the phase advance in their 1.6 cell GTF gun for π-mode operation is 187 deg instead of 180 deg. The difference in phase in the half cell is reported to be 5 deg. The GTF gun has a mode spacing between 0- and π-mode of 3.5 MHz. Due to this different phase advance, the RMS energy spread has been measured by the authors to be approximately 3.5 times higher than in the simulated single mode case at linac

phase of 0 deg. It has to be noted though that this is not an absolute increase of the energy spread, but a shift of the minimum towards different phases. An increase in mode spacing has been shown in [23] to decrease the effects on the energy spread dramatically. In addition to the energy spread, the emittance due to the time dependent RF field has been reported in [25]to be reduced by a factor of approximately 1.9 by increasing the 0-π mode spacing from 3.5 MHz to 15 MHz. This emittance contribution is important in cases where the space charge induced emittance growth is small (also see [25]).

Since the REGAE gun has a mode spacing of approximately 9.5 MHz, the effects on beam dynamics should be small, but this has to investigated in the future. The RF induced transverse emittance is given by ([22])

$$\epsilon_x^{\mathrm{RF}} = \frac{k^3\alpha}{\sqrt{2}} \cdot \sigma_x^2\sigma_z^2, \tag{2.77}$$

where α is the normalized vector potential and k the wavenumber. Therefore for the REGAE bunch parameters (short bunch $< 10\,fs$ RMS and spot size $5\,\mu$m RMS) this contribution is negligible, which has been tested and verified through simulations ([26]). It has to be noted that the mode spacing between the buncher cavity modes is much smaller ($2\pi/3-\pi$ spacing is approximately 2 MHz). Therefore it has to be investigated in what extent this affects the performance of the cavity in bunching mode.

2.6.3 Fine Tuning of the Cavities

Mechanical tuning of the accelerating cavities can only be done up to a certain accuracy that depends on the actual tuning method. Another reason is the fact that the cavities are in the final RF setup part of a circuit. In order to cope with this situation, the dependence of the resonance frequency of the cavity on the temperature can be utilized. This dependence is simply the result of the expansion/contraction of the material. A measurement of the temperature dependent reflected RF signal at the cavity can thus be used to determine the optimal cavity temperature and hence as a means of fine tuning. The cavity at the temperature that minimizes the reflected signal is then tuned to the frequency of the incoming wave.

Using a MATLAB tool that controls the cavity heaters, the temperature of both the gun and the buncher cavity has been scanned, whilst recording the forward and reflected wave at the cavity. As it has already been shown, the single klystron setup at REGAE leads to crosstalk between the cavities. In order to investigate this circumstance, two measurements have been performed for each cavity: One

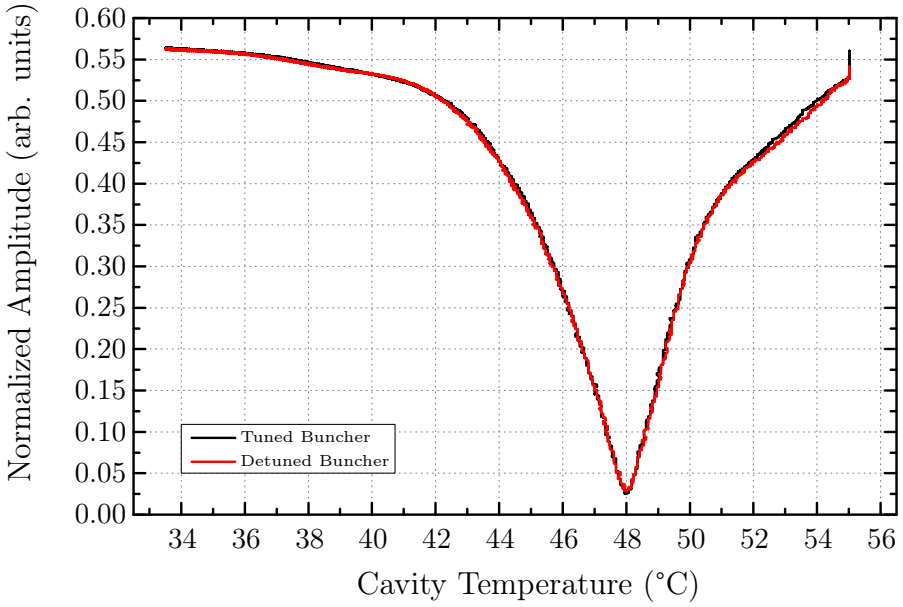

Figure 2.27: Temperature scan of the gun cavity for two different settings. The optimal temperature has been determined to be $T_{0,\mathrm{g}} = 48.0\,^{\circ}\mathrm{C}$.

with the other cavity tuned and the second with the other cavity detuned far off resonance (at 55 °C). The results are shown in figures 2.27 and 2.28. The best tuning temperatures have been determined to be

$$\begin{aligned} T_{0,\mathrm{g}} &= 48.0\,^{\circ}\mathrm{C}, \\ T_{0,\mathrm{b}} &= 38.6\,^{\circ}\mathrm{C}. \end{aligned} \tag{2.78}$$

It can be seen that the gun cavity is not perturbed by the buncher cavity, as both scans result in nearly the same curve. The temperature scan for the buncher on the other hand shows some interesting features. In the range of the scan three modes can be identified (three dips). The first one at 38.6 °C has the strongest coupling. This is the π-mode of the buncher. The second one at approximately 41.7 °C is much more pronounced in the tuned-gun case and can hence be identified as cross-coupling of the gun π-mode. The third one has a very weak coupling and does shift to lower temperatures in the detuned-gun case due to the weaker cross-coupling between the cavities. It can also be seen that the crosstalk between the cavities diminishes the coupling of the buncher π-mode.

In order to quantify the effect of the crosstalk on the coupling of the modes, the *complex reflection coefficient* Γ can be calculated from the data. The data consists of amplitude (A_{FW} and A_{REF}) and phase (ϕ_{FW} and ϕ_{REF}) signals from the directional couplers right in front of the respective cavity (note that the phase

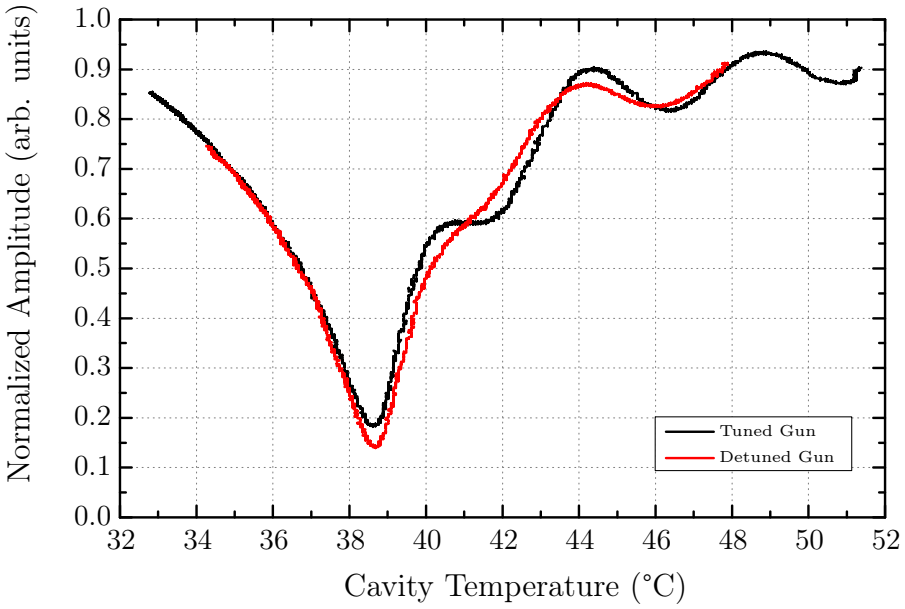

Figure 2.28: Temperature scan of the buncher cavity for two different settings. The optimal temperature has been determined to be $T_{0,\mathrm{b}} = 38.6\,^{\circ}\mathrm{C}$.

signals are given in degrees instead of radians). The complex signal is now defined as

$$a_{\mathrm{FW/REF}} = A_{\mathrm{FW/REF}} \cdot \exp(i\phi_{\mathrm{FW/REF}} \cdot \pi/180) \tag{2.79}$$

and the complex reflection coefficient:

$$\Gamma = \frac{a_{\mathrm{REF}}}{a_{\mathrm{FW}}}. \tag{2.80}$$

The complex reflection coefficient can then be plotted in the complex plane. For a single resonance, Γ describes a circle in the complex plane (see derivation below). Figures 2.29 and 2.30 show the results for the gun and the buncher cavity respectively. Looking at the data, it can be seen that the reflection coefficients — in the case of the REGAE cavities — do not describe an ideal circle. Instead a combination of several circles, or spiral can be seen. These kinds of shapes in the complex reflection coefficient have been shown by Dohlus et al. to result from multiple closely spaced modes (see [27]). The shape of the reflection coefficients evolution in the complex plane therefore confirms the results that have been presented above.

It has been shown ([28]) that the coupling coefficient β can be extracted from Γ using a circle fit in the complex plane that determines the center position and the radius. This can be derived the following way. Starting from equation 2.72

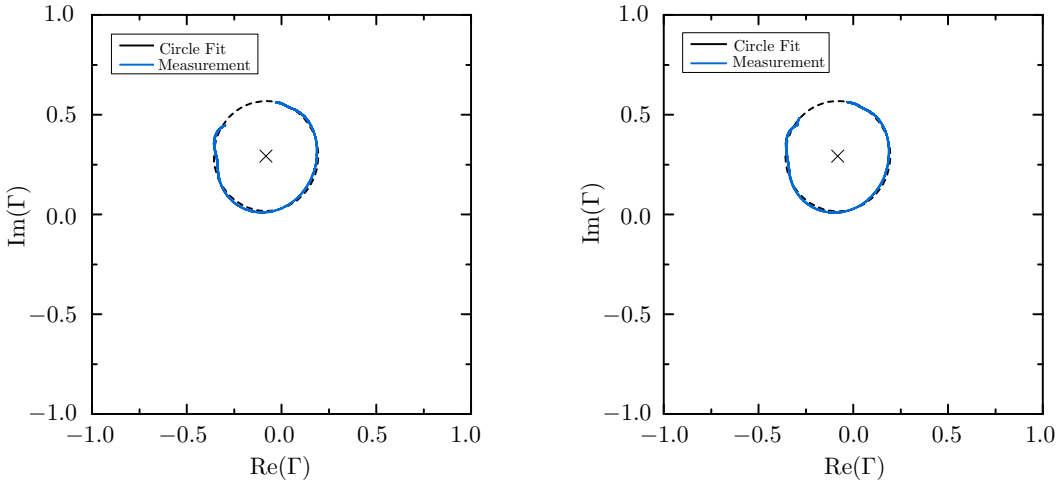

Figure 2.29: The complex reflection coefficient measured for the gun cavity, plotted in the complex plane together with a circle fit. The left plot shows the case where the buncher cavity had been tuned. On the right the case where the buncher cavity had been detuned is shown.

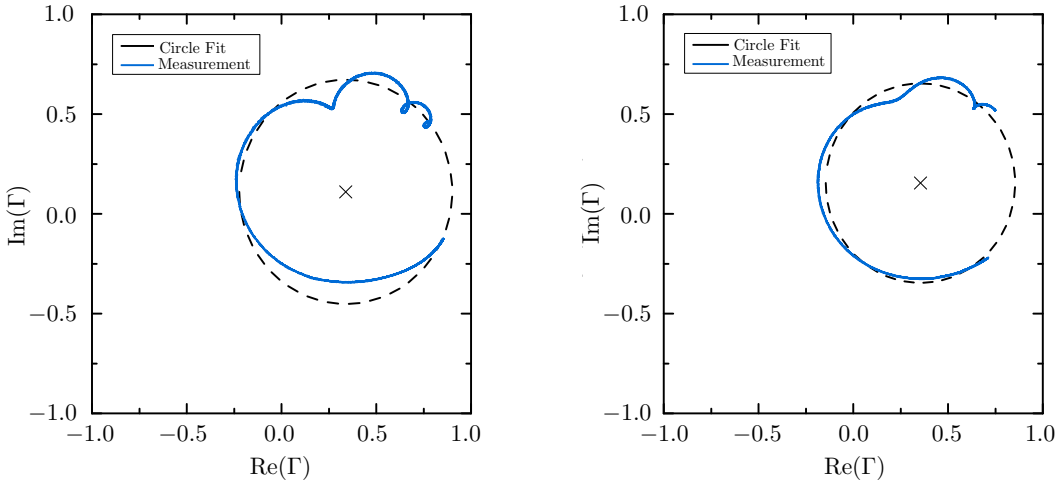

Figure 2.30: The complex reflection coefficient measured for the buncher cavity, plotted in the complex plane together with a circle fit. The left plot shows the case where the gun cavity had been tuned. On the right the case where the gun cavity had been detuned is shown.

(differential equation of the RLC resonator) and assuming that the external driving voltage is given by a harmonic function of the form

$$V_{\text{ext}}(t) = (V_{\text{ext,r}}(t) + iV_{\text{ext,i}}(t)) \cdot \exp(i\omega t), \tag{2.81}$$

i. e. an slowly varying envelope and a fast oscillating term, one can separate the resulting differential equation into real and imaginary parts, yielding

$$\begin{aligned} \partial_t^2 V_r + \frac{\omega_o}{Q}\partial_t V_r - 2\omega\partial_t V_i - \omega^2 V_r - \frac{\omega\omega_0}{Q}V_i + \omega_0^2 V_r &= \frac{\omega_0}{Q}\partial_t V_{\text{ext,r}} - \frac{\omega\omega_0}{Q}V_{\text{ext,i}} \\ \partial_t^2 V_i + \frac{\omega_o}{Q}\partial_t V_i + 2\omega\partial_t V_r - \omega^2 V_i + \frac{\omega\omega_0}{Q}V_r + \omega_0^2 V_i &= \frac{\omega_0}{Q}\partial_t V_{\text{ext,i}} + \frac{\omega\omega_0}{Q}V_{\text{ext,r}}. \end{aligned} \tag{2.82}$$

In the appendix of [29] the author introduces the assumptions $Q \gg 1$, $\omega_{1/2} \ll \omega_0$ and $\Delta\omega \ll \omega_0$, where $\omega_{1/2}$ is the half-bandwidth of the resonator and $\Delta\omega$ is the detuning as a means to simplify equation 2.82 In addition to that, the small second order terms can be neglected. Thus the following approximation can be found, which is appropriate in the case of accelerator cavities:

$$\begin{aligned} \partial_t V_r &= -\omega_{1/2}V_r - \Delta\omega V_i + \omega_{1/2}V_{\text{ext,r}} \\ \partial_t V_i &= \Delta\omega V_r - \omega_{1/2}V_i + \omega_{1/2}V_{\text{ext,i}}. \end{aligned} \tag{2.83}$$

Combining real and imaginary part and neglecting the fast oscillating part, one gets

$$\begin{aligned} \partial_t V &= V_r + iV_i \\ &= V_r(i\Delta\omega - \omega_{1/2}) + V_i(-\Delta\omega - i\omega_{1/2}) + \omega_{1/2}V_{\text{ext}} \\ &= V_r(i\Delta\omega - \omega_{1/2}) + iV_i(i\Delta\omega - \omega_{1/2}) + \omega_{1/2}V_{\text{ext}} \\ &= (i\Delta\omega - \omega_{1/2})V + \omega_{1/2}V_{\text{ext}}. \end{aligned} \tag{2.84}$$

This is the so called *envelope equation*. The cavity voltage V in this equation is given by the sum $a_{\text{FW}} + a_{\text{REF}}$. Introducing the reflection coefficient for zero detuning Γ_0 (due to impedance mismatch), the external driving voltage can be written as $V_{\text{ext}} = (1 + \Gamma_0) \cdot a_{\text{FW}}$. Using equation 2.80, the complex reflection coefficient for steady state condition ($\partial_t V = 0$) now reads

$$\Gamma = (1 + \Gamma_0) \cdot \frac{\omega_{1/2}}{\omega_{1/2} + i\Delta\omega} - 1. \tag{2.85}$$

This expression — in the complex plane — describes a circle, if plotted for different values of $\Delta\omega$. All of the derivations that have been shown so far are based on the assumption of perfectly calibrated field probes and directional couplers. In reality

the measured signals are subject to calibration errors in amplitude and phase. Therefore (without any crosstalk in the directional couplers)

$$\begin{aligned} a_{\mathrm{FW}} &= A \cdot \tilde{a}_{\mathrm{FW}} \\ a_{\mathrm{REF}} &= B \cdot \tilde{a}_{\mathrm{REF}}, \end{aligned} \tag{2.86}$$

with the complex correction factors A and B. The measured values are denoted by the tilde. Recalling the definition of the reflection coefficient (equation 2.80), it can be seen that the real reflection coefficient differs from the measured value by a factor of B/A. This fact makes the interpretation of the plots 2.29 and 2.30 difficult, because the plotted values are scaled. In order to overcome this problem, Brandt et al. have found a relation between the reflection coefficient Γ_0 and the properties of the circle ([28]):

$$\Gamma_0 = -\frac{B}{A}(|c| - r)\frac{c}{|c|} = -\frac{|c| - r}{|c| + r}, \tag{2.87}$$

where c is the center of the circle fit and r is the radius. It can be seen that the calibration errors are already included. Using the definition for the coupling coefficient

$$\beta = \frac{1 + \Gamma_0}{1 - \Gamma_0}, \tag{2.88}$$

it is now possible to compare the coupling coefficients for the different cases in order to determine the effect of the crosstalk on the coupling. The following calculations have been performed according to the derivation above and using a circle fit algorithm that was proposed by Pratt in [30]. Only the data close to the resonance temperature has been used for the fit. The results are shown in table 2.7. It can be seen that the crosstalk between the cavities reduces the coupling in both cases. For the gun the coupling is reduced by approximately 0.77 %, which is negligible. In contrast to that, the buncher coupling is reduced by approximately 9.94 %.

Table 2.7: Coupling coefficients β_{gun} and β_{bun} calculated from the complex reflection coefficients for the gun and buncher cavity.

	β_{gun}	β_{bun}
Crosstalk	0.906	0.634
No crosstalk	0.913	0.704

2.6.4 Characterization of the REGAE Gun Cavity II

The new REGAE gun cavity features a newly designed cathode holder which incorporates a new spring that resembles the ones used for vacuum tube holders. This eliminates the problem that the probability of damaging the spring during cathode exchange had been very high with the previous design.

In order to characterize the modified gun cavity, the following measurements have been conducted using a *Hewlett Packard 8720C* network analyzer (NWA):

- Measurement of the π- and 0-mode
- Reproducibility of the cathode position
- Measurement of the E-field profile using the *bead-pull technique*

In order to guarantee optimal results, the NWA has been recalibrated using the *Agilent 85032 B Type N Calibration Kit* prior to every measurement.

Measurement of the π- and 0-Mode

The π- and 0-mode has been determined by measurement of the *S11 scattering parameter* using the NWA at room temperature (22 °C) in air. In addition to the resonant frequencies the bandwidth, the coupling (minimal S11) and the loaded quality factor Q_L has been measured. The results are shown in table 2.8. Due to the better coupling of the π-mode, the measured loaded Q-factor of this mode is lower than the quality factor of the 0-mode.

Table 2.8: Measurement results for the π-mode and 0-mode.

	f (MHz)	**BW (kHz)**	Q_L	**S11 (dB)**
0-Mode	2986.512	349	8517	-11.062
π-Mode	2996.206	462	6522	-22.468
Delta	9.694	113	-1995	-11.406

The reflection coefficient Γ which describes the ratio between reflected to forward power, is related to S11 by

$$\Gamma^2 = 10^{\frac{S11}{10}} \tag{2.89}$$

and to the coupling coefficient β by

$$\beta = \frac{1+\Gamma}{1-\Gamma}. \tag{2.90}$$

The square in the first equation introduces an ambiguity, i.e. it is not a priory clear whether the coupling is overcoupled ($\beta > 1$) or undercoupled ($\beta < 1$). The coupling of the 0-mode hence yields $\beta = 1.77$ or $\beta = 0.56$, from which the unloaded quality factor is calculated as $Q_0 = (1 + \beta)Q_L = 23592$ or $Q_0 = 13286$.The first value is significantly higher than expected from theory, thus an undercoupled case with $\beta = 0.56$ can be concluded. For the π-mode $\beta = 1.16$ or $\beta = 0.86$ and $Q_0 = 14087$ or $Q_0 = 12131$, respectively. The theoretically expected quality factor indicates again an undercoupled case. In the REGAE experiment the gun cavity is operated at T = 40 to 45 °C and in vacuum. Therefore a correction has to be applied to the measurement shown in table 2.9:

Table 2.9: Measurement results for the π-mode and 0-mode.

Source	**Correction**
Vacuum	+0.95 MHz
Temperature	-41.0 kHz/degree
Thread	+24 kHz

During the measurements a nylon thread is stretched through the cavity (see below for details). The thread reduces the resonance frequency of the cavity by 24 kHz. The temperature coefficient has been experimentally determined after tuning of Gun I and verified the values during operation. (For the tuning of Gun I 48.5 kHz/degree had been used.) Application of these corrections (assuming a temperature change of 20 °C and therefore a correction of -0.82 MHz) to the π-mode frequency results in the following detuning of the π-mode:

Table 2.10: Detuning of the new REGAE gun cavity (π-mode).

	f (MHz)
Design frequency (42 °C, vacuum, w. o. thread)	2998.000
Design frequency (22 °C, air, thread)	2997.850
Measured frequency (22 °C, air, thread)	2996.206
Corrected frequency (42 °C, vacuum, w. o. thread)	2996.360
Detuning	**-1.640**

Reproducibility of the Cathode Position

The reproducibility of the cathode position has been determined by measuring the π-mode frequency including the cathode and without the cathode being inserted.

Table 2.11: Reproducibility of the cathode position (π-mode).

	incl. Cathode		**without Cathode**	
	f (GHz)	S11 (dB)	f (GHz)	S11 (dB)
	2.9962007	-22.871	2.9982407	-15.650
	2.9961857	-22.048	2.9982407	-15.718
	2.9961857	-22.278	2.9982407	-15.821
	2.9961857	-22.503	2.9982407	-15.890
Average	**2.9961887**	**-22.461**	**2.9982407**	**-15.787**
Frequency shift due to the cathode: 2.052 MHz				

The results show that the repositioning of the cathode has almost no effect on the resonant frequencies. This implies that the cathode can indeed be repositioned very accurately into the new holder.

Figure 2.31: The new cathode holder with an inserted cathode dummy.

Measurement of the E-field Profile using the Bead-pull Technique

In order to measure the profile of the electric field inside of the gun cavity, the so-called *bead-pull technique* has been used, where a small metal bead is pulled

through the cavity using a thread. This bead then acts as a perturbation and therefore shifts the resonant frequencies of the cavity proportional to the square of the local electric field (see [31, 32]). It is thus possible to measure the z-dependent frequency shift (where the z-axis is the axis that is defined by the thread) by using a stepper motor. The spatial resolution of the measurement is defined by the length of the bead (∼5 mm). The length and wall thickness of the bead also determines the frequency shift which limits the accuracy of the field measurement.

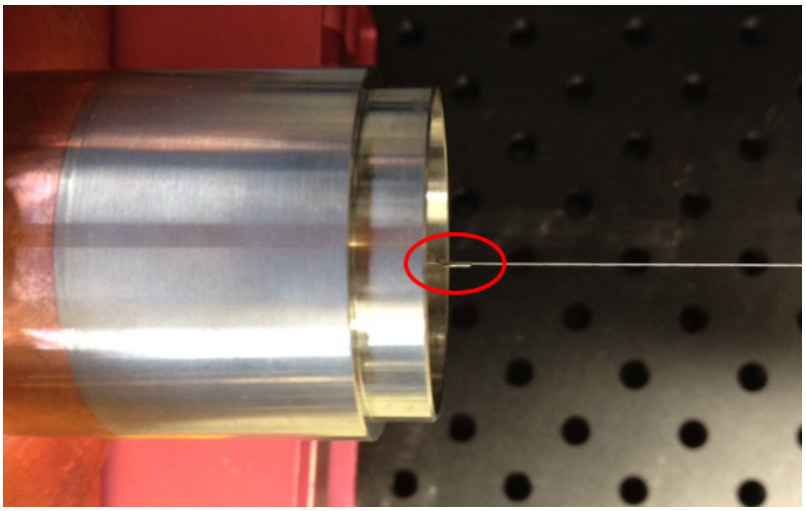

Figure 2.32: Small metal bead (marked by red circle) on a nylon thread in front of the coupler entrance.

The results of the bead-pull measurement using a nylon thread are shown in figure 2.33. Looking closer at the resonant frequencies for the bead being placed outside the cavity on the coupler and the cathode side respectively it can be seen that there is a small offset of 10 kHz for the 0-mode and 5 kHz for the π-mode. In order to investigate this offset, a second measurement has been conducted using a new thread of different material. The results are shown in figure 2.34. The offsets have been determined to be 0 Hz for the 0-mode and 3.1 kHz for the π-mode. This implies that the offset can be attributed to the perturbations due to the thread. It has to be noted that the perturbation is larger using the new thread due to a slightly larger bead. All following measurements have been made with the new bead/thread.

Tuning

To tune the cavity, the bottom of blind holes, which are located on the outer cylinder of each cavity cell, are deformed. The deformation allows shifting the

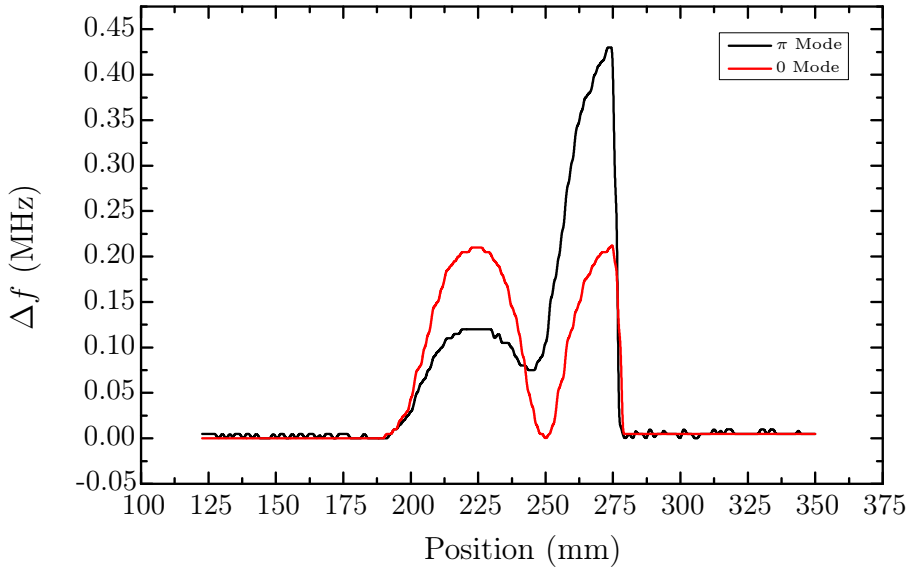

Figure 2.33: Bead-pull measurement using the nylon thread.

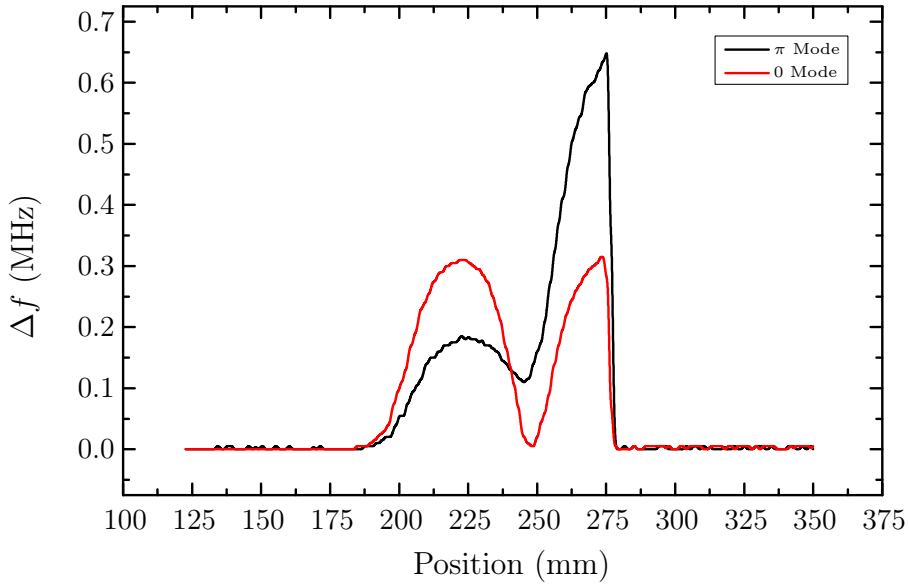

Figure 2.34: Bead-pull measurement using the new thread.

frequency only in one direction (upwards) and determines the field profile, i. e. the ratio of the peak field in the full cell to the peak field in in the half cell. The tuning has to be distributed to the cells such that the field profile stays close to 1. A slightly higher field in the half cell is preferable. Since the frequency measurement near the cathode hole is influenced by the cathode (e. g. when the bead touches the cathode) the exact determination of the field profile is in general difficult. The final frequency corresponds to an operation temperature of 39 °C.

Table 2.12: Frequency and field flatness for different tuning steps.

	Frequency (MHz)	**Field Flatness**
Start	2996.140	0.990
Step 1	2996.990	0.970
Step 2	2996.389	0.960
Turn Cavity	2996.380	0.970
Redo	2996.379	0.960
Step 3	2996.740	0.974

Final Measurements

Final measurements of the field profile of the $\pi-$ and the 0-mode are shown in figure 2.35 and summarized in table 2.13. For these measurements the averaging mode of the NWA and a small step size has been used, which leads to a smooth field profile and a field flatness of 0.99. The better coupling as compared to the first measurement (see table 2.8) in conjunction with the lower quality factor confirms an under-coupled case. The coupling coefficient and unloaded quality factor are determined as $\beta = 0.92$ and $Q_0 = 12230$.

Table 2.13: Measurement results for the π-mode and 0-mode after tuning.

	f (MHz)	**BW (kHz)**	Q_L	**S11 (dB)**
0-Mode	2988.037	357	8372	-11.4
π-Mode	2997.696	470	6370	-27.4
Delta	9.659	113	-2002	-16.0

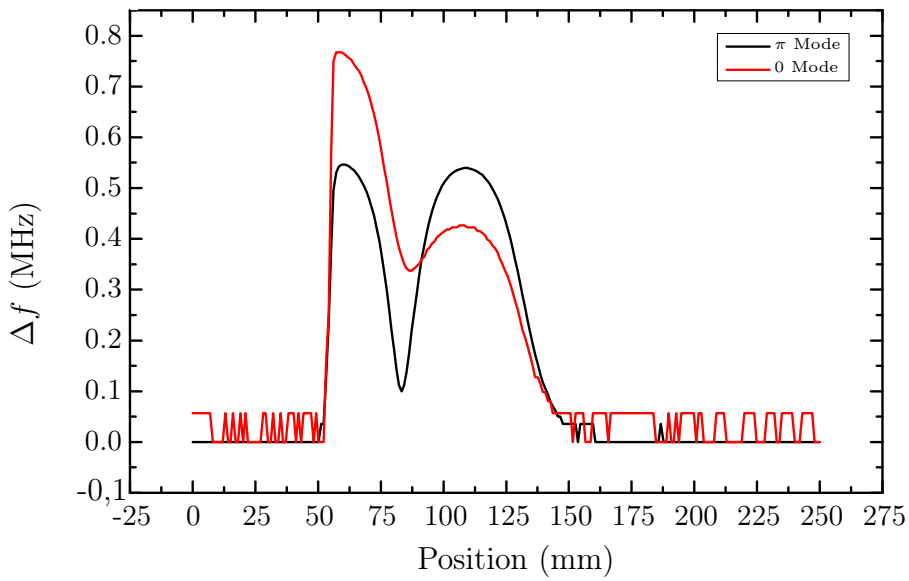

Figure 2.35: Field profile of the π-mode and 0-mode after tuning. Note: Cavity had been turned around.

3

Stability

In this chapter the stability of important parameters of the REGAE electron beam will be discussed. Since the stability of the beam parameters is ultimately the result of the stability of the whole REGAE machine, important machine parameters will be discussed. The state of the machine stability during this M.Sc. project will be presented and analyzed. Prior to the actual discussion of the current state of the machine, a so called *global sensitivity analysis* will be carried out using a method mainly based on work by Saltelli et al. ([33]) in conjunction with ASTRA simulations. Using the results of this analysis, the important factors for specific beam parameters that are crucial for the experiments presented in chapter 1 will be identified. To conclude the first part of this chapter, a more in-depth theoretical treatment of the time of flight sensitivity towards small phase changes will be deduced.

3.1 Global Sensitivity Analysis

As it has already been stated in the introduction to this chapter, the stability of beam parameters like *bunch time of flight*, *beam spot size*, etc. is ultimately the result of the stability of basic machine parameters like the *gun RF phase*, or the current of the solenoid lenses. Sometimes the effect of such a parameter can be readily seen by considering the physics behind the acceleration process, but since an accelerator is a complex machine consisting of many different devices, the effect might be not as obvious. This can lead for example to the phenomenon of jitter compensation, when certain parameters influence each other. A more detailed

theoretical discussion of the sensitivity of the bunch time of flight towards small RF phase changes will show how the gun/buncher setup that has been chosen for REGAE can lead to such effects (see section 3.2).

The ideal starting point for the identification of important machine parameters would be an analytical model of the form

$$P_i = F_{m,i}(\mathbf{a}), \tag{3.1}$$

where P_i is the beam parameter of interest and $\mathbf{a}$ is a set (vector) of machine input parameters. $F_{m,i}$ would be the general and analytical formula corresponding to (in our case) the REGAE accelerator. Such an approach is in general not feasible, because of the sheer amount of input parameters and the complexity of the system. We therefore have to conclude that in most cases $F_{m,i}$ is unknown and has to be considered as a *black box*. So how can we approach a system like this? In practice all the important beam parameters can be determined via numerical simulation (beam tracking). The main tool for this is ASTRA. In the following sections all simulations will be carried out using ASTRA. We now have access to the most important beam parameters via ASTRA, but still need tools to determine the sensitivity of certain beam parameters towards the input parameters. This way we could identify the most important of them. The next section will give an introduction to the most commonly used methods for sensitivity analysis, which itself can be defined as "the study of how uncertainty in the output of a model (numerical or otherwise) can be appointed to different sources of uncertainty in the model input" (Saltelli et al., 2004).

3.1.1 Theoretical Background

The sensitivity analysis of a given system or mathematical model can be conducted in several ways ([33]). Let $f(\mathbf{a})$ be a mathematical model with M input parameters and $\mathbf{a}$ an M-dimensional vector, which contains those parameters. This model has just one output. For simplicity, let us assume the model to be defined as

$$f(\mathbf{a}) = \sum_{i=0}^{M} c_i a_i. \tag{3.2}$$

Each input parameter is assumed to be normally distributed with an uncertainty σ_{a_i} and the c_i are arbitrary constants. One typical approach to specify the "sensitivity" of such an analytical model towards the input parameters, is to just take the partial derivatives. The measure of sensitivity would hence be defined by

$$S_{a_i} = \frac{\partial f(\mathbf{a})}{\partial a_i}. \tag{3.3}$$

In our simple case we would get $S_{a_i} = c_i$, or in other words: The most influential parameter is the one with the largest slope (for example for the bunch time of flight: $S_{t_{\mathrm{TOF}}} = 1\,\mathrm{ps}/\mathrm{deg}_{\mathrm{RF}}$). There are several problems here:

(1) This sensitivity measure is only globally valid for linear models, or if we assume small changes and hence the σ_{a_i} to be sufficiently small.

(2) This method only works, if the input parameters are independent.

(3) The uncertainty of the individual input parameters is ignored.

The first problem is very straight forward. If our model includes nonlinear terms in a_i, it is necessary to assume small changes in a_i in order to be able give a global and constant S_{a_i}. Doing so will of course fix the sensitivity measure to one point in the configuration space of the a_i. The most important downside of this simple method is the fact that the uncertainty of the input is ignored. Assuming $c_i = c_0 = \text{const}$ for all i, all partial derivatives and hence all S_{a_i} would evaluate to the same value c_0, meaning that the system is equally sensitive to all input parameters, or: "all input parameters have the same effect on the output". This is clearly not true if $\sigma_{a_i} \neq \sigma_{a_j}$ for $i \neq j$ and $i, j \in [0, N]$. The input parameter with the highest uncertainty will have the highest impact on the result, which is clearly overlooked using simple partial derivatives.

A possible work around for problem (3) is using so called *sigma normalized derivatives*. Sigma normalized derivatives take both the individual uncertainty of the a_i and the overall uncertainty of the output into account. The sensitivity measure now looks like

$$\tilde{S}_{a_i} = \tilde{\sigma}_i \cdot \frac{\partial f(\mathbf{a})}{\partial a_i}, \tag{3.4}$$

where $\tilde{\sigma}_i = \sigma_{a_i}/\sigma_{f(\mathbf{a})}$. It can be shown that for a linear additive model like equation 3.2 the sum of the $S_{a_i}^2$ is equal to one, which qualifies the sigma normalized derivatives as a useful sensitivity measure [33]. The derivation can be done the following way. Starting with

$$\sum_{i=0}^{M} \tilde{S}_{a_i}^2 = \sum_{i=0}^{M} \tilde{\sigma}_i^2 \left(\frac{\partial f(\mathbf{a})}{\partial a_i} \right)^2 = \frac{1}{\sigma_{f(\mathbf{a})}^2} \cdot \sum_{i=0}^{M} \sigma_{a_i}^2 \left(\frac{\partial f(\mathbf{a})}{\partial a_i} \right)^2, \tag{3.5}$$

it can be written for a model like equation 3.2:

$$\sum_{i=0}^{M} \tilde{S}_{a_i}^2 = \frac{1}{\sigma_{f(\mathbf{a})}^2} \cdot \sum_{i=0}^{M} \sigma_{a_i}^2 c_i^2 \stackrel{!}{=} 1. \tag{3.6}$$

Therefore

$$\sigma^2_{f(\mathbf{a})} \stackrel{!}{=} \sum_{i=0}^{M} \sigma^2_{a_i} c_i^2. \tag{3.7}$$

Using the usual definition for the variance we get

$$\sigma^2_{f(\mathbf{a})} = \frac{1}{N} \cdot \sum_{j=0}^{N} (f(\mathbf{a}_j) - \bar{f})^2. \tag{3.8}$$

Without loss of generality M can be set to $M = 2$. Therefore it can be calculated for N samples that

$$\begin{aligned}
\sigma^2_{f(\mathbf{a})} &= \frac{1}{N} \cdot \sum_{j=0}^{N} (c_1 a_{1,j} + c_2 a_{2,j} - \bar{f})^2 \\
&= \frac{1}{N} \cdot \sum_{j=0}^{N} (c_1 a_{1,j} + c_2 a_{2,j} - \bar{f}_1 - \bar{f}_2)^2 \\
&= \frac{1}{N} \cdot \sum_{j=0}^{N} (c_1 a_{1,j} - \bar{f}_1)^2 + (c_2 a_{2,j} - \bar{f}_2)^2 \\
&\qquad + 2(\bar{f}_1 \bar{f}_2 + c_1 a_{1,j} c_2 a_{2,j} - c_1 a_{1,j} \bar{f}_2 - c_2 a_{2,j} \bar{f}_1) \\
&= \frac{1}{N} \cdot \sum_{j=0}^{N} (c_1 a_{1,j} - \bar{f}_1)^2 + (c_2 a_{2,j} - \bar{f}_2)^2 + 2(c_1 a_{1,j} - \bar{f}_1)(c_2 a_{2,j} - \bar{f}_2).
\end{aligned} \tag{3.9}$$

Using the definition for the covariance $\mathrm{Cov}(x, y) = \langle (x - \bar{x})(y - \bar{y}) \rangle$ we arrive at

$$\sigma^2_{f(\mathbf{a})} = \sigma^2_{a_1} c_1^2 + \sigma^2_{a_2} c_2^2 + 2 c_1 c_2 \cdot \mathrm{Cov}(a_1, a_2). \tag{3.10}$$

This result can be generalized for arbitrary M and corresponds to equation 3.7 if all covariance terms vanish, which is the case for uncorrelated a_i. The last assumption of course implies an important constraint on the usefulness of this sensitivity measure. Only additive, linear models with uncorrelated input parameters lead to sum of the squares that is equal to one.

As it has been stated several times, the behavior of the REGAE beam parameters cannot in general be described by a simple analytical model. Despite this circumstance it is possible to find so called *model independent* stability measures. This thesis will focus on two kinds:

(1) Scatter plots and averaged partial variances

(2) Variance based sensitivity indices.

The first method is the method of scatter plots. Scatter plots can be obtained via Monte Carlo simulations. A Monte Carlo simulation consists of a set of N simulation runs of a given model, where the input vector $\mathbf{a}$ is generated pseudo-randomly for each run. This way also numerical models like the ASTRA tracking code can be used. In order to explain the method, the simple model from equation 3.2 with $M = 4$ will be used. A sample simulation can be seen in figure 3.1. The scatter plots shown there immediately visualize the sensitivity of the model towards the a_i. A first graphical analysis can be the division of the scatter plots' coordinate systems into the four usual quadrants I, II, III and IV. Then the shape of the distribution can be characterized by

$$s_{a_i} = (\Sigma_{\mathrm{I}} + \Sigma_{\mathrm{III}}) - (\Sigma_{\mathrm{II}} + \Sigma_{\mathrm{IV}}), \tag{3.11}$$

where Σ_j denotes the sum of data points in the quadrant j. So for a radially distributed set of data points s would be approximately zero, the distribution would have no significant shape. It has to be noted that this is a very vague measure, as it only measures the overall shape of the distribution. A somewhat more robust tool is the so called *Pearson's* ρ, or in the case of empirical data the *correlation coefficient*. The latter can be calculated using

$$r_{x,y} = \frac{\sum_{i=0}^{N}(x_i - \bar{x})(y_i - \bar{y})}{\sqrt{\sum_{i=0}^{N}(x_i - \bar{x})^2 \cdot \sum_{i=0}^{N}(y_i - \bar{y})^2}}. \tag{3.12}$$

In our case $x = f(\mathbf{a})$ and $y = a_i$. The correlation coefficient r is a measure of the linearity of the functional dependence $x(y)$ and $r_{x,y} \in [-1, 1]$. It can also be used to calculate the fraction of the variance of x that can be attributed to its linear connection to y, which is called R^2 or the *coefficient of determination* and is just the square of $r_{x,y}$. Since $r_{x,y} \in [-1, 1]$, $R^2 \in [0, 1]$. This coefficient is often also used as a figure of merit for fit models. These two measures are good tools for a quick analysis of scatter plots, but still do not fulfill the requirement of model freeness. We ultimately want to determine how much of the variance of the output parameter can be attributed to the variance of a specific input parameter for all kinds of models (this is also the definition of sensitivity used in this thesis). By doing so, the most important parameters can be filtered out. A popular method ([33]) is the analysis of scatter plots by cutting them into slices along the abscissa and calculating the characteristics of the slice distributions. Saltelli et al. suggest the variance of the mean of the output parameter along the slice as the quantile of choice. In the limit of infinite slices this corresponds to the so called *first order effect* of a_i on $f(\mathbf{a})$. These averaged partial variances have the important advantage over sigma normalized derivatives for example that one explores the

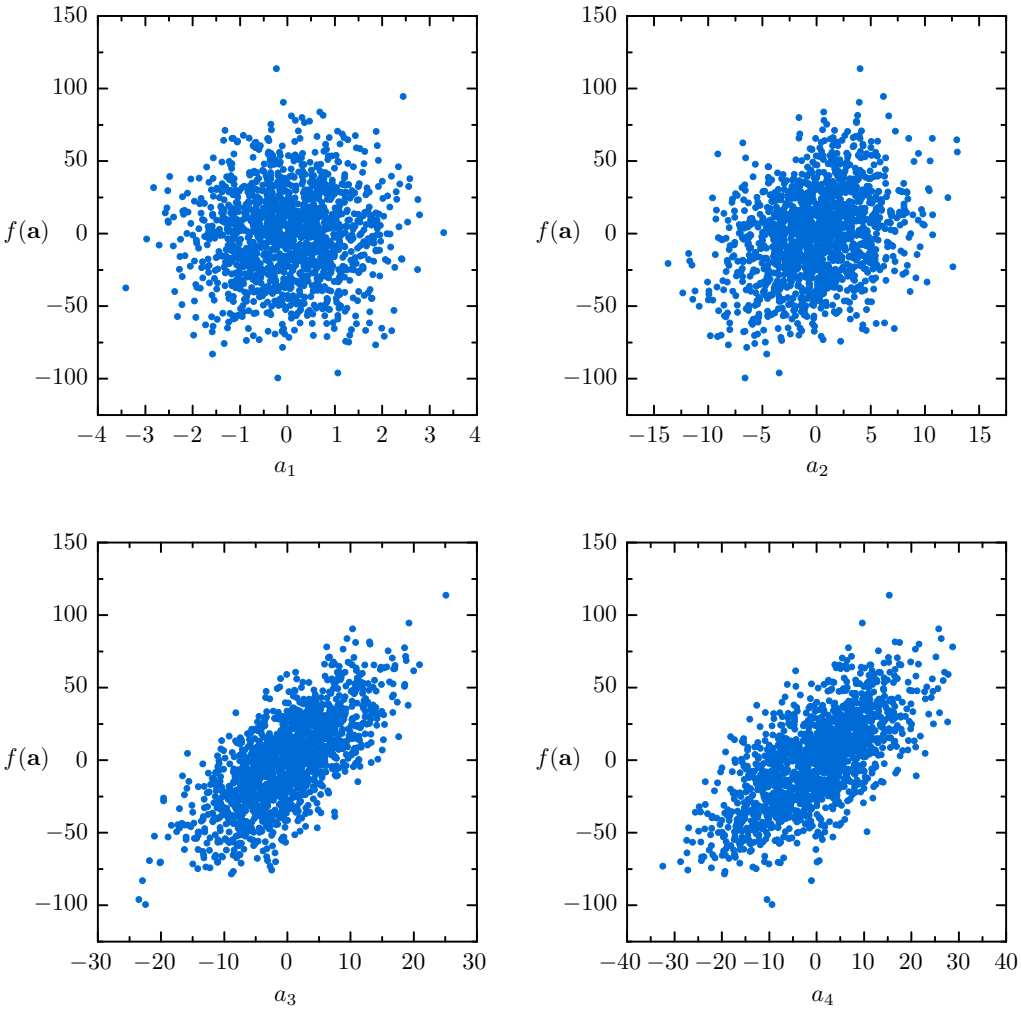

Figure 3.1: Scatter plots for a linear additive model like equation 3.2 with $M = 4$ and 1500 runs. The c_i have all been chosen to be equal to 2 and the input parameters a_i are normally distributed around 0 with standard deviations $\sigma_{a_1} < \sigma_{a_2} < \sigma_{a_3} < \sigma_{a_4}$. Please note the different scaling of the axes.

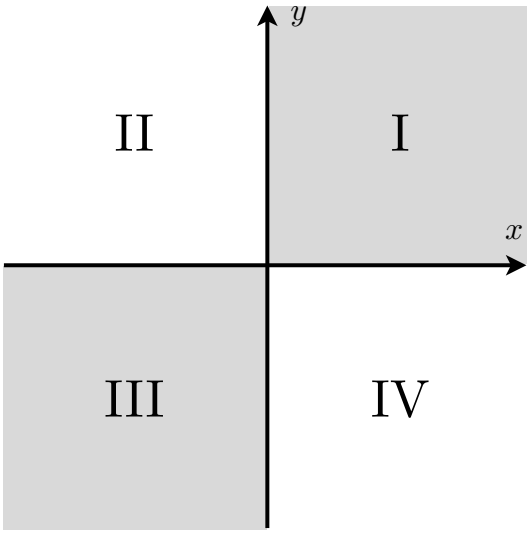

Figure 3.2: The four quadrants of a Cartesian coordinate system.

whole configuration space instead of focusing on one fixed a_i. We are now able to condense scatter plots into one single number, the first order effect, which is in its normalized form also called the *first order sensitivity index* and defined by ([33])

$$S_i = \frac{\mathrm{V}_{a_i}(\mathrm{E}_{\sim a_i}(f(\mathbf{a})|a_i))}{\mathrm{V}(f(\mathbf{a}))}, \tag{3.13}$$

where in the literature the notation V is mostly used for the variance, E for the expectation value and $\sim a_i$ for "all but a_i". The numerator can be read as "the variance of the expectation value of $f(\mathbf{a})$ for fixed (known) a_i" and is hence a conditional variance. This measure is now indeed model free and $S_i \in [0, 1]$, but can only describe the first order effect and therefore neglects all interdependencies between the input parameters. This implies that for a model, where the interdependencies between input parameters affect the output

$$S_T = \sum_{i=1}^{M} S_i < 1. \tag{3.14}$$

Figure 3.3 shows the evolution of the mean of the output distribution along one slice for 100 uniformly distributed slices of the scatter plots shown in 3.1. The difference in variance can be seen. From these data the first order sensitivity indices have been computed for different numbers of slices in order to show the fact that one has to take the limit of infinite slices in order to approach the real values. See figure 3.4 for the results of this calculation. Since the underlying model

is the simple model from equation 3.2, the total first order effect must converge to unity, which it does for a large number of slices. An important result from this numerical experiment is the fact that for low slice numbers the difference between the individual sensitivity indices is way too low, leading to a wrong judgment of the sensitivities.

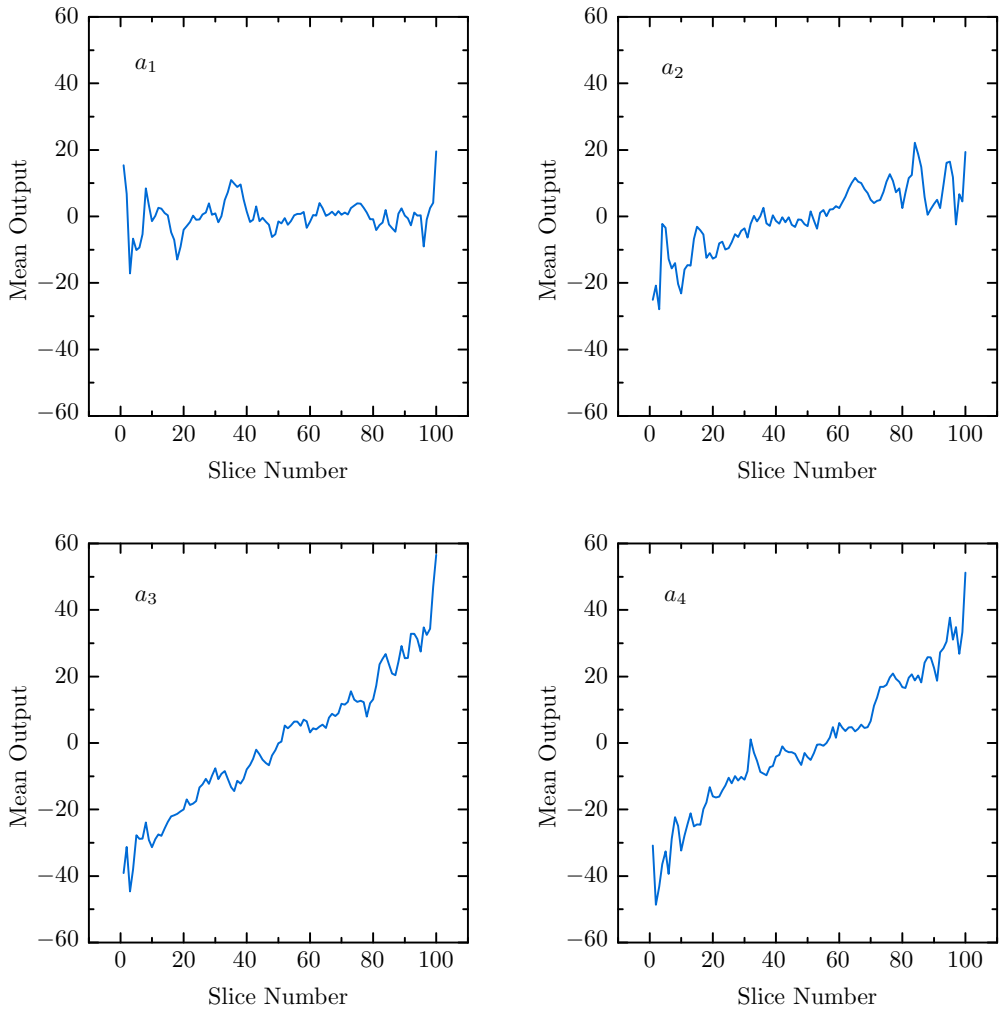

Figure 3.3: Evolution of the mean output of 100 uniformly distributed slices for the scatter plots shown in 3.1.

Having described a method to interpret Monte Carlo simulations of arbitrary form (model free approach) using scatter plots and averaged partial variances, the

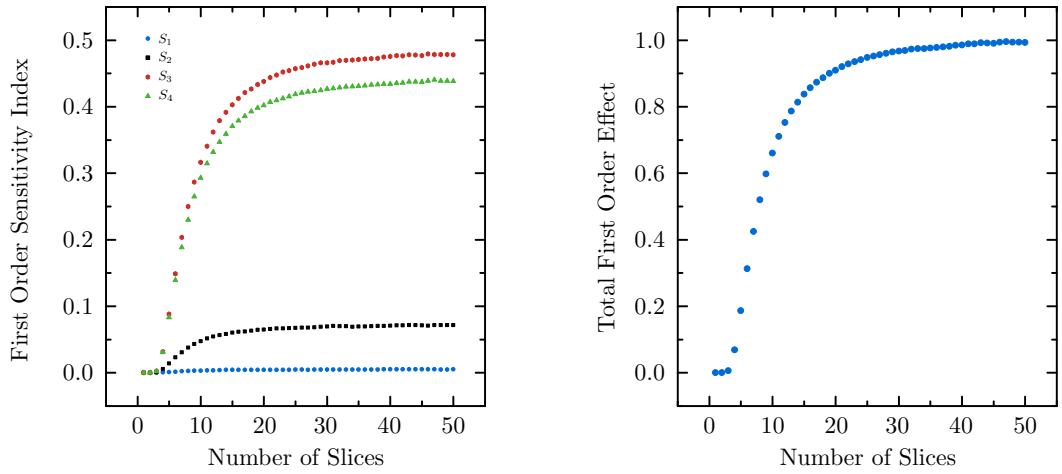

Figure 3.4: First order sensitivity indices and the total first order effect for the scatter plots shown in figure 3.1. The S_i have been calculated using equation 3.13 and the total effect is defined by the sum of the individual S_i.

focus will now be put on a well established variance based method for calculating sensitivity indices like the one presented in equation 3.13 for an arbitrary model with uncorrelated input parameters. It was first proposed by Sobol in 1990 ([34, 35]) and has since then been extended by Saltelli et al. and others ([1, 36]).

The first step is the setup of the Monte Carlo experiment by defining two input matrices of the following form:

$$\hat{\mathbf{M}}_1 = \begin{pmatrix} a_1^{(1)} & a_2^{(1)} & \dots & a_{M-1}^{(1)} & a_M^{(1)} \\ a_1^{(2)} & a_2^{(2)} & \dots & a_{M-1}^{(2)} & a_M^{(2)} \\ \vdots & \vdots & \dots & \vdots & \vdots \\ a_1^{(N-1)} & a_2^{(N-1)} & \dots & a_{M-1}^{(N-1)} & a_M^{(N-1)} \\ a_1^{(N)} & a_2^{(N)} & \dots & a_{M-1}^{(N)} & a_M^{(N)} \end{pmatrix}, \tag{3.15}$$

$$\hat{\mathbf{M}}_2 = \begin{pmatrix} \tilde{a}_1^{(1)} & \tilde{a}_2^{(1)} & \dots & \tilde{a}_{M-1}^{(1)} & \tilde{a}_M^{(1)} \\ \tilde{a}_1^{(2)} & \tilde{a}_2^{(2)} & \dots & \tilde{a}_{M-1}^{(2)} & \tilde{a}_M^{(2)} \\ \vdots & \vdots & \dots & \vdots & \vdots \\ \tilde{a}_1^{(N-1)} & \tilde{a}_2^{(N-1)} & \dots & \tilde{a}_{M-1}^{(N-1)} & \tilde{a}_M^{(N-1)} \\ \tilde{a}_1^{(N)} & \tilde{a}_2^{(N)} & \dots & \tilde{a}_{M-1}^{(N)} & \tilde{a}_M^{(N)} \end{pmatrix}, \tag{3.16}$$

where each of these matrices is of dimension $M \times N$. M is the number of input parameters and N is the number of Monte Carlo runs. We now have two inde-

pendent (denoted by the tilde characters in $\hat{\mathbf{M}}_2$) and randomly generated sets of input parameters. The next step is to setup the M so called *re-sampled matrices* C_j, which are defined by

$$\hat{\mathbf{C}}_j = \begin{pmatrix} \tilde{a}_1^{(1)} & \tilde{a}_2^{(1)} & \dots & a_j^{(1)} & \dots & \tilde{a}_{M-1}^{(1)} & \tilde{a}_M^{(1)} \\ \tilde{a}_1^{(2)} & \tilde{a}_2^{(2)} & \dots & a_j^{(2)} & \dots & \tilde{a}_{M-1}^{(2)} & \tilde{a}_M^{(2)} \\ \vdots & \vdots & \dots & \vdots & \dots & \vdots & \vdots \\ \tilde{a}_1^{(N-1)} & \tilde{a}_2^{(N-1)} & \dots & a_j^{(N-1)} & \dots & \tilde{a}_{M-1}^{(N-1)} & \tilde{a}_M^{(N-1)} \\ \tilde{a}_1^{(N)} & \tilde{a}_2^{(N)} & \dots & a_j^{(N)} & \dots & \tilde{a}_{M-1}^{(N)} & \tilde{a}_M^{(N)} \end{pmatrix}, \tag{3.17}$$

i. e. a matrix $\hat{\mathbf{M}}_1$, where all but the j-th column is re-sampled with values from $\hat{\mathbf{M}}_2$. Now the Monte Carlo experiment is performed for all of the $M+2$ matrices, resulting in $N(M+2)$ runs. The results are the output vectors

$$\begin{aligned} \mathbf{f}_0 &= f(\hat{\mathbf{M}}_2) \\ \mathbf{f}_j &= f(\hat{\mathbf{C}}_j) \\ \mathbf{f}_{1,2,\dots,M} &= f(\hat{\mathbf{M}}_1). \end{aligned} \tag{3.18}$$

Using these output vectors, it is now possible to calculate sensitivity indices as follows.

Let us first recall equation 3.13. In order to calculate the numerator one has to start with the variance of $f(\mathbf{a})$ for <u>one</u> known $a_i = \tilde{a}_i$. Using the standard definition of the variance ($\sigma_x^2 = \langle x^2 \rangle - \langle x \rangle^2$) we then get

$$\mathrm{V}(f(\mathbf{a})|a_i = \tilde{a}_i) = \langle f(\mathbf{a}_{a_i=\tilde{a}_i})^2 \rangle - \langle f(\mathbf{a}_{a_i=\tilde{a}_i}) \rangle^2 \tag{3.19}$$

Since we try to find a model free sensitivity measure, it is now necessary to integrate over all a_i, or in other words calculate the expectation value with respect to a_i, given by

$$\begin{aligned} \mathrm{E}(\mathrm{V}(f(\mathbf{a})|a_i)) &= \mathrm{E}(\langle f(\mathbf{a}_{a_i=\tilde{a}_i})^2 \rangle) - \mathrm{E}(\langle f(\mathbf{a}_{a_i=\tilde{a}_i}) \rangle^2) \\ &= \langle f(\mathbf{a})^2 \rangle - \mathrm{E}(\langle f(\mathbf{a}_{a_i=\tilde{a}_i}) \rangle^2), \end{aligned} \tag{3.20}$$

where both notations for the expectation value are used for better readability. The numerator in equation 3.13 can also be understood as the difference of the total output variance and the expectation value of the output variance for known a_i. Hence

$$\mathrm{V}_{a_i}(\mathrm{E}_{\sim a_i}(f(\mathbf{a})|a_i)) \equiv \mathrm{V}(f(\mathbf{a})) - \mathrm{E}(\mathrm{V}(f(\mathbf{a})|a_i)), \tag{3.21}$$

where the second term is just equation 3.20. Inserting 3.20 into 3.21 we arrive at

$$\begin{aligned} \mathrm{V}_{a_i}(\mathrm{E}_{\sim a_i}(f(\mathbf{a})|a_i)) &= \langle f(\mathbf{a})^2 \rangle - \langle f(\mathbf{a}) \rangle^2 - \langle f(\mathbf{a})^2 \rangle + \mathrm{E}(\langle f(\mathbf{a}_{a_i=\tilde{a}_i}) \rangle^2) \\ &= \mathrm{E}(\langle f(\mathbf{a}_{a_i=\tilde{a}_i}) \rangle^2) - \langle f(\mathbf{a}) \rangle^2. \end{aligned} \tag{3.22}$$

Adopting the notation from the original paper by Saltelli et al. ([1]) this conditional variance can be written as

$$V^C_{i_1,i_2\ldots i_M} = U_{i_1,i_2\ldots i_M} - \mathrm{E}^2(f(\mathbf{a})) \tag{3.23}$$

Note that before only first order effects had been discussed, which would lead to a V^C with only one index. Higher order effects are now described for example by $V^C_{1,4} = V_1 + V_4 + V_{1,4}$, which therefore includes all the first order terms plus the interdependency term. It has been shown in [37] that the U_j can be estimated by

$$U_j = \frac{\mathbf{f}_{1,2,\ldots,M} \cdot \mathbf{f}_j}{M-1}, \tag{3.24}$$

where $\langle\cdot\rangle$ denotes the scalar product between two vectors. Using a Monte Carlo experiment carried out based on the input matrices $\hat{\mathbf{M}}_1$, $\hat{\mathbf{M}}_2$ and $\hat{\mathbf{C}}_j$, it is now easy to calculate S_j. In addition to that, one also can calculate the so called *total effect indices* S^T_j which contain the first order effects, as well as all interdependencies of the a_j. They are defined analogously to the S_j as

$$S^T_j = \frac{\mathrm{V}(f(\mathbf{a})) - \mathrm{V}(\mathrm{E}(f(\mathbf{a}_{a_{-j}})))}{\mathrm{V}(f(\mathbf{a}))} = 1 - \frac{U_{-j} - \mathrm{E}^2(f(\mathbf{a})}{\mathrm{V}(f(\mathbf{a})}, \tag{3.25}$$

where $U_{-j} = \mathbf{f}_0 \cdot \mathbf{f}_j/(M-1)$. The nominator in equation 3.25 can be verbalized as "the difference between the total variance and the contributions to the variance from a_i, which do not depend on a_i". Table 3.1 shows all terms that can estimated using this method for a model with $M = 5$.

Table 3.1: Terms that can be estimated given the corresponding vectors of model evaluation, $M = 5$ (Taken from [1]).

	$\mathbf{f}_0$	$\mathbf{f}_1$	$\mathbf{f}_2$	$\mathbf{f}_3$	$\mathbf{f}_4$	$\mathbf{f}_5$	$\mathbf{f}_{2345}$	$\mathbf{f}_{1345}$	$\mathbf{f}_{1245}$	$\mathbf{f}_{1235}$	$\mathbf{f}_{1234}$	$\mathbf{f}_{12345}$
$\mathbf{f}_0$	$\hat{V}(y)$											
$\mathbf{f}_1$	$\hat{S}^T_1$	$\hat{V}(y)$										
$\mathbf{f}_2$	$\hat{S}^T_2$	$\hat{V}^C_{-12}$	$\hat{V}(y)$									
$\mathbf{f}_3$	$\hat{S}^T_3$	$\hat{V}^C_{-13}$	$\hat{V}^C_{-23}$	$\hat{V}(y)$								
$\mathbf{f}_4$	$\hat{S}^T_4$	$\hat{V}^C_{-14}$	$\hat{V}^C_{-24}$	$\hat{V}^C_{-34}$	$\hat{V}(y)$							
$\mathbf{f}_5$	$\hat{S}^T_5$	$\hat{V}^C_{-15}$	$\hat{V}^C_{-25}$	$\hat{V}^C_{-35}$	$\hat{V}^C_{-45}$	$\hat{V}(y)$						
$\mathbf{f}_{2345}$	$\hat{S}_1$	$\hat{E}^2(y)$	$\hat{V}^C_{12}$	$\hat{V}^C_{13}$	$\hat{V}^C_{14}$	$\hat{V}^C_{15}(y)$	$\hat{V}(y)$					
$\mathbf{f}_{1345}$	$\hat{S}_2$	$\hat{V}^C_{12}$	$\hat{E}^2(y)$	$\hat{V}^C_{23}$	$\hat{V}^C_{24}$	$\hat{V}^C_{25}(y)$	$\hat{V}^C_{-12}(y)$	$\hat{V}(y)$				
$\mathbf{f}_{1245}$	$\hat{S}_3$	$\hat{V}^C_{13}$	$\hat{V}^C_{23}$	$\hat{E}^2(y)$	$\hat{V}^C_{34}$	$\hat{V}^C_{35}(y)$	$\hat{V}^C_{-13}(y)$	$\hat{V}^C_{-23}$	$\hat{V}(y)$			
$\mathbf{f}_{1235}$	$\hat{S}_4$	$\hat{V}^C_{14}$	$\hat{V}^C_{24}$	$\hat{V}^C_{34}$	$\hat{E}^2(y)$	$\hat{V}^C_{45}$	$\hat{V}^C_{-14}(y)$	$\hat{V}^C_{-24}(y)$	$\hat{V}^C_{-34}$	$\hat{V}(y)$		
$\mathbf{f}_{1234}$	$\hat{S}_5$	$\hat{V}^C_{15}$	$\hat{V}^C_{25}$	$\hat{V}^C_{35}$	$\hat{V}^C_{45}$	$\hat{E}^2(y)$	$\hat{V}^C_{-15}$	$\hat{V}^C_{-25}(y)$	$\hat{V}^C_{-35}(y)$	$\hat{V}^C_{-45}$	$\hat{V}(y)$	
$\mathbf{f}_{12345}$	$\hat{E}^2(y)$	$\hat{S}_1$	$\hat{S}_2$	$\hat{S}_3$	$\hat{S}_4$	$\hat{S}_5$	$\hat{S}^T_1$	$\hat{S}^T_2$	$\hat{S}^T_3$	$\hat{S}^T_4$	$\hat{S}^T_5$	$\hat{V}(y)$

The advantage of this method compared to the scatter plot method is the fact that also higher order effects can be detected. On the other hand many evaluations

are necessary, which will be visualized now using the simple linear model 3.2 with $M = 3$ and $c_1 = c_2 = c_3 = 1$. In order to evaluate how many model evaluations are necessary to reach an accurate estimate for the S_j, a Monte Carlo experiment has been performed, where the sensitivity analysis is performed 100 times for different numbers of model evaluations. After that, the mean value and standard deviation for the S_j has been calculated for each number of evaluations. Figure 3.5 shows the results for S_3. It can be seen that in order to achieve a reasonable accuracy of $>99\,\%$, an amount of model runs of at least 400000 is necessary.

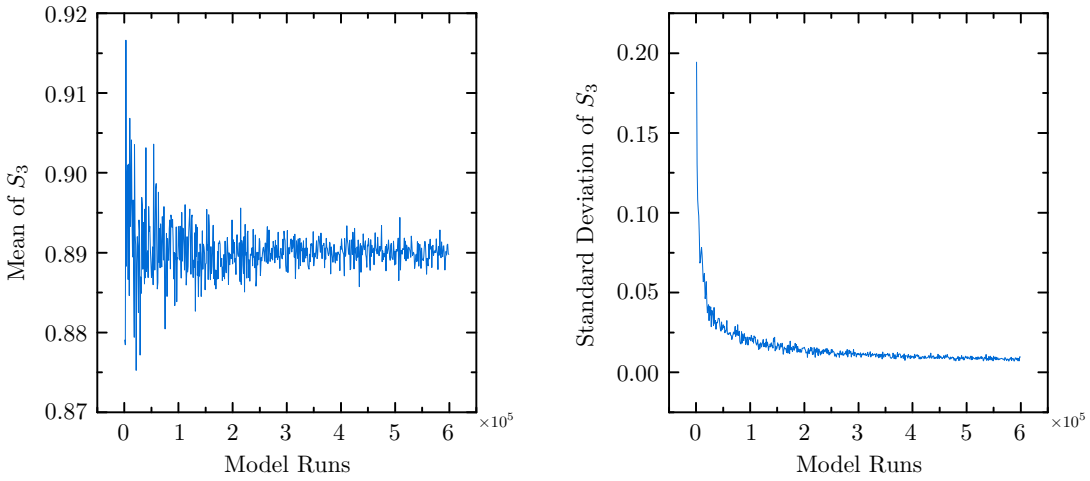

Figure 3.5: Mean value and standard deviation of S_3 calculated for different amounts of model evaluations. For every data point the sensitivity analysis has been performed 100 times.

3.1.2 Sensitivity Analysis based on ASTRA Simulations

In this section, two of the sensitivity analysis methods that have been discussed above will be applied to several parameters at REGAE. As it has already been stated, the method by Saltelli et al. — even though it is one of the most efficient ([33]) — requires a large amount of simulation runs. If one wants to perform a sensitivity analysis for REGAE, the only possibility is to use the particle tracking code ASTRA. Therefore in order to be able to generate enough statistics, one needs to perform an immense amount of ASTRA simulations ($N(M + 2)$). Since REGAE is a relatively small machine and therefore the number of input parameters is manageable, it can be used to also evaluate the feasibility of the variance based

sensitivity analysis methods that have been presented, in the context of accelerator physics. In this thesis two different sensitivity analyses will be performed:

(a) Scatter plot analysis based on ASTRA simulations performed using electron bunches for several machine parameters

(b) Saltelli type analysis based on single particle ASTRA simulations.

The first one will be focused on beam parameters like transverse emittance, energy spread and bunch length. Here also the effects due to the solenoid lenses will be studied. The second — Saltelli type — analysis will then be focused on the mean beam energy, which leads to changes in the time of flight of the bunches. To this end the cavity amplitudes and phases will be used as input parameters.

Using ASTRA for Sensitivity Studies

A Saltelli type sensitivity analysis requires an easy mechanism to perform the model evaluations in an automated way. ASTRA simulations always start with a so called *input deck*, which contains all the required simulation parameters and the machine layout. This implies that for each simulation run a unique input deck is required. In other words, the input matrices $\hat{\mathbf{M}}_1, \hat{\mathbf{M}}_2$ and $\hat{\mathbf{C}}_j$ need to be translated into valid ASTRA input decks. To this end a MATLAB tool has been written, which performs the following five steps:

(1) Random generation of the input matrices $\hat{\mathbf{M}}_1, \hat{\mathbf{M}}_2$

(2) Calculation of the re-sampled matrices $\hat{\mathbf{C}}_j$

(3) Generation of the $N(M+2)$ ASTRA input decks, based on the input matrices

(4) Consecutive execution of the ASTRA code for all $N(M+2)$ input decks

(5) Calculation of sensitivity measures based on the ASTRA output and using Saltelli's method.

It has been shown above that in order to improve the accuracy (reduce the standard deviation) of the sensitivity indices, a large number of model runs is necessary. Therefore the sensitivity analysis tool has been setup in a away that it can run on multiple processors. The following simulations have been performed using a total of 32 cores (Intel Xeon and Intel Core i5), which resulted in a simulation time of 7 days.

Scatter Plot Analysis

For the scatter plot analysis 32000 ASTRA simulations from the cathode to the target screen at $z = 5.5\,\mathrm{m}$ have been performed. As output parameters horizontal RMS emittance, energy spread, bunch length and horizontal RMS spot size on the target were chosen. For the input both cavity phases, as well as the magnetic fields of the solenoid lenses have been chosen. Variation of the input has been configured to be compliant with the design stability goals of 0.01 deg phase stability for both cavities, while the solenoid field stability has been adjusted to a stability obtained from the measurements that will be discussed in section 3.3.1. Using the slice analysis method discussed above, the first order sensitivity indices shown in table 3.2 have been estimated. For the variance of the horizontal RMS emittance the gun phase stability is the most important factor. This makes sense, because this is where the beam emittance is first defined through the acceleration process. Interestingly also the first solenoid has a significant effect on the variance of the RMS emittance. Its sensitivity index is approximately half the gun phase sensitivity. This circumstance can be explained by non linear forces that act on the beam when it passes the first solenoid. In fact this is also true for the other two solenoids, but the beam size right after the gun cavity is much larger, since it is not focused yet (except for the focusing effect of the gun itself). This leads to a larger fraction of the bunch being exposed to non-linearities of the solenoid field.

The bunch length variance is mainly dependent on the cavity phases. It turns out that the gun cavity's phase is the most influential parameter. This can be explained by considering that phase slippage effects inside the gun cavity — which are different depending on the injection phase — can affect the bunch length. In addition to that, the energy spread also depends on the injection phase, which is an important factor in the velocity bunching scheme.

According to the analysis, the variance of the horizontal RMS spot size on target is mostly dependent on the last solenoid's variance, which is the last element in

Table 3.2: First order sensitivity indices for the slice based scatter plot analysis using ASTRA simulations. ($S_1 \rightarrow$ gun phase, $S_2 \rightarrow$ buncher phase, $S_3 \rightarrow$ solenoid 1 field, $S_4 \rightarrow$ solenoid 2_3 field, $S_5 \rightarrow$ solenoid 4_5 field)

	S_1	S_2	S_3	S_4	S_5	ΣS_i
Horizontal RMS emittance	0.621	0.009	0.326	0.043	0.008	1.006
Bunch length	0.553	0.425	0.01	0.006	0.005	0.999
Energy spread	0.745	0.237	0.011	0.005	0.005	1.003
Horizontal RMS spot size	0.024	0.024	0.022	0.176	0.713	0.959

front of the target. It can also be seen that the focusing effect of the cavities cannot be neglected. The effect on the spot size variance is on the same order as the effect of the first solenoid.

Except for the case of the spot size, interdependencies of the input parameters do not seem to have an effect on the variances. It is important to note that a total sensitivity value slightly greater than one can occur due to statistical inaccuracies. An increase in the number of slices leads to a slight oscillation around the asymptotic value. The stability of the REGAE magnets will be discussed in detail in section 3.3.1.

Saltelli Type Analysis

For the second sensitivity analysis 600000 ASTRA simulations have been performed using the sensitivity tool. Since this analysis is limited to single particle simulations, only one output parameter will be evaluated, the beam energy. As input parameters the gun amplitude and phase, as well as the buncher amplitude and phase have been studied. Table 3.3 shows the results of the analysis. There are several things that can be extracted from the sensitivity indices here. First of all it can be seen that the buncher phase is the most important parameter of the four. This makes sense, because the buncher is operated off-crest. It can also be seen that the phases show significantly larger sensitivity compared to the amplitudes. The third observation is the fact that the sum of the S_i is smaller than one. Recalling the theory of the sensitivity indices, this leads to the conclusion that higher order effects, or in other words the combined effect of the individual parameters also influence the overall beam energy variance. This can also be concluded from the total effect indices, which are in all cases greater than the first order effects.

The sensitivity analysis for the beam energy has revealed how the individual variances of the cavity parameters affect the beam energy. In the next section the dependence of the electron bunch time of flight stability on the RF phase stability will be discussed looking at the underlying physics in an analytical way.

Table 3.3: First order, as well as total sensitivity indices for the sensitivity analysis using ASTRA for the mean beam energy. The values have been obtained using Saltelli's method. ($S_1 \rightarrow$ gun amplitude, $S_2 \rightarrow$ gun phase, $S_3 \rightarrow$ buncher amplitude, $S_4 \rightarrow$ buncher phase)

	S_1	S_2	S_3	S_4	ΣS_i
1st order effect	0.004	0.069	0.019	0.881	0.973
Total effect	0.028	0.105	0.037	0.927	1.097

Concluding Remarks

In this section variance based sensitivity analysis methods have been applied to several parameters of the REGAE machine. Even though the results of both analyses provide insight into the importance and interplay of different input parameters, it has to be admitted that the sheer amount of required model runs limits these techniques to small machines like REGAE. A complex machine like FLASH (**F**ree electron **LAS**er **H**amburg) for example, has so many input parameters that in order to analyze them, the number of model runs and the resulting computing time would not be feasible.

3.2 Dependence of Bunch Time of Flight Stability on RF Stability

In the preceding chapters the dependence of several beam parameters on the variance of input parameters like the gun phase and amplitude have been discussed on the basis of statistical methods. As it has been stated in the introductory chapter, the stability of the bunch time of flight is crucial for the experiments, which are going to be conducted using the REGAE machine. The first part of this section will give the relevant physical background for understanding the dependence of time of flight on small RF phase changes. In the second part actual measurements of the phase stability at REGAE will be presented.

3.2.1 Physical Background

The phase for which the electron and the field reach a fixed phase relationship inside the accelerator cavity is the so called synchronous phase ϕ_{sync}, which has been derived elsewhere ([12]) to be:

$$\phi_{\text{sync}} = \phi_0 + \frac{1}{2\alpha} \cdot \csc\left(\phi_0 + \frac{1}{2\alpha}\right) \tag{3.26}$$

where $\phi_0 + 1/2\alpha \equiv \phi_{\text{eff}}$ is the effective phase that compensates the phase slippage effects right after the injection process ([12]) and α is the normalized vector potential of the field, which can be written in terms of the maximum accelerating field E_0 as

$$\alpha = \frac{eE_0}{2m_e c^2 k}, \tag{3.27}$$

where e and m_e are the charge and the mass of the electron and $k = 2\pi/\lambda$. For $\alpha \geq 1$ relativistic effects in the particle dynamics have to be taken into account.

For an S-band cavity — like the cavities that are used at REGAE — operating at 110 MV/m, the normalized vector potential is approximately equal to 1.7. When the electron has reached ϕ_{sync}, its velocity is $v \approx c$, where c is the speed of light in vacuum. This implies that an electron which could be injected at $\phi_0 = \phi_{\text{sync}}$ must have the shortest time of flight, which in turn means that $\phi_{\text{sync}} - \phi_0$ is a measure for the time of flight of a particle. The phase of the electron can be expressed as:

$$\phi = \omega t - kz + \phi_0 = \beta ckt - kz + \phi_0, \tag{3.28}$$

where $k = 2\pi/\lambda$ and $\beta = v/c$. So for $t = 0$ and $z = 0$ (hence the injection point in space and time) the phase is equal to ϕ_0. We now have:

$$\phi_{\text{sync}} - \phi_0 = \omega t - kz = \beta ckt - kz. \tag{3.29}$$

And from this it follows that the time of flight of the particle after a certain distance z can be expressed as:

$$T_{\text{g}} = \frac{\phi_{\text{sync}} - \phi_0 + kz}{\beta ck}. \tag{3.30}$$

The minimum time of flight is reached for $E_0 = 110\,\text{MV/m}$ at $\phi \approx 73\,\text{deg}$, which corresponds to an effective phase inside the first cell of 90 deg. This is the expected result if we define the maximum of the field to be at a phase of 90 deg, which is the standard definition for RF guns.

Exact Solution

It should be noted that the calculation only estimates the time of flight of the particle. In order to calculate the exact value of T_{g}, one has to integrate the $\gamma(z)$ dependent velocity of the particle over the desired flight distance. Noticing that

$$\beta(z) = \frac{\sqrt{\gamma(z)^2 - 1}}{\gamma(z)}, \tag{3.31}$$

it can be seen that this involves integrals of the form:

$$t = \frac{1}{c} \cdot \int_{z_1}^{z_2} \frac{\gamma(z)}{\sqrt{\gamma(z)^2 - 1}} \mathrm{d}z, \tag{3.32}$$

which cannot be solved analytically. They can of course be solved numerically. In order to get the exact time of flight for the REGAE gun cavity, one would then have to solve three integrals, accounting for the half cell section, the full cell section and the subsequent drift region. So T_{g} would then be:

$$T_{\text{g}} = t_{1/2} + t_1 + t_{\text{drift}}. \tag{3.33}$$

Small Deviations of the Phase

Since we are for now only interested in the time of flight changes caused by small phase changes in the gun system, it is not necessary to find the exact solution for $T(\phi_0, z)$. It is sufficient to focus on small time of flight differences caused by small phase differences of around one degree. The time of flight deviation due to small phase changes is then given by the derivative of T_g with respect to ϕ_0. In order to simplify the equations and to account for the fact that β is also a function of ϕ_0, $T_\mathrm{g}(\phi_0)$ can be written as

$$T_\mathrm{g}(\phi_0) = \frac{\phi_\mathrm{sync}(\phi_0) - \phi_0 + kz}{\beta(\phi_0) \cdot ck} = \frac{\tilde{T}_\mathrm{g}(\phi_0)}{\beta(\phi_0)}. \tag{3.34}$$

The derivative is thus given by

$$\frac{\mathrm{d}T_\mathrm{g}(\phi_0)}{\mathrm{d}\phi_0} = \frac{\mathrm{d}_{\phi_0}\tilde{T}(\phi_0)}{\beta(\phi_0)} - \frac{\tilde{T}(\phi_0) \cdot \mathrm{d}_{\phi_0}\beta(\phi_0)}{\beta(\phi_0)^2}, \tag{3.35}$$

where the abbreviation $\mathrm{d}_{\phi_0} = \mathrm{d}/\mathrm{d}\phi_0$ has been used. The derivative of $\tilde{T}_\mathrm{g}$ is given by

$$\frac{\mathrm{d}\tilde{T}_\mathrm{g}}{\mathrm{d}\phi_0} = \frac{1}{ck} \cdot \left(\frac{\mathrm{d}\phi_\mathrm{sync}(\phi_0)}{\mathrm{d}\phi_0} - 1 \right), \tag{3.36}$$

where the derivative of the synchronous phase with respect to ϕ_0 can be calculated using its definition 3.26 and the fact that

$$\frac{\mathrm{d}}{\mathrm{d}x} \csc(x) = -\frac{\cos(x)}{\sin^2(x)} \tag{3.37}$$

It is also called the *bunch compression factor*. Using this result we then get

$$\frac{\mathrm{d}T_\mathrm{g}}{\mathrm{d}\phi_0} = \frac{1}{\beta(\phi_0)^2 ck} \cdot \left[\frac{\beta(\phi_0)}{2\alpha} \cdot \frac{\cos(\phi_\mathrm{eff})}{\sin^2(\phi_\mathrm{eff})} - (\phi_\mathrm{sync}(\phi_0) - \phi_0 + kz) \cdot \mathrm{d}_{\phi_0}\beta(\phi_0) \right]. \tag{3.38}$$

Under the assumption that β is approximately constant, i. e. for a ϕ_0 close to an effective phase of 90 deg, the following simplified expression can be found. Since β is now constant regardless of a small phase change $\delta\phi$, the second term in equation 3.38, which accounts for time of flight differences in the drift region after the gun (z-dependence), vanishes and

$$\frac{\mathrm{d}T_\mathrm{g}}{\mathrm{d}\phi_0} \approx \frac{1}{\beta ck} \left(\frac{1}{2\alpha} \cdot \frac{\cos(\phi_\mathrm{eff})}{\sin^2(\phi_\mathrm{eff})} \right). \tag{3.39}$$

In order to obtain the more accurate approximation 3.38, the phase dependent velocity $\beta(\phi_0)c$ has to be calculated. The energy gain inside the cavity across the

distance $\Delta z = z_2 - z_1$ due to the RF field and under constant phase approximation is given by ([12]):

$$\Delta\gamma(z_2, z_1) = \alpha \cdot \left[k\Delta z \sin(\tilde{\phi}) - \frac{1}{2}\left(\cos(\tilde{\phi} + 2kz_2) - \cos(\tilde{\phi} + 2kz_1)\right)\right], \tag{3.40}$$

where $\tilde{\phi}$ is ϕ_{eff} inside the half cell (in order to account for the phase slippage) and ϕ_{sync} inside the full cell of the REGAE gun cavity. The total energy gain for the REGAE 1.5 cell gun is then given by the sum of the contributions of each individual cell. Therefore

$$\gamma_{\text{g}} = 1 + \Delta\gamma(z_{1/2}, 0) + \Delta\gamma(z_{\text{g}}, z_{1/2}), \tag{3.41}$$

where z_{g} is the length of both cells and $z_{1/2}$ is the length of the half cell. Using this result and

$$\beta(\phi_0) = \frac{\sqrt{\gamma(\phi_0)^2 - 1}}{\gamma(\phi_0)} \tag{3.42}$$

equation 3.38 can be evaluated. Figure 3.6 shows a comparison of results from ASTRA simulations and values obtained using equation 3.38. One can see that

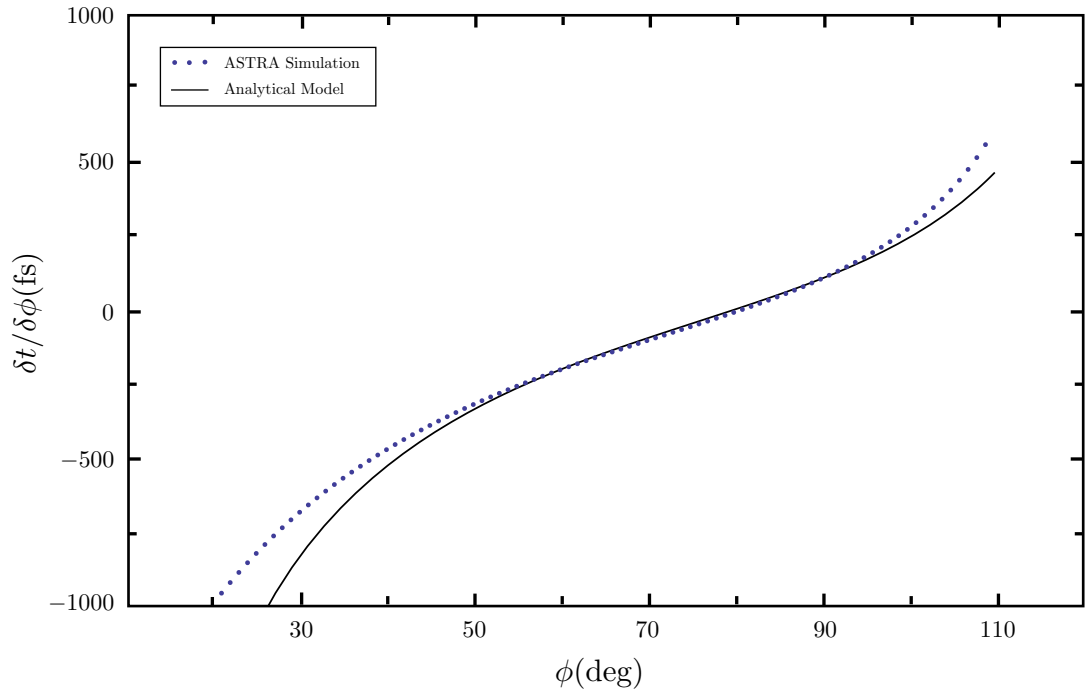

Figure 3.6: Time of flight deviations due to small phase changes $\delta\phi$ in the gun cavity.

equation 3.38 is very close to the numerical solution, except for the extreme cases. Differences from the ASTRA results are due to the fact that an ideal RF-field (sine) has been assumed. ASTRA in turn uses the real field map of the REGAE gun. Another reason for the differences is the fact that the REGAE gun incorporates a so called *elongated half-cell*, which is also taken into account in the ASTRA simulations. Elongation of the half cell results in an increase of the energy gain in the half cell. The elongation length is obtained via optimization calculations that take space charge effects into account ([38]).

Buncher Cavity

In order to determine the time of flight variations induced by the phase changes of the buncher cavity, one first has to look at the energy gain of the particles inside of a full RF cell, which is given by equation 3.40. For the buncher cavity a constant ϕ can be assumed, because the particles have already reached ϕ_{sync} in the gun cavity. Using $\phi_0 = \phi_{\text{sync}}$ and equation 3.30, the time of flight is given by

$$T_{\text{b}} = \frac{z - z_0}{\beta_{\text{b}} c}, \tag{3.43}$$

where z_0 is the position of the first cell of the buncher cavity. The velocity βc can again be calculated via the energy gain. As it has been already discussed in chapter 2, the REGAE buncher cavity is comprised of four full cells, hence the energy gain inside the buncher is given by four times the energy gain due to a full cell. A full cell has exactly the length of a half wavelength, therefore in this case $z_2 = z_1 + \lambda/2$. Inserting this into equation 3.40, we get

$$\begin{aligned} \Delta\gamma &= \alpha \cdot \left[\frac{k\lambda}{2} \sin(\phi) - \frac{1}{2} \left(\cos(\phi + 2kz_1 + 2\pi) - \cos(\phi + 2kz_1) \right) \right] \\ &= \alpha \cdot \left[\frac{2\pi\lambda}{2\lambda} \sin(\phi) - \frac{1}{2} \left(\cos(\phi + 2kz_1) - \cos(\phi + 2kz_1) \right) \right] \\ &= \alpha\pi \cdot \sin(\phi). \end{aligned} \tag{3.44}$$

Therefore

$$\Delta\gamma_{\text{b}} = 4\pi\alpha_{\text{b}} \cdot \sin(\phi), \tag{3.45}$$

where α_{b} is the normalized vector potential of the buncher cavity. Hence β_{b} in equation 3.43 is given by

$$\beta_{\text{b}} = \beta_{\text{b}}(\gamma_0 + \Delta\gamma_{\text{b}}), \tag{3.46}$$

where γ_0 is the initial γ of the incoming particle. The time of flight deviation due to small buncher phase changes is now given by the derivative of equation 3.43

with respect to the buncher phase. Figure 3.7 shows the time of flight deviation for $\Delta z = 2.21\,\mathrm{m}$ calculated using equation 3.43 compared to ASTRA simulations. It can be seen that the analytical solution approximates the ASTRA simulations very well over a large phase region, but fails to describe the extreme cases sufficiently. For phases smaller than 0 the electrons start to be decelerated, which cannot be described by this model sufficiently. The other extreme case is the debunching case. These cases can however be neglected, since only phases around 0 deg (bunching), or 90 deg (maximum energy gain) are of interest in most cases.

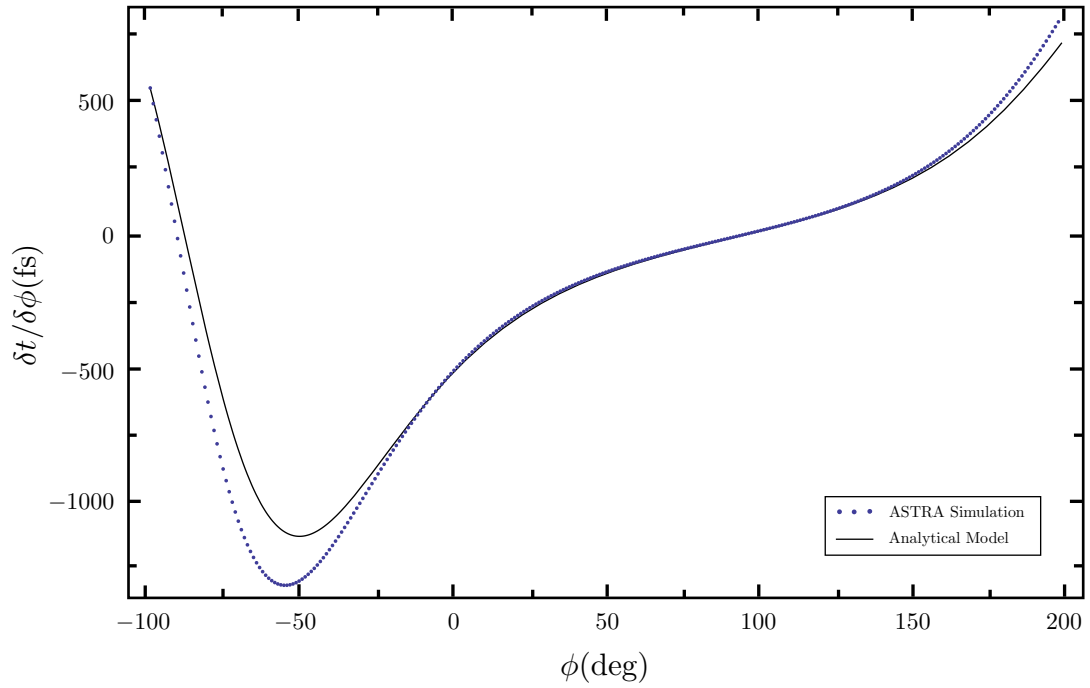

Figure 3.7: Time of flight deviations due to small phase changes $\delta\phi$ in the buncher cavity at $z = 2.21\,\mathrm{m}$.

Combining Gun and Buncher

The total time of flight jitter of the whole system is essentially determined by three phase jitter sources: gun phase jitter, buncher phase jitter and the so called common phase jitter. Gun and buncher phase jitter can for example be caused by temperature fluctuations which result in the expansion or contraction of the copper material. This in turn causes a change of the resonant behavior of the respective cavities and hence their resonant frequencies. As both cavities are fed

by one single klystron, phase jitter originating from the klystron causes a phase jitter on both cavities, the common phase jitter. Two things now have to be taken into account. First of all γ_0 in equation 3.46 now depends on the gun phase ϕ_g and hence

$$\beta_\mathrm{b} = \beta_\mathrm{b}(\phi_\mathrm{b}, \phi_\mathrm{g}) = \beta_\mathrm{b}(\gamma_\mathrm{g}(\phi_\mathrm{g}) + \Delta\gamma_\mathrm{b}(\phi_\mathrm{b})). \tag{3.47}$$

Secondly, the fact that the time of flight between the two cavities depends on the gun phase, has to be taken into account. In normal operation the two cavity phases ϕ_g and ϕ_b are adjusted to maximum energy gain and maximum bunching respectively. It is important to note now that due to phase dependent time of flight between the cavities, ϕ_b is in configured phase only for fixed ϕ_g. An electron with a shorter or longer time of flight will arrive at a different phase in the buncher. In other words, a gun phase jitter corresponds to a buncher phase jitter. Therefore a correction has to be added to the buncher phase and ϕ_b is now a function of the gun phase. Thus

$$\phi_\mathrm{b}(\phi_\mathrm{g}) = \phi_\mathrm{b} + \tilde{\phi}(\phi_\mathrm{g}), \tag{3.48}$$

where the correction phase is given by

$$\tilde{\phi}(\phi_\mathrm{g}) = \beta_\mathrm{g}(\phi_\mathrm{g})ck \cdot \frac{\mathrm{d}T_\mathrm{g}(\phi_\mathrm{g})}{\mathrm{d}\phi_\mathrm{g}} \cdot (\phi_\mathrm{g} - \phi_\mathrm{g}^0). \tag{3.49}$$

The factor $(\phi_\mathrm{g} - \phi_\mathrm{g}^0)$ ensures that the correction is only applied for phase deviations $\delta\phi$ from ϕ_g^0 (it is assumed that the machine has been configured for a fixed pair of ϕ_g^0 and ϕ_b). This phase correction also has to be taken into account in the context of the arbitrary phase tool (see section 2.5). It has to be noted that this effect can also lead to compensation effects. These compensation effects can in fact be interpreted as the higher order effects, which have been observed in the sensitivity analysis.

In order to describe the effects of the different phase jitter sources on the time of flight, one now has to combine the formulae that have been derived above, keeping in mind the phase correction. Hence

$$T_\mathrm{ges}(\phi_\mathrm{g}, \phi_\mathrm{b}, \phi_\mathrm{c}) = T_\mathrm{g}(\phi_\mathrm{g}, \phi_\mathrm{c}) + T_\mathrm{b}(\phi_\mathrm{g}, \phi_\mathrm{c}, \phi_\mathrm{b} + \tilde{\phi}(\phi_\mathrm{g})), \tag{3.50}$$

where ϕ_c is a phase factor which can be introduced into the formulae as a phase term that is added to both the gun and buncher phases, in order to account for the common phase changes. The three jitter contributions can then be calculated by deriving the total time of flight with respect to ϕ_g,ϕ_b, or the common phase ϕ_c. Since the time of flight of a particle also depends on the RF amplitude ($\alpha = \alpha(E_0)$), equation 3.50 can also be derived with respect to the gun and buncher amplitudes.

The phase correction factor in this case depends on the gun amplitude. Table 3.4 shows the expected time of flight deviation per degree and MV/m for all of the three contributions at a typical phase setting of maximum energy gain and bunching at a z-position of 5.5 m (REGAE target chamber). From these results it can be seen that in order to reach a 10 fs time of flight stability a phase stability on the order of $7 \cdot 10^{-3}$ deg and 0.01 MV/m is necessary. It is important to note that the result for the buncher cavity is only valid for an ideal field (sine) at zero crossing phase. A deviation of 1 deg from this setting results in an increase of the $E_{0,\mathrm{g}}$ contribution by 40 fs/(MV/m).

Table 3.4: Time of flight deviation due to small phase and amplitude changes. The values have been obtained using equation 3.50 and a phase setting for maximum energy gain and bunching and $z = 5.5\,\mathrm{m}$

Contribution	**Value (fs/deg)**	**Contribution**	**Value (fs/(MV/m))**
ϕ_g	86	$E_{0,\mathrm{g}}$	-1010
ϕ_b	-1434	$E_{0,\mathrm{b}}$	0
ϕ_c	-1348	$E_{0,\mathrm{c}}$	-1010

In order to study the compensation effects due to the time of flight differences between the cavities, a Monte Carlo experiment has been performed using equation 3.50. The phases have been set to the maximum energy gain for the gun and the bunching phase for the buncher cavity, i. e. usual operation settings. Normally distributed phase errors of the order of 0.03 deg have been applied to the cavity phases, as well as the common phase. Table 3.5 shows the resulting normalized standard deviations for all possible jitter scenarios. It can be seen that in all cases

Table 3.5: Results of a Monte Carlo experiment that determines the effect of the time of flight differences between the cavities. Values are normalized.

Jitter applied to			ϕ_b	$\phi_\mathrm{b} + \tilde{\phi}(\phi_\mathrm{g})$
ϕ_g	ϕ_b	ϕ_c	1	0.95
ϕ_g	ϕ_b	–	0.69	0.69
ϕ_g	–	–	0.03	0.04
ϕ_g	–	ϕ_c	0.72	0.65
–	ϕ_b	ϕ_c	0.99	0.95
–	–	ϕ_c	0.72	0.65
–	ϕ_b	–	0.69	0.7

where the common phase is involved a compensation of approximately 6 % can be observed. Recalling the two figures 3.6 and 3.7 this makes sense for the phase settings that have been used for the experiment. The gun phase jitter induces a positive time of flight deviation and the buncher phase jitter a negative one.

Considering the compensation effects, another interesting question is whether there exists a pair of $(\phi_\mathrm{g}, \phi_\mathrm{b})$ with minimal standard deviation of the time of flight. Therefore a second Monte Carlo experiment has been performed for differ ent phase settings. Figure 3.8 shows the results of the numerical experiment in form of a density plot. The phase range has been chosen to be compliant to usual operation phases for both cavities (ϕ_g), where $\phi_\mathrm{g} = 0\,\mathrm{deg}$ is now defined as the phase for maximum energy gain and $\phi_b = -90\,\mathrm{deg}$ as the bunching phase. The numerical experiment shows that there is indeed a minimum. This minimum occurs for the case of both cavities being set to an accelerating phase, which is the expected result. In the usual operating setup (maximum energy gain + bunching) a much higher jitter is expected due to the off-crest operation mode of the buncher cavity. This circumstance is also confirmed by the numerical experiment. The compensation effect can thus not be leveraged.

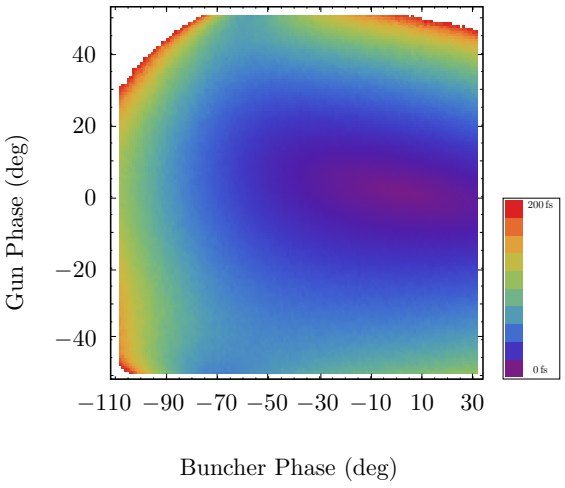

Figure 3.8: Density plot of the standard deviation of the time of flight obtained via a Monte Carlo experiment using equation 3.50 for different cavity phase settings.

Concluding Remarks

In this section the physical background of time of flight deviations due to small phase changes has been discussed. Three important insights can be extracted. First of all there are three different phase jitter sources, which have independent sources and can compensate each other. The second insight is the fact that a gun phase jitter leads to an additional buncher phase jitter, because of the change in time of flight between the two cavities. Finally the requirements for 10 fs time of flight stability are $7 \cdot 10^{-3}$ deg and 0.01 MV/m according to the analytical model.

In the following section the analytical approximations will be used to estimate the time of flight jitter at REGAE based on actual phase jitter measurements.

3.2.2 Measurement of the RF Phase Stability using the Phase Scan Technique

As it has been discussed above, the RF phase is a very important parameter especially for the beam energy and hence the time of flight of the electron bunch. It is therefore necessary to know the phase jitter as accurate as possible. There are several methods for measuring the RF phase. The first method is the measurement of the phase inside the cavities using a probe antenna. This way both the gun and the buncher phase and the gun phase jitter can be measured easily. One thing to keep in mind here is the fact that this method is indeed a so called *in-loop* measurement. The real phase stability is determined by the bandwidth of the cavity (gun $\pi-$mode: 462 kHz, see chapter 2.6.4), which leads to a much more stable phase. Knowing this, it becomes clear that a method based on beam diagnostics should be used in order to determine the real phase jitter. A very accurate technique is the so called *phase scan method*, where the electron bunch charge is measured at a phase where the charge is most sensitive to small changes in the phase ([39]). Figure 3.9 shows an ASTRA simulation of the gun phase dependent bunch charge, as well as the the four main regimes. The simulation determines the charge at the position of the first diagnostics station (DDC1, $z =$ 693 mm), where the first of three Faraday cups is installed. Regime (I) describes the case where no electrons arrive at the Faraday cup due to the immediate deceleration inside of the half-cell. The electrons essentially get pushed back onto the cathode. In regime (II) parts of the electron bunch are emitted into an accelerating phase; at the phase $\phi_{1/2}$, 50 % of the emitted electrons are accelerated and can therefore be detected. Phase region (III) shows a monotonic increase of the charge. This can be explained by the *Schottky effect*, which leads to a decrease of the work function inside the Cs_2Te cathode that can be attributed to higher field gradients at the

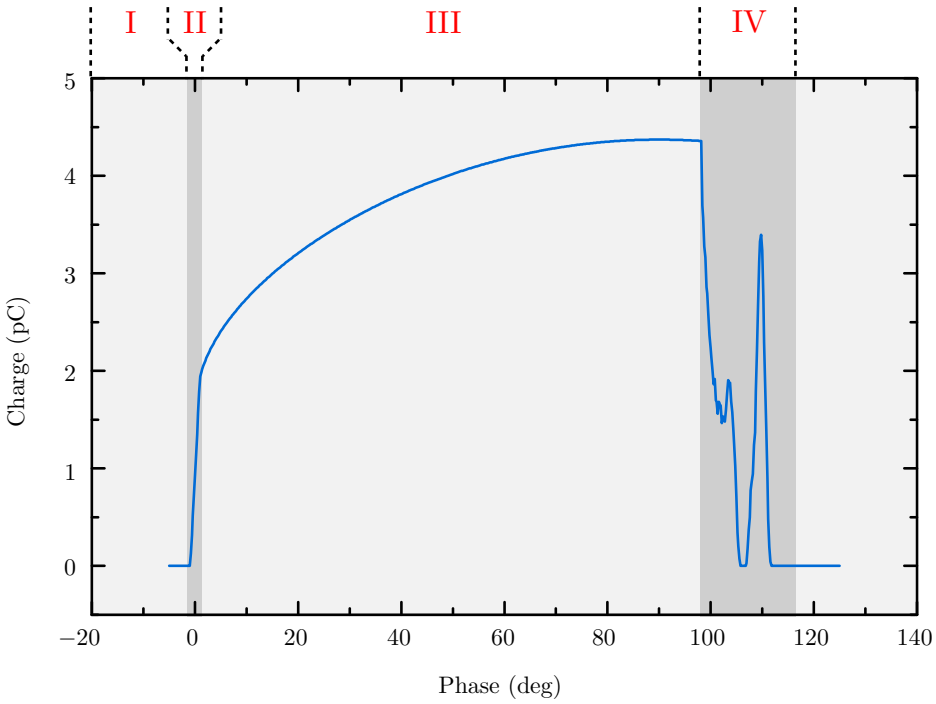

Figure 3.9: ASTRA simulation of the gun phase dependent charge at DDC1. Gun amplitude: 60 MV/m.

cathode. A decreased work function leads to an increase of emitted electrons and hence the monotonic increase in charge ([40]). The last regime (IV) is the regime, where parts of the beam get accelerated in the half-cell, but decelerated, or even reflected in the full-cell. Reflected electrons can then produce secondary electrons, if they hit the cathode. Secondary electrons that oscillate collectively in the RF field of the cavity can then also cause the so called *multipacting* effect, which leads to an avalanche of newly emitted electron if the secondary electron yield is high enough (bigger than 1, see [41]). Looking at figure 3.9, it becomes apparent that the most sensitive phase is $\phi_{1/2}$. Thus a phase stability measurement can now be performed by first scanning the phase and then measuring the charge jitter at $\phi_{1/2}$. Since the increase in charge around this phase is almost linear, the charge jitter can then readily be related to a phase jitter.

Measurement at REGAE

In order to conduct the measurement according to the method described above, two self-written diagnostics tools in MATLAB have been used. They both interface

with data acquisition servers, which collect all the diagnostics data and provide them via the *TINE protocol* (cf. [42] for details on the protocol). The first tool (FM_PhaseScanTool) performs a phase scan and records the charge on one of the Faraday cups, whereas the second (FM_ReadOutTool) can be used to display and also record diagnostics data to disk.

The phase stability measurement has been performed for four different machine setups:

(1) No feedback

(2) With analogue feedback

(3) With digital learning feedforward correction (LLRF)

(4) With digital learning feedforward correction (LLRF) and analogue feedback.

The comparison of these cases should show the effects of both the feedback and the LLRF (low level RF) feedforward correction. The analogue feedback system is essentially a simple proportional type feedback loop, with acts on the klystron phase according to the error signal at the gun probe antenna. Since this system — being p-type — acts very fast, an improvement of the overall RMS stability is expected. The learning feedforward correction (LFF) is an adaptive algorithm, acting on the LLRF part of REGAE, specifically the so called *feedforward tables* that define the output pulse shape. It tries to keep the amplitude of the pulse, where the electron bunch is emitted in time, as flat as possible. In addition to that, the phase is also tried to be kept as constant as possible during this period of time. Because the algorithm averages over 10 pulses, only relatively slow drifts are expected to be corrected by the LFF.

Case (1)

Figure 3.10 shows the complete phase scan for the charge at the Faraday cup (DDC1). All of the following measurements have been conducted using this diagnostic. The data shown is an average over five consecutive measurements. For all of the following measurements the gun amplitude had been set to 60 MV/m. In comparison to the ASTRA simulation shown above, the signal is much noisier. This noise might be attributed to space charge effects, since the measurement has been conducted at a relatively low gun gradient of 60 MV/m and high values of the charge up to approximately 4.5 pC. For the stability measurement two phases have been chosen; one on the first flank of the charge curve (postive slope) and one on the second flank (negative slope). In addition to that, a third measurement has

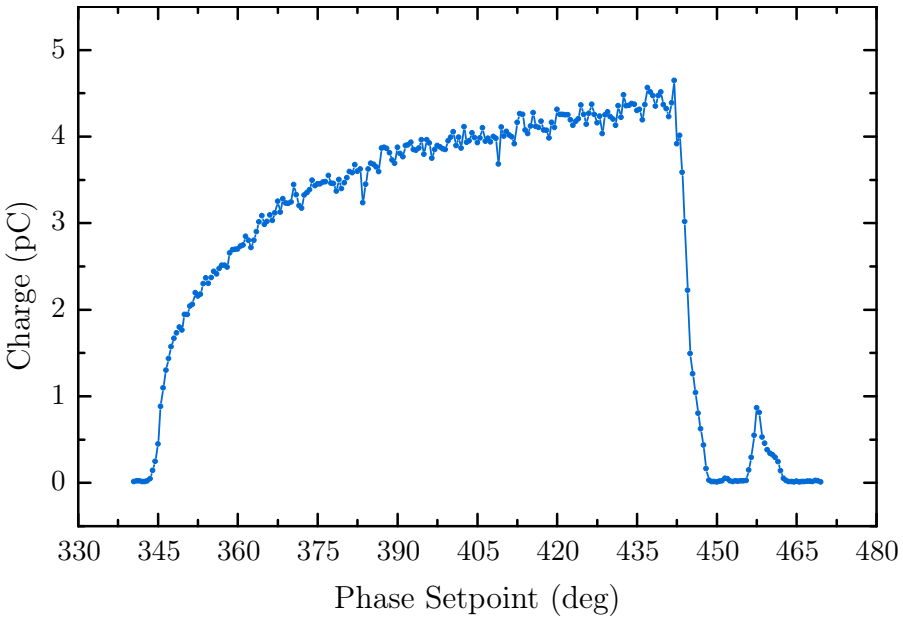

Figure 3.10: Phase scan of the charge at the Faraday cup (DDC1). The analogue feedback, as well as the learning feedforward correction had been turned off.

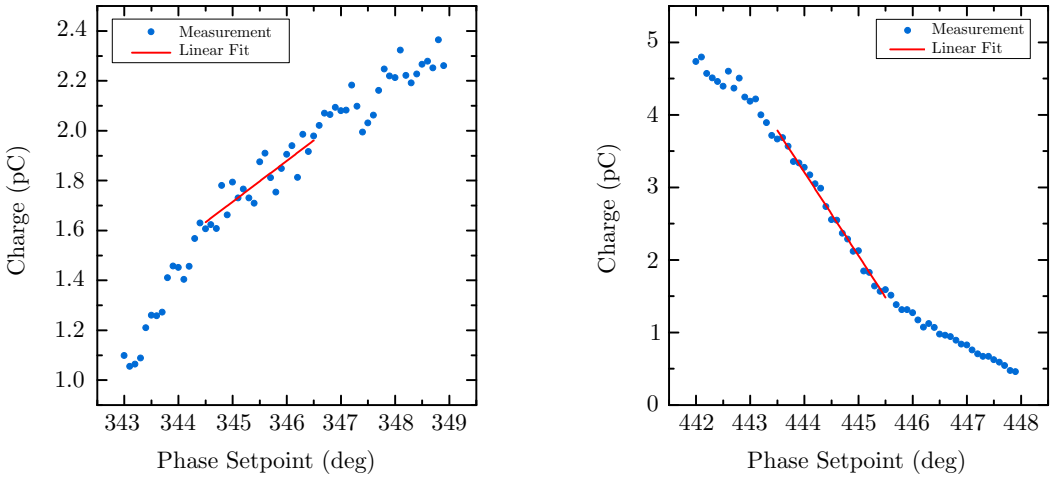

Figure 3.11: Detailed phase scan of the charge at the Faraday cup (DDC1). The left plot shows the first flank, the right plot the second one. Both plots also include the linear fit curve ±1 deg around the phase the measurement was conducted at.

been performed at a phase, where the charge is insensitive to phase changes, in order to determine the intrinsic noise of the Faraday cup, which ultimately limits the resolution of this technique. The charge jitter due to the Faraday cup and its digitization electronics have been determined to be 0.007 pC, which limits the accuracy of the measurement depending on the slope of the flank to approximately 20 fs. Data was recorded for a period of 5 min for every 6th pulse. Table 3.6 shows the results of this measurement. The time of flight jitter has been estimated for the target chamber position ($z = 5.5\,\mathrm{m}$) using the theory shown in section 3.2.1 assuming common phase jitter. Looking at the results, one can see the large RMS errors for this setting, which are also strongly different for each flank. This can be attributed to the phase drifts of up to approximately 0.19 deg/min that occurred during the measurement. They were caused by cavity temperature drifts of approximately -0.02 °C.

Table 3.6: Results of the RF phase stability measurement using the phase scan technique without any feedback. The in loop data has been measured using the gun probe antenna.

	RMSE – Beam based		**RMSE – In loop**	
	Phase (deg)	Time of flight (fs)	Phase (deg)	Time of flight (fs)
1st flank	0.182	245.336	0.173	233.204
2nd flank	0.311	419.228	0.341	459.668
Average	**0.247**	**332.956**	**0.257**	**346.436**

Case (2)

For the second case the analogue feedback was used. Again, two measurements were performed, one at each flank. The results (see table 3.7) show that the analogue feedback dramatically reduces the phase jitter, which is the expected result.

Case (3)

The third measurement was conducted using just the LFF and usual measurement scheme. Looking at table 3.8, one can see that the RMS values are between the cases (1) and (2) and almost the same as the RMS values for case (1), when the linear drift is removed (see table 3.8). It can therefore be concluded that the LFF reduces the slow phase drifts as expected. A more thorough analysis of data shows

Table 3.7: Results of the RF phase stability measurement using the phase scan technique with analogue feedback. The in loop data has been measured using the gun probe antenna.

	RMSE – Beam based		**RMSE – In loop**	
	Phase (deg)	Time of flight (fs)	Phase (deg)	Time of flight (fs)
1st flank	0.071	95.708	0.053	71.444
2nd flank	0.073	98.404	0.054	72.792
Average	**0.072**	**97.056**	**0.0535**	**72.118**

Table 3.8: Results of the RF phase stability measurement using the phase scan technique with LFF. The in loop data has been measured using the gun probe antenna.

	RMSE – Beam based		**RMSE – In loop**	
	Phase (deg)	Time of flight (fs)	Phase (deg)	Time of flight (fs)
1st flank	0.093	125.364	0.151	203.548
2nd flank	0.096	129.408	0.195	262.86
Average	**0.0945**	**127.386**	**0.173**	**233.204**

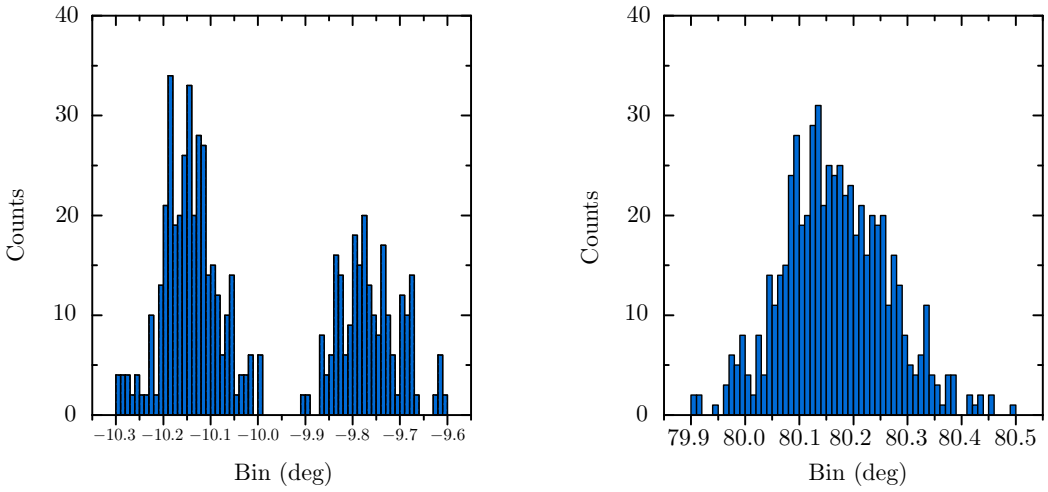

Figure 3.12: Histograms of the phase stability measurement at the second flank for both the gun probe signal (left plot) and the beam based signal via Faraday cup (right plot).

an interesting behavior of the vector modulator though. Comparison of the gun probe phase signal and the beam based phase signal for the second flank show a significant difference. Figure 3.12 shows histograms for both the gun phase signal measured via the probe and the beam based method. It can be seen that the probe signal is based upon two different normal distributions ($\sigma_{-10.2} = 0.047\,\text{deg}$ and $\sigma_{-9.8} = 0.066\,\text{deg}$). The beam based signal shows a single normal distribution with $\sigma_b = 0.096\,\text{deg}$. All other signals are also normally distributed. A scatter plot of the gun probe signal also reveals the two distributions (figure 3.13). It turns out that this phenomenon can be tracked down to the vector modulator, which produces a signal that jumps in phase between to central phases. This might be caused by crosstalk between signals in the master oscillator. At the time of the measurement (04.09.2012) the LLRF group had just changed the vector modulator board. The new board also suffered from sudden signal offsets that required a reset of the whole module. There are two question left to answer

1. Why can the phase jumps only be seen in the probe signal?

2. Why are the phase jumps not visible in the beam based phase signal?

The first question can be answered by noticing that the double distribution is also visible on the buncher phase. Due to the small bandwidth the system — in contrast to the klystron and waveguide system — reacts to the jumps, which

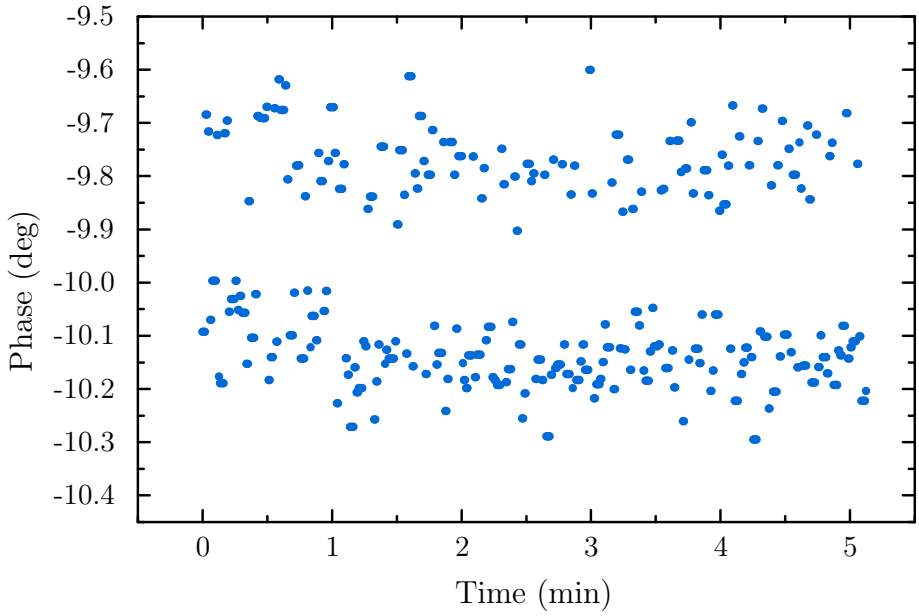

Figure 3.13: Raw gun probe data for the stability measurement at the second flank.

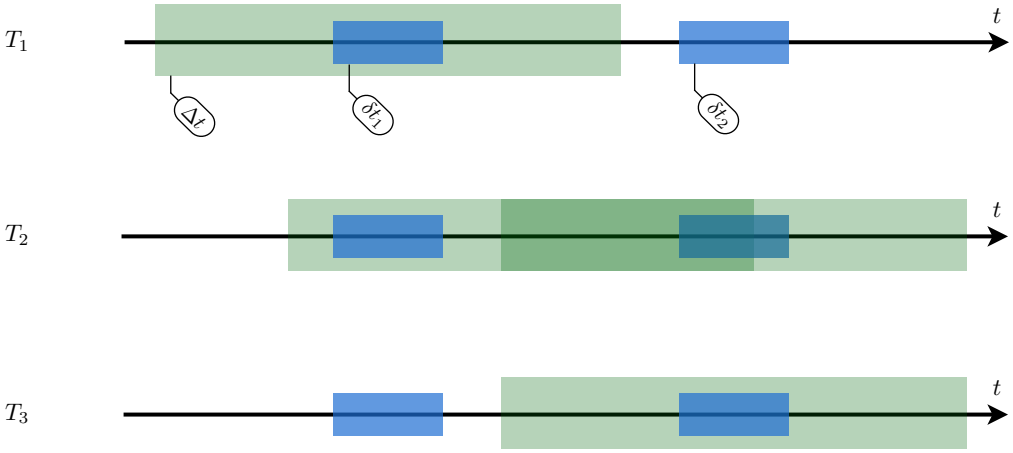

Figure 3.14: Illustration of how the adaptive window of the Faraday cup electronics works. δt_1 and δt_2 are the timing windows due to the phase jitter at the two center phases. Δt is the dynamic time window of the Faraday cup electronics. The three points T_i show different scenarios of data acquisition. Scenario T_2 depicts the case where the electronics mix the data from both δt_i.

is then visible in the measured signal. Answering the second question requires some knowledge of the Faraday cup electronics. The current electronics use an adaptive time window, which is centered around the bunch according to the signal history. Using an adaptive window improves the resolution of the measurement, which divides the pulse into 8 parts of 0.5 ns. If the phase and therefore the time of flight of the bunch (see section 3.2.1) now changes, the window needs to change its position in time. This can lead to a situation, where old and new data is mixed, if the window cannot adjust to the sudden phase jump fast enough. Figure 3.14 illustrates this problem. As a result the jitter on the beam based phase signal can now be understood as a convolution of the real phase jitter of the system and jitter of the jumps the vector modulator produces. Therefore the expected result is a single broadened normal distribution.

Case (4)

The last measurement was conducted using both the LFF and the analogue feedback. Table 3.9 shows the stability of this setup, which is — as expected — the best of the four. Unfortunately this measurement also suffered from RF jumps, which makes the interpretation of the individual results difficult.

Table 3.9: Results of the RF phase stability measurement using the phase scan technique with LFF and analogue feedback. The in loop data has been measured using the gun probe antenna.

	RMSE – Beam based		**RMSE – In loop**	
	Phase (deg)	Time of flight (fs)	Phase (deg)	Time of flight (fs)
1st flank	0.068	91.664	0.049	66.052
2nd flank	0.087	117.276	0.068	91.664
Average	**0.0775**	**104.47**	**0.0585**	**78.858**

Phase Stability with a new Vector Modulator

As a reaction to the problems described above the vector modulator has been replaced. In addition to that the master oscillator (that provides the 3 GHz reference signal) as well as the cabling had been checked.

The following measurement has been conducted on the basis of this new setup. Both the analogue feedback and the LFF had been turned on, because this setting turned out to be the most stable (see above). The results in terms of the RMS

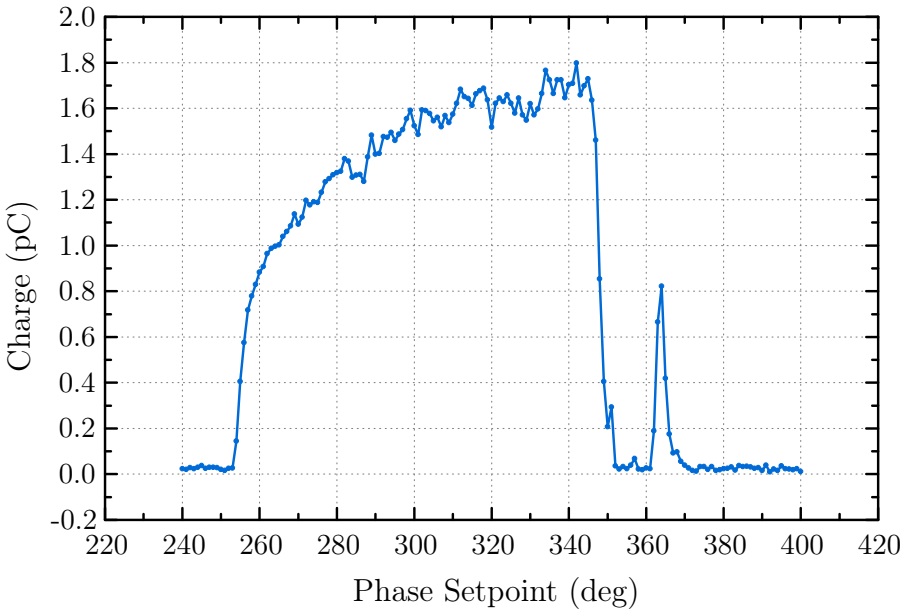

Figure 3.15: Phase scan of the charge at the Faraday cup (DDC1) using the new vector modulator setup. The analogue feedback, as well as the learning feedforward correction had been turned on.

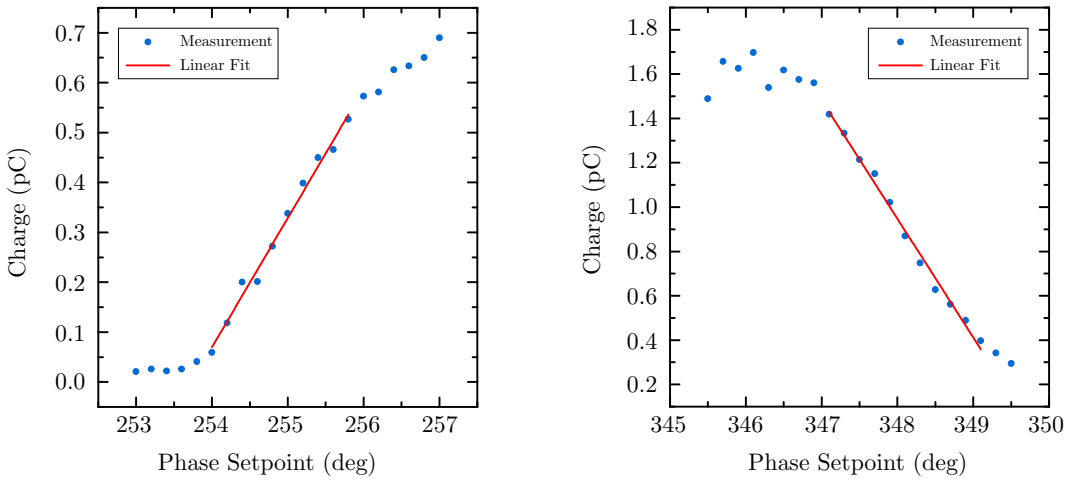

Figure 3.16: Detailed phase scan of the charge at the Faraday cup (DDC1) using the new vector modulator setup. The left plot shows the first flank, the right plot the second one. Both plots also include the linear fit curve ±1 deg around the phase the measurement was conducted at.

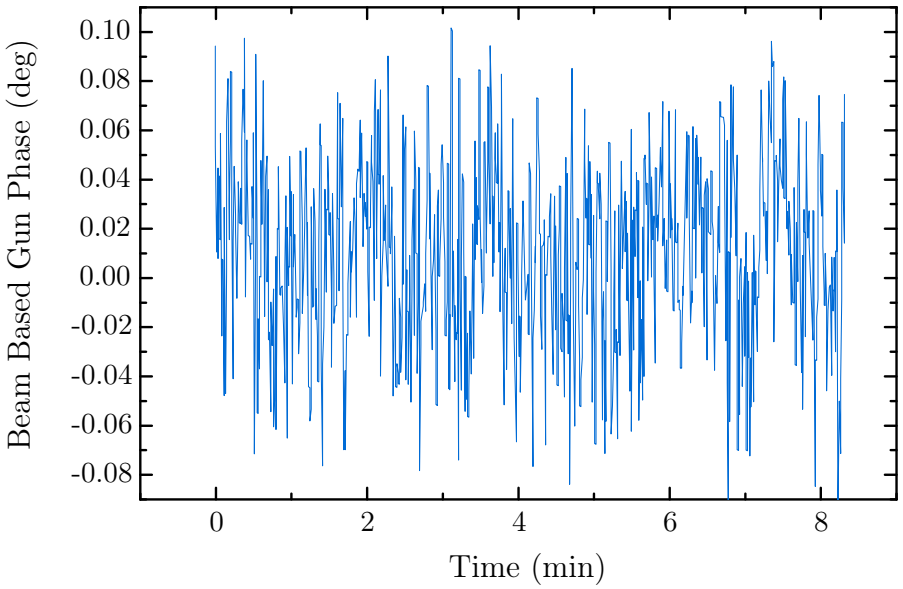

Figure 3.17: Raw data from the beam based phase stability measurement. The data has been recorded at the second flank.

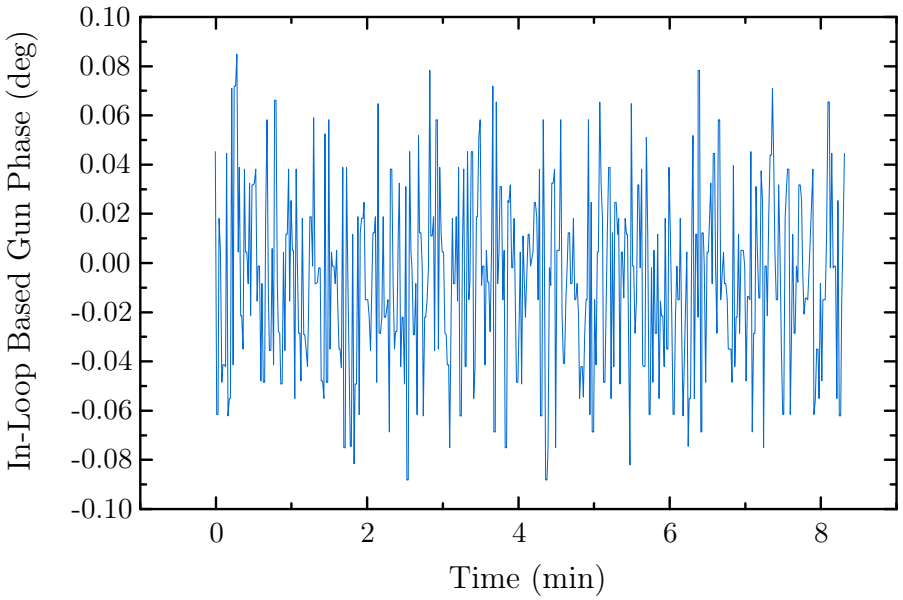

Figure 3.18: Raw data from the gun probe antenna based phase stability measurement. The data has been recorded at the second flank.

Table 3.10: Results of the RF phase stability measurement using the phase scan technique with LFF and analogue feedback, as well as the new vector modulator. The in loop data has been measured using the gun probe antenna.

	RMSE – Beam based		**RMSE – In loop**	
	Phase (deg)	Time of flight (fs)	Phase (deg)	Time of flight (fs)
1st flank	0.038	51.224	0.036	48.528
2nd flank	0.037	49.876	0.036	48.528
Average	**0.0375**	**50.55**	**0.036**	**48.528**

stability are shown in table 3.10. Looking at these results a significant improvement in comparison to the values obtained with the old setup can be observed. Figures 3.17 and 3.18 show the raw data for a period of approximately 8 min. In addition to the phase jitter, the gun amplitude jitter during this measurement has also been determined. Table 3.11 shows the results. It can be seen that the contribution to bunch time of flight jitter due to gun amplitude jitter is approximately 15% smaller than the contribution due to gun phase jitter. Although — due to the missing jumps in the phase — the beam based results of the phase measurement now almost match the ones measured in loop, a periodic perturbation of the charge signal that ultimately degrades the calculated RMS stability can be seen. In order to track down the source of this modulation, a readout for the laser power meter has been included into the data acquisition software.

Table 3.11: Results of the RF amplitude stability measurement using LFF and analogue feedback, as well as the new vector modulator. The in loop data has been measured using the gun probe antenna.

	RMSE – In loop	
	Amplitude (deg)	Time of flight (fs)
1st flank	0.039	39.39
2nd flank	0.043	43.43
Average	**0.041**	**41.41**

Side Note: Correlation of Time Series

One of the most important things one has to consider when the correlation of different time series needs to be determined is the simultaneity. This is especially important when time series need to be compared, which suffer from a lot of random noise. Using a simple Mathematica calculation, the problem can be illustrated. Consider two time series of data S_1 and S_2, where S_2 contains data that is linearly dependent on the data contained in S_1. Let S_1 contain normally distributed data and S_2 the linear function of the data in S_2, plus some additional random normally distributed jitter. Then a plot of S_1 vs. S_2 would look like the left one shown in figure 3.19. The linear dependence can readily be extracted from the scatter plot. Suppose the data is now shifted in time with respect to each other by just one data point (for the calculation 10000 data points have been used). Then the scatter plot would look like the right one shown in figure 3.19. No clear linear dependence can be extracted from the data. In reality the simultaneity of the data can also be randomly distributed over the time series, which would result in a mixture of the two scenarios.

In the case of all the measurements conducted for this thesis the simultaneity of the recorded data can only be guarantied, when the data is acquired from a single TINE server. In order to overcome the problem described above, the method of so called *2D cross covariograms* obtained using *sliding window cross-covariance* can be employed. Here the cross-covariance defined by

$$(f \star g)(x) = \int f^*(x)g(x+t)dt \tag{3.51}$$

is calculated for small time windows that "slide" over the whole time series. The cross-covariance is a measure of similarity of two functions f and g, therefore using the sliding windows the evolution of similarity and also possible offsets can be extracted from the resulting 2D map, or covariogram.

Figure 3.20 shows 2D covariograms for the phase stability measurement conducted using both analogue feedback and the LFF. It can be seen that the fluctuations in the laser intensity are clearly the dominant source of perturbation. From the structure of the covariogram the similarity of the two signals can be concluded. The other two possible sources show no significant similarity over the course of the measurement.

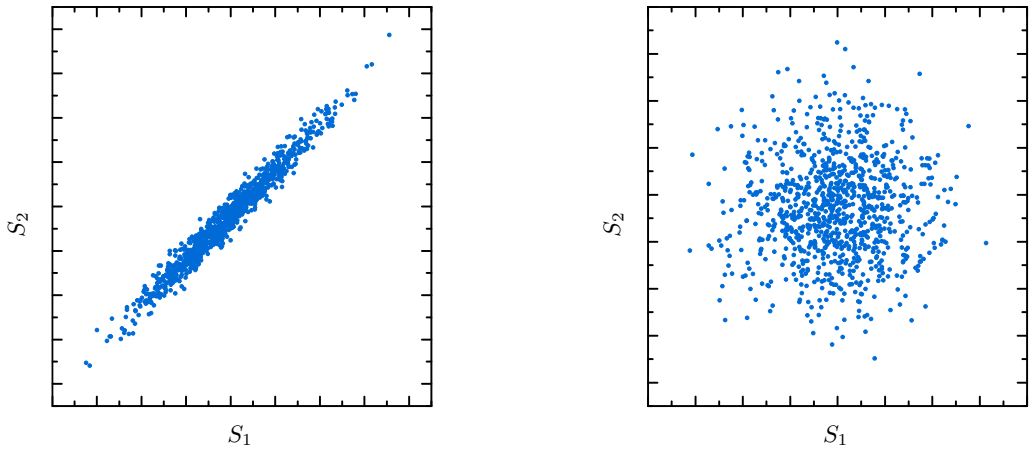

Figure 3.19: Comparison of two scatter plots for two different data acquisition scenarios. The left one corresponds to simultaneously taken data points, the left one to data with a slight temporal offset.

Temperature Stability

The data that has been presented above reveal a worsening of the phase stability when both the analogue feedback and the LFF are disabled. In order to estimate the effect of the cavity temperature stability on the RF phase stability, equation 2.38 in conjunction with the cavity parameters (see section 2.6.4) can be used. For the gun cavity a temperature change of 1 °C then results in a phase change of approximately 10 deg. At REGAE the gun cavity temperature RMS stability has been measured to be 0.027 °C. Therefore the expected RMS phase jitter due to temperature instability can be estimated to be 0.27 deg, which is in the order of to the phase jitter that has been measured for the 'no feedback' case.

Concluding remarks

The phase stability measurement shown above has characterized the current status of the REGAE machine in terms of phase stability. It has also revealed problems with the vector modulator that have an impact on the overall phase stability. This has been addressed by swapping the vector modulator and by identifying problems with the master oscillator. The measurement also contributed to the understanding of how the Faraday cup electronics work and how charge measurements using this diagnostic have to be interpreted. In addition to that it can be concluded from

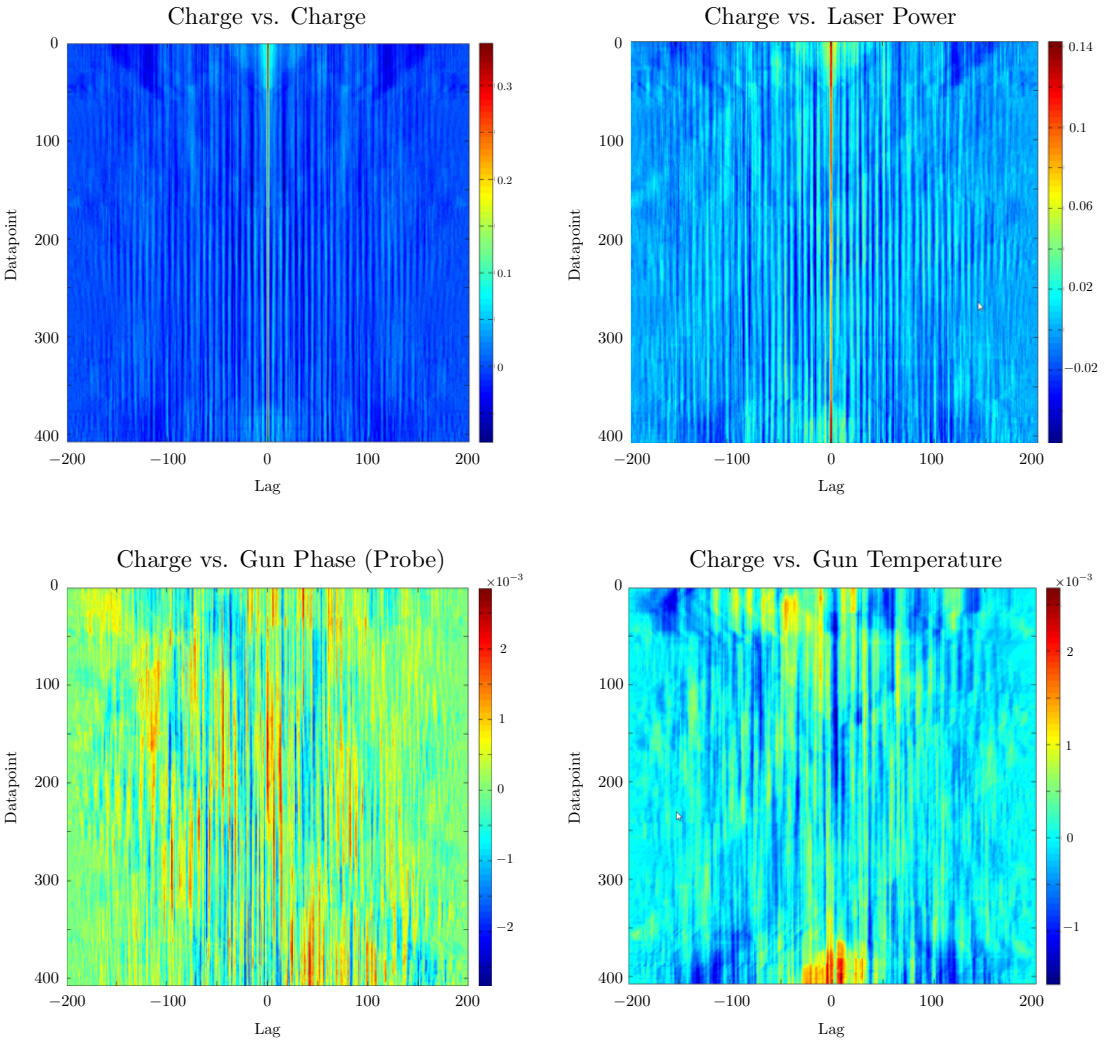

Figure 3.20: 2D cross-covariograms calculated using the sliding window cross-covariance method for three different possible jitter sources compared to the auto-covariogram of the charge signal.

the intrinsic noise level of the Faraday cup signal that the design phase stability of 0.01 deg cannot be measured using this kind of setup. The dark current monitor (DaMon) mentioned in section 1.1 is expected to provide a better resolution [43], but has not been available at the time of this thesis.

The current state of the machine allows for an RMS phase stability of approximately 50 fs. This value is a factor of 2 smaller than the 100 fs limit that has been discussed in the context of femtosecond electron diffraction, but does not comply with the stability requirements of external injection experiments. It has also been found out that the beam based measurements are strongly perturbed by the instability of the laser power. Improvements concerning temperature stability are currently in the works.

3.3 General Stability Studies

In this section the stability of several machine parameters will be discussed. Based on the results of the measurements the current status of the machine stability is evaluated.

3.3.1 Magnet Power Supplies

The stability of the solenoid power supplies is an important factor for the overall beam stability at REGAE. As it has been shown in the introductory chapter, the REGAE setup features three focusing elements in the form of solenoids (one single and two double solenoids). In addition to that, four steerer pairs are part of the beam optics. As part of the master thesis by Tim Gehrke a large Helmholtz type coil has been added to the design in order to compensate the earth's magnetic field (see [44]). An important device for the beam energy diagnostics is the dipole magnet, which is part of the spectrometer. The stability of the dipole magnet's field is therefore crucial for energy stability measurements conducted using the spectrometer.

All of the stability measurements have been conducted over-night using a MATLAB tool, which calculates the standard deviation over a given period of time for different current setpoints. The following stability data is based on 30 minutes of recorded data and is normalized to the respective current setting. The results can be seen in figures 3.21, 3.22 and 3.23. The data for the dipole is shown in figure 3.24.

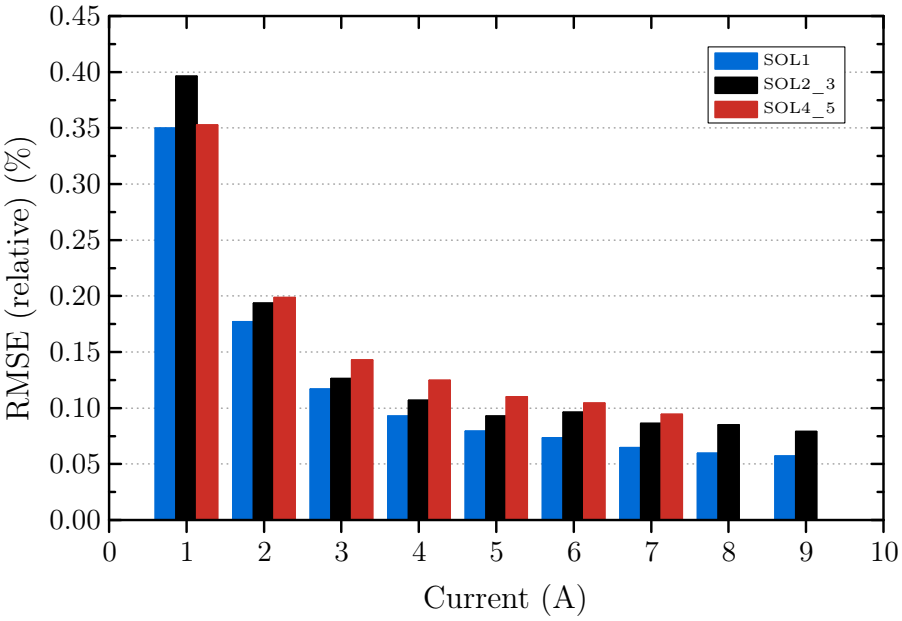

Figure 3.21: Stability measurement for the REGAE solenoid power supplies. Each data point corresponds to 30 min of recorded data.

Solenoids

From the results it can be seen that the power supplies are optimized for high currents $> 5\,A$. The solenoid power supply stability strongly depends on the current used in operation. In low-current situations the standard deviation can be as large as 0.4 %. For currents above 5 A the power supplies can be regarded as very stable with stabilities better than 0.1%. But how does the current actually affect the focusing of the solenoids? Particle motion in a magnetic field $\mathbf{B}$ is given by the *Lorentz force*

$$m\mathbf{a} = q\mathbf{v} \times \mathbf{B}. \tag{3.52}$$

Since we are interested in the focusing properties of the solenoid it makes sense to use cylindrical coordinates and to look at the radial component of the equation of motion. We then get

$$m(\ddot{r} - r\dot{\theta}^2) = qr\dot{\theta}B_z, \tag{3.53}$$

where r, θ and z are the components of the cylindrical coordinate system. From the other components it can be derived ([45]) that

$$\dot{\theta} = \frac{-q}{2m}B_z. \tag{3.54}$$

Using this and the fact that

$$\ddot{r} = d_t\dot{r} = d_t(d_z r d_t z) = d_z^2 r \cdot \dot{z}^2 + d_z r \cdot \ddot{z}, \tag{3.55}$$

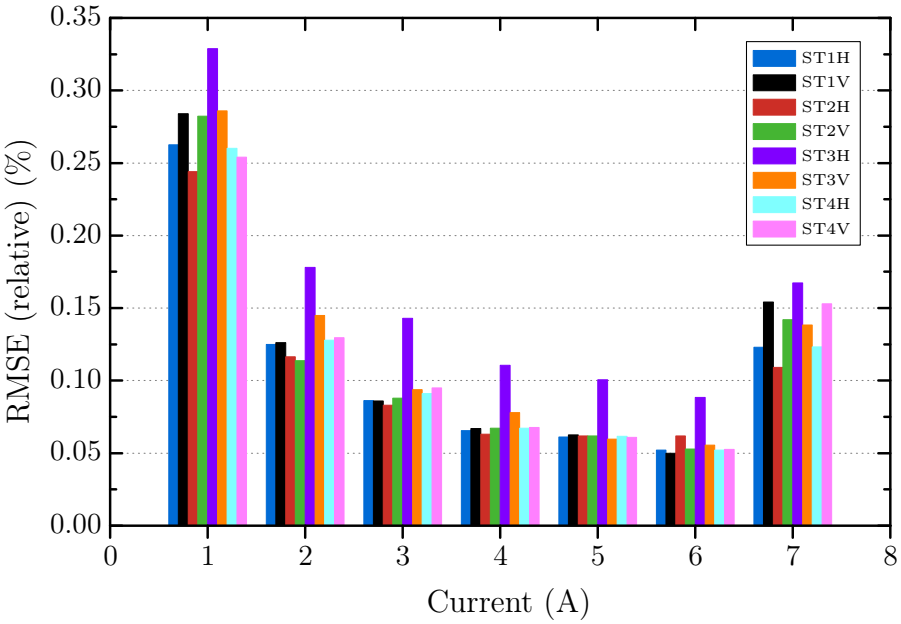

Figure 3.22: Stability measurement for the REGAE steerer magnet power supplies. Each data point corresponds to 30 min of recorded data.

equation 3.52 becomes

$$d_r^2 r = \frac{-q^2}{4p_z} B_z^2 r. \tag{3.56}$$

In thin lens approximation the focal length is defined as

$$\frac{1}{f} = \frac{-d_z r}{r}. \tag{3.57}$$

Therefore by integrating equation 3.56 and inserting the result into equation 3.57 we arrive at

$$\frac{1}{f} = \frac{q^2}{2p_z} \cdot \int B_z^2 dz. \tag{3.58}$$

The focal length is hence inversely proportional to the spatial integral over the square of the longitudinal magnetic field. Since the magnetic field of a solenoid is linearly dependent on the current I, it follows that

$$f \propto \frac{1}{I^2}. \tag{3.59}$$

A detailed derivation of the solenoid lens can be found in [46, 12].

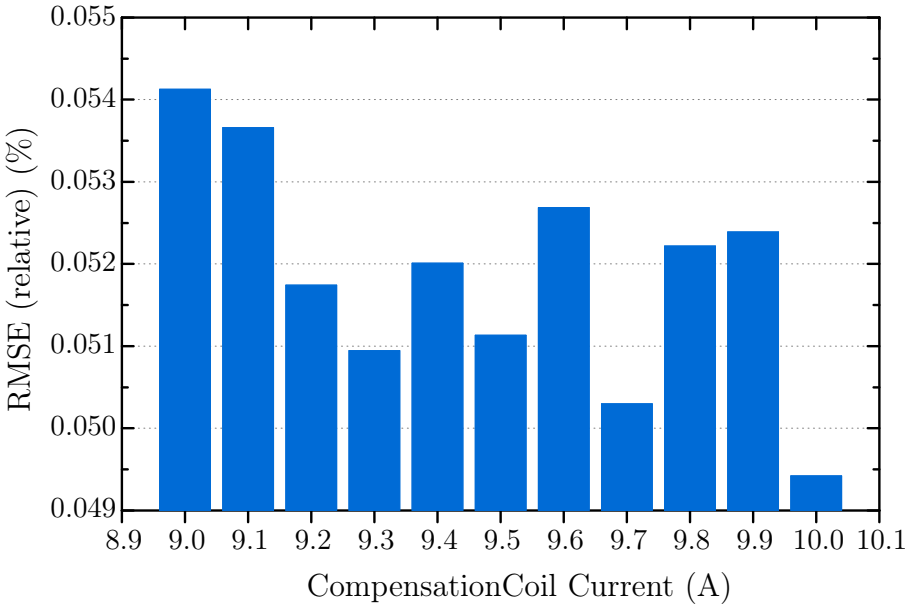

Figure 3.23: Stability measurement for the REGAE compensation coil power supply. Each data point corresponds to 30 min of recorded data. The data has been recorded around the usual set point of -9.75 A (optimal compensation of the earth's magnetic field).

Steerers

The steerer magnet power supplies behave similar to the solenoid power supplies, but the stability is generally about 0.05 % better due to a lower load. Interestingly the stability suddenly decreases at a current of 7 A. In addition to that it can also be seen that the third steerer pair is not as stable as the other ones. The ST3H power supply has the worst stability. It has to be noted that the steerer magnets should only be used at low fields in order to minimize large divergences when entering the solenoid lenses or the buncher cavity. Therefore it can be concluded that the power supplies of the steerer magnets are not optimized for usual machine operation.

Compensation Coil

As the compensation coil acts on the whole machine, a high stability of the power supplies is important. Looking at the result for the compensation coil, it can be seen that the power supply is stable up to approximately 0.055 %, which is a very good result. Since all power supplies are of the same type, it can be seen that they are optimized for high current operation. This clearly does not comply with the needs especially in the case of the steerer magnets.

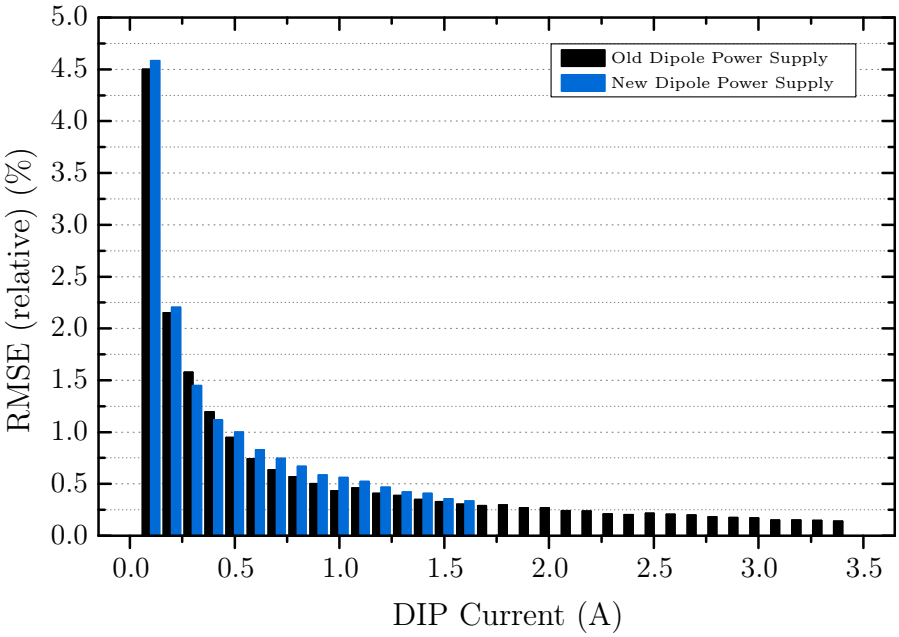

Figure 3.24: Stability measurement for the REGAE dipole power supply. Each data point corresponds to 30 min of recorded data.

Dipole

The dipole magnet is used as a dispersive element in the spectrometer section. Stability of the dipole's magnetic field is therefore crucial for determining the mean beam energy. Calibration of the dipole leads to the following linear relation:

$$E_{\text{beam}} \triangleq 4.072 \,\frac{\text{MeV}}{\text{A}} \cdot I_{\text{dip}} + 0.211\,\text{MeV}. \tag{3.60}$$

This calibration has been determined using simulations. During operation, the energy of the beam can then be determined by positioning the beam in the center of the x-axis of the screen using the dipole (see figure 3.25). At this position 3.60 holds. The beam position on the x-axis depends due to the layout of the dipole spectrometer on two main factors:

- Beam momentum p_z
- Dipole current I_{dip}.

Therefore a large jitter on the dipole current can on the one hand complicate the identification of the beam position and on the other hand also complicate energy stability measurements. In the following the effect of a current jitter on the x position of the beam will be discussed using transfer matrix formalism.

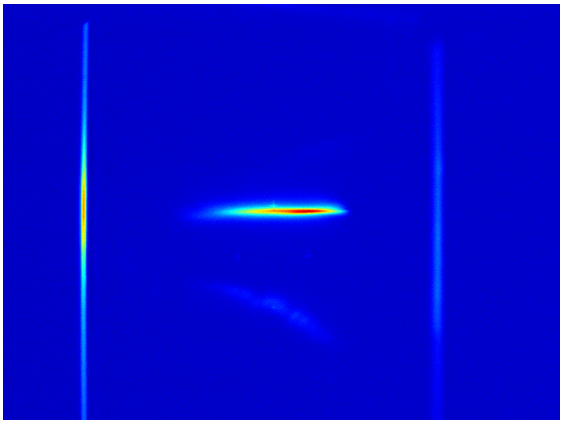

Figure 3.25: REGAE beam on the DC3 screen (dipole arm).

The dipole spectrometer can — as a first approximation — be thought of as a combination of an ideal dipole magnet and a drift section. In [47] the 6-dimensional transfer matrices have been derived to be

$$M_{\text{dip}} = \begin{pmatrix} \cos(\phi) & \rho\sin(\phi) & \rho(1-\cos(\phi)) & 0 & 0 & 0 \\ -\sin(\phi)/\rho & \cos(\phi) & \sin(\phi) & 0 & 0 & 0 \\ 0 & 0 & 1 & 0 & 0 & 0 \\ 0 & 0 & 0 & 1 & \rho\phi & 0 \\ 0 & 0 & 0 & 0 & 1 & 0 \\ 0 & 0 & 0 & 0 & 0 & 1 \end{pmatrix} \tag{3.61}$$

and

$$M_{\text{drift}} = \begin{pmatrix} 1 & d & 0 & 0 & 0 & 0 \\ 0 & 1 & 0 & 0 & 0 & 0 \\ 0 & 0 & 1 & 0 & 0 & 0 \\ 0 & 0 & 0 & 1 & d & 0 \\ 0 & 0 & 0 & 0 & 1 & 0 \\ 0 & 0 & 0 & 0 & 0 & 1 \end{pmatrix}, \tag{3.62}$$

where ρ is the bending radius, ϕ is the bending angle and d is the distance between dipole and DC3 screen. The beam itself is in this definition characterized by the vector $\mathbf{v} = (x_0, x_0', \Delta p/p, y_0, y_0', \Delta p/p)^T$. The x position on the screen can now be calculated via the matrix multiplication

$$M_{\text{drift}} \cdot M_{\text{dip}} \cdot \mathbf{v}. \tag{3.63}$$

Since we are interested in the effect of the current jitter, we need to relate the x-position to the current. For small changes in the current it is useful to map the

small ΔI_{dip} to small changes in the beam momentum Δp. The cyclotron radius ρ is defined as

$$\rho = \frac{p}{|q|B}, \tag{3.64}$$

where q is the charge of the electron. Using this we now get

$$\begin{aligned} \frac{p+\Delta p}{|e|B(I_{\mathrm{dip}})} &= \frac{p}{|e|B(I_{\mathrm{dip}}+\Delta I_{\mathrm{dip}})} \\ \Leftrightarrow \frac{\Delta p}{|e|B(I)} &= \frac{p}{|e|B(I_{\mathrm{dip}}+\Delta I_{\mathrm{dip}})} - \frac{p}{|e|B(I_{\mathrm{dip}})}, \\ \Leftrightarrow \Delta p &= p \cdot \left(\frac{B(I_{\mathrm{dip}})}{B(I_{\mathrm{dip}}+\Delta I_{\mathrm{dip}})} - 1 \right) \end{aligned} \tag{3.65}$$

where $B(I_{\mathrm{dip}})$ for REGAE has been determined to be

$$B(I_{\mathrm{dip}}) = 0.046\,\frac{\mathrm{T}}{\mathrm{A}} \cdot I_{\mathrm{dip}} + 0.006\,\mathrm{T}. \tag{3.66}$$

Implying ideal boundary conditions ($x_0 = 0, x_0' = 0$ and $\phi = \pi/2$) and using $d = 0.295\,\mathrm{m}$ at REGAE, it is now possible to calculate the jitter of the x position due to a dipole current jitter using the calibration 3.60.For a dipole current of 1 A, which — according to figure 3.24 — corresponds to a jitter of 0.43 %, the resulting jitter in the x-position is $\sigma_x = 2.17\,\mathrm{mm}$. On the DC3 screen each mm has been determined to correspond to 11.25 keV. Therefore the beam energy jitter can only be detected down to a standard deviation of 24.4 keV at this setting. This makes it almost impossible to perform reasonable energy stability measurements using the spectrometer arm. Such a measurement could be used to measure the bunch time of flight jitter caused by cavity amplitude jitter. In order to be sensitive to the required 10 fs, an energy resolution of at least 0.5 keV is necessary. This can be estimated using the theory shown in section 3.2.1. Therefore a more stable power supply must be incorporated into the setup in order to be able to perform reliable energy stability measurements. A modified version of the current power supply (see "New Dipole Power Supply" in figure 3.24) turned out to have an even worse stability.

3.3.2 Beam Pointing Stability

The REGAE accelerator is situated in the old *LINAC I* building, which is right next to the synchrotron *DESY II*. During DESY II operation, the REGAE beam has turned out to be less stable. Figure 3.26 shows two beam pointing measurements. One of the measurements had been performed at a time, where DESY II

had a scheduled maintenance day, whereas the other one on a day with DESY II operation. It turns out that the DESY "DI_DC_GM" magnet acts on the REGAE beam and therefore degrades the beam pointing stability. Table 3.12 shows the standard deviation of the beam center of mass position on the screen. It can be seen that during the DESY operation the pointing stability is reduced by a factor of 8.7 for the x-direction and by a factor of 2.2 in the y-direction. Currently the only way to avoid this problem, is to run REGAE at 12.5 Hz, which is the DESY II working frequency. In the future shielding will have to be installed at DESY to enable REGAE to run at different non-synchronized frequencies.

Table 3.12: Standard deviation of the beam center of mass position on the DDC2 screen.

	σ_x (μm)	σ_y (μm)
DESY Magnet OFF	4.92	17.57
DESY Magnet ON	42.99	38.85

3.3.3 Long Term Measurements

In the last sections short term stability of machine parameters has been discussed. This section will focus on long term ($> 5\,h$) measurements that have been conducted mostly over-night. For the following studies the MATLAB parameter readout tool *RFReadOutTool*, which is based on the *TINE MATLAB API* (see [42]) has been written and used. It is now also used in day to day operation as a readout panel.

Measurement with RF Rack Temperature Regulation

In order to determine the — at that time — current overall stability of the RF signals without feedback several LLRF parameters were recorded from 02-May-2012 21:30:34 to 03-May-2012 08:39:40 using the RFReadOutTool. During this period the machine had not been used for other experiments and the set-points for amplitude and phase were constant. Temperature regulation was active for all racks inside of the modulator room. Figures 3.27 and 3.28 show the recorded data for the different RF signals. From the data it can immediately be seen that there is a periodic modulation on both the phase and the amplitude signals. It has to be noted that for the phase signals the data range is $[-180\,\text{deg}, 180\,\text{deg}]$. This leads to folding effects in the data. A detailed view of the gun phase probe signal (see

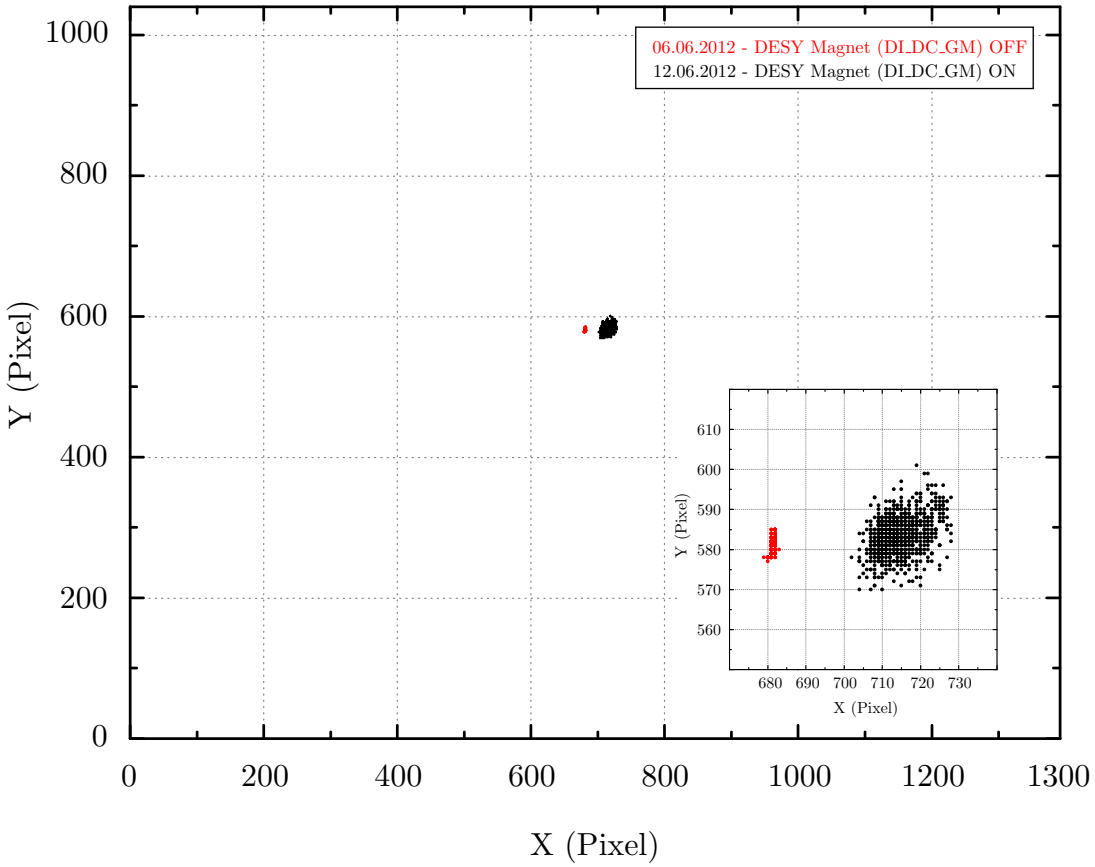

Figure 3.26: Comparison between two 10 min measurements of the REGAE electron beam pointing at DDC2. The X-Y range of the main plot corresponds to the complete visible area of the DDC2 screen. The inset shows a magnification.

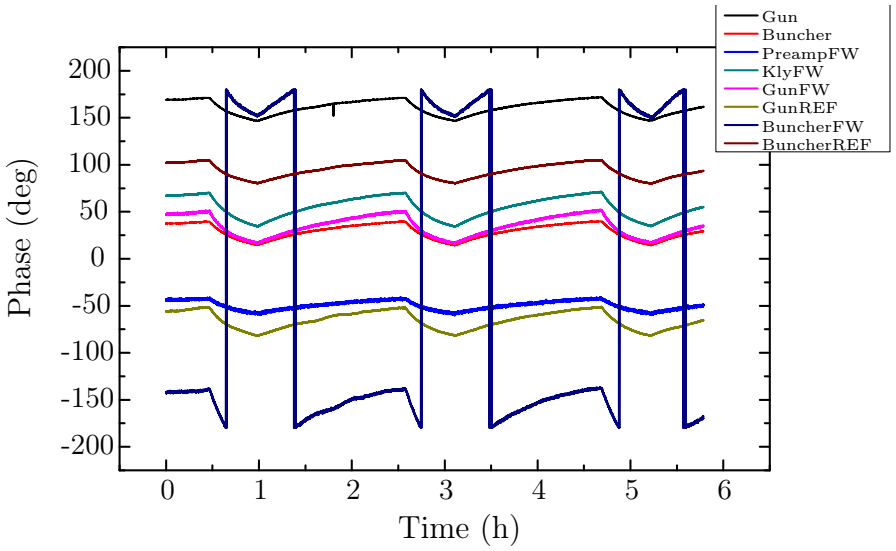

Figure 3.27: Recorded phase data from 02-May-2012 21:30:34 to 03-May-2012 08:39:40.

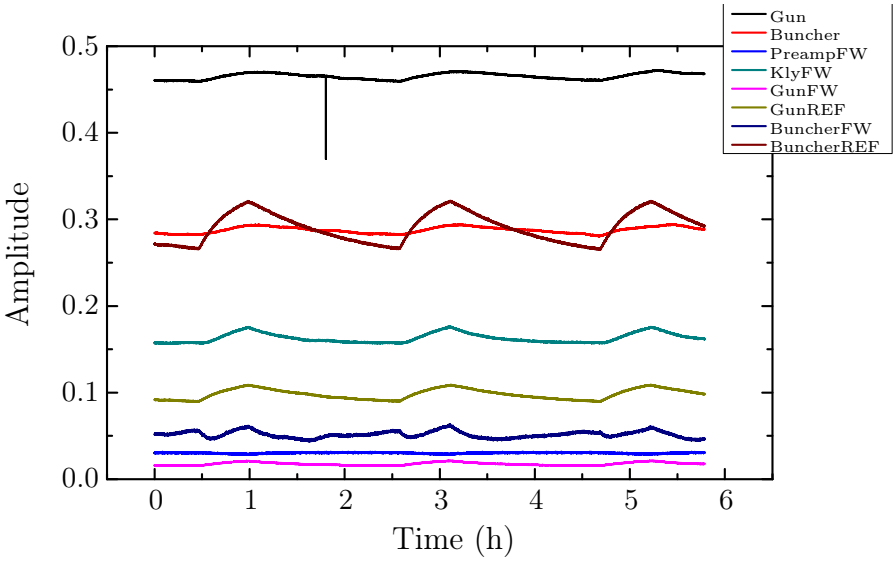

Figure 3.28: Recorded amplitude data from 02-May-2012 21:30:34 to 03-May-2012 08:39:40.

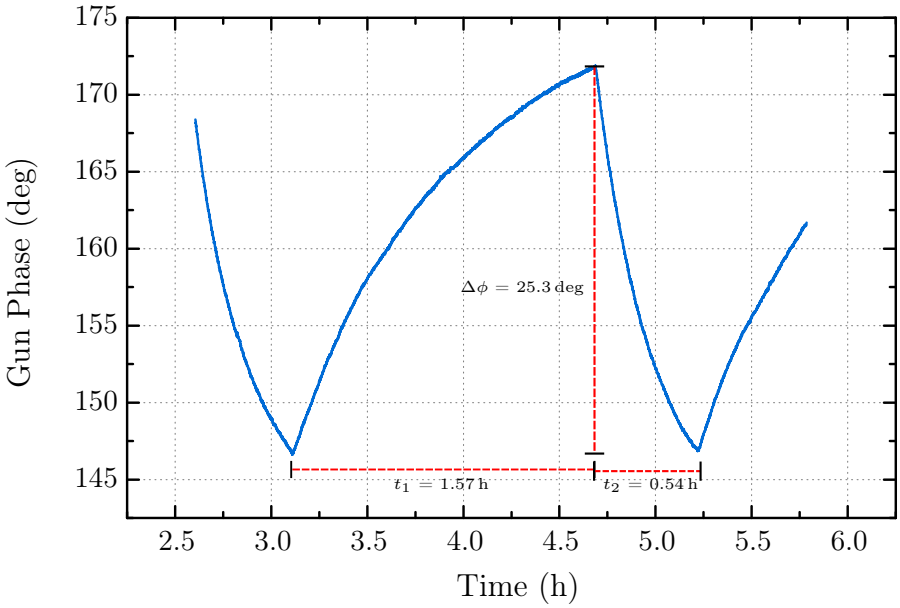

Figure 3.29: Detailed view of the gun phase signal measured via the probe antenna.

figure 3.29) reveals the shape of the periodic modulation. During the measurement the RF modulator shut itself down due to an interlock (see figure 3.30). The following data shows the evolution of the parameters after this interlock (full data range 02-May-2012 21:30:34 to 03-May-2012 08:39:40). It can be seen that the periodicity of the signal is still present for the preamplifier signals. For all other signals it is gone. From this it can be concluded that the periodicity originates from the preamplifier. The following measurements had been performed in order to investigate if this periodicity can be attributed to the temperature regulation inside of the RF rack, where the preamplifier is installed.

Measurement without RF Rack Temperature Regulation

In order to investigate the saw-tooth like periodic perturbation, another measurement had been conducted from 03-May-2012 21:31:43 to 04-May-2012 08:50:35. For this measurement the temperature regulation of the RF-rack had been disabled. During this period the machine had (again) not been used for other experiments and the setpoints for amplitude and phase were constant. Figures 3.31 and 3.32 show the recorded data for the different LLRF parameters. From the data it can be seen that the periodic modulation on both the phase and the amplitude signals is not present when the temperature regulation is switched off. This measurement shows the importance of correct temperature control in the RF rack.

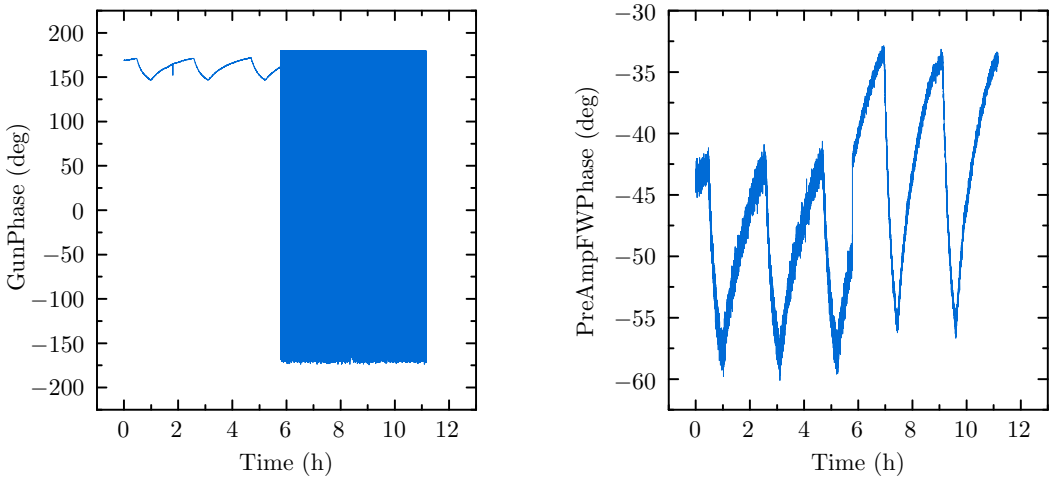

Figure 3.30: Recorded data from 02-May-2012 21:30:34 to 03-May-2012 08:39:40 for the gun phase and the preamplifier forward phase.

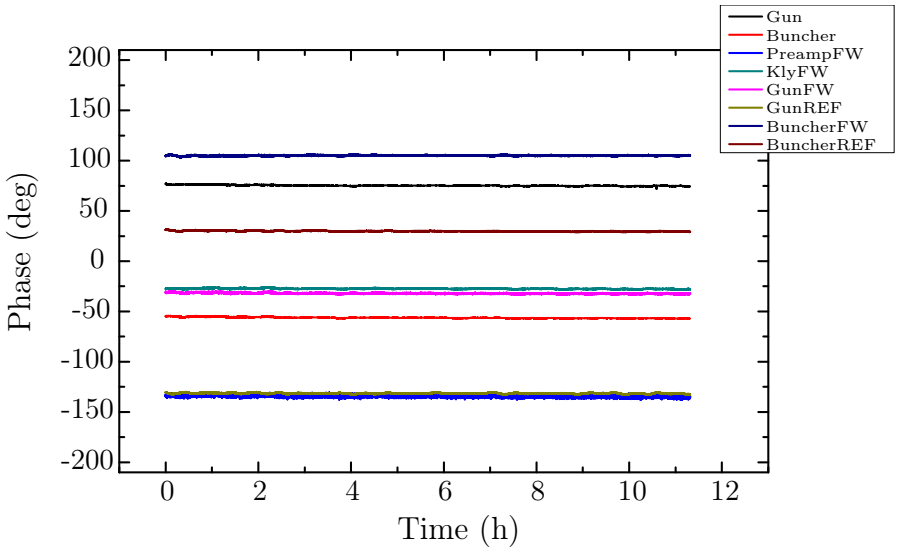

Figure 3.31: Recorded phase data from 03-May-2012 21:31:43 to 04-May-2012 08:50:35.

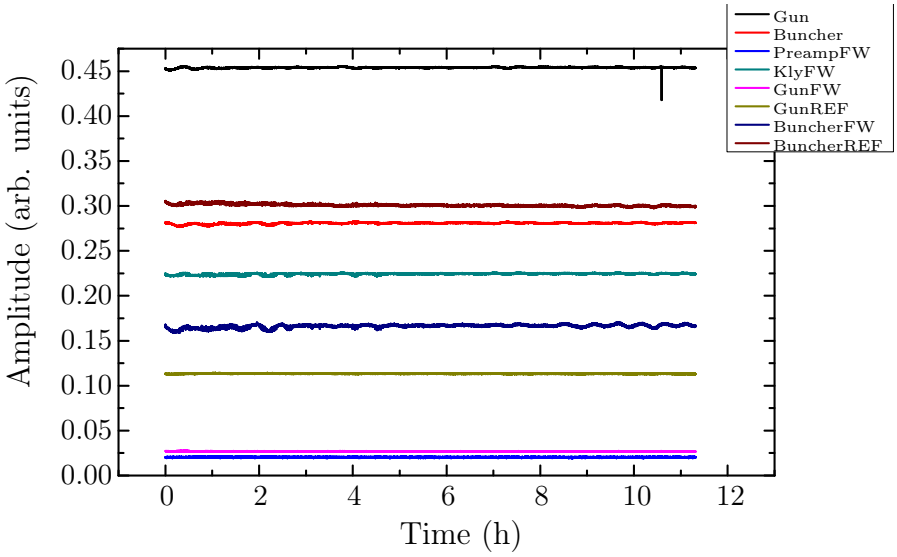

Figure 3.32: Recorded amplitude data from 03-May-2012 21:31:43 to 04-May-2012 08:50:35.

Klystron Voltage Stability

One of the most important factors for cavity field amplitude stability is the klystron voltage. In order to determine the amplitude stability limit given by the klystron voltage stability, the gun amplitude has been measured for different klystron voltage settings (see figure 3.33). The linear fit results in a slope of 0.23 $\frac{\mathrm{MV/m}}{\mathrm{V}}$. During the measurement from 03-May-2012 21:31:43 to 04-May-2012 08:50:35 the klystron voltage has been recorded. The result is a mean voltage of 859.84 V and a standard deviation of 0.02 V. This translates to an RMS amplitude jitter of $4.6 \cdot 10^{-3}$ MV/m, which in turn leads according to section 3.2.1 to a bunch time of flight jitter of 4.65 fs (gun cavity). This jitter value is much smaller than the ones caused by phase instability and can therefore be regarded as the lower limit for time of flight stability at REGAE.

46 Hour long Term Measurement with enabled LFF

Since the learning feedforward correction is mainly focused on reducing slow linear drifts of the phase and amplitude over the whole RF pulse, a 46 hour long term measurement has been conducted in order to determine possible residual linear drifts. To this end a measurement has been set up, where both the analogue feedback and the LFF had been enabled. Table 3.13 summarizes the results of the measurement for the gun phase and amplitude. The bunch time of flight (TOF)

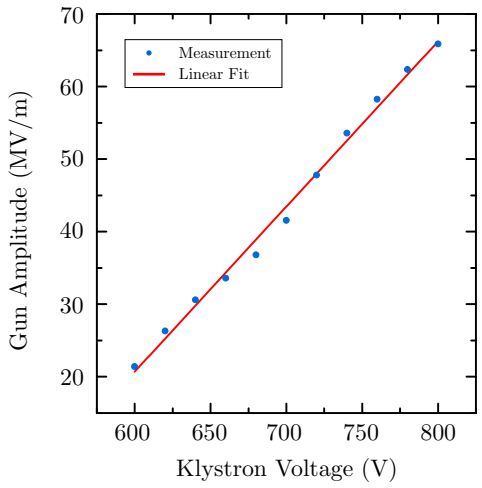

Figure 3.33: Measurement of the gun amplitude via the probe antenna for different klystron voltage settings. The linear fit reveals a slope of 0.23 $\frac{\mathrm{MV/m}}{\mathrm{V}}$.

RMS values have been estimated for the target chamber position ($z = 5.5\,\mathrm{m}$) using the theory shown in section 3.2.1 and assuming common phase jitter. It can be seen that the LFF indeed reduces the linear drifts very efficiently. The amplitude drifted only with a rate of $2.16 \cdot 10^{-3}$ percent of the initial amplitude per hour.

Concluding remarks

The long term measurements that have been discussed above lead to some interesting conclusions concerning stability at REGAE. First of all it has been shown that the cooling system for the LLRF components is a crucial factor for the overall stability of the important RF parameters. It has also been shown that the REGAE modulator offers extraordinary voltage stability even over $> 6\,h$ periods of time. The measured value of 4.65 fs RMS stability can be regarded as the lower limit of the time of flight stability at REGAE at the time of this thesis. The first learning feedforward implementation has also been put to the test via a 46 hour measure-

Table 3.13: Results for the 46 hour long term measurement from 21-September-2012.

	Linear Drift	RMSE	Estimated TOF RMSE
Gun phase	$-2.77 \cdot 10^{-4}\,\frac{\mathrm{deg}}{\mathrm{h}}$	0.046 deg	62.008 fs
Gun amplitude	$-1.13 \cdot 10^{-4}\,\frac{\mathrm{MV/m}}{\mathrm{h}}$	$0.039\,\frac{\mathrm{MV}}{\mathrm{m}}$	39.39 fs

ment, which showed that the LFF indeed almost eliminates phase and amplitude drifts. The bunch time of flight stability over 46 hours has been approximately 62 fs, which is given by the phase jitter contribution.

3.3.4 Some Remarks on the Learning Feedforward

It has been shown in the preceding sections that the learning feedforward — especially in conjunction with the analogue feedback — dramatically reduces the linear drifts on the gun phase. This is a very important result, but it comes with a cost. Since the only way the LFF can act on the machine is to adjust the I and Q (real and imaginary part) values of the klystron output signal, it becomes apparent that every such regulation also affects the buncher cavity. This can be best seen in the data from the 46 hour measurement presented in section 3.3.3. Figure 3.34 shows the difference between gun and buncher phase for this measurement. It can be seen that although the gun phase is practically locked, the buncher phase suffers from both external factors like temperature and in addition to that, the input signal adjustments of the LFF. This circumstance obviously poses a major problem, albeit the drifts occur on large timescales.

There are only two possibilities to cope with this problem. The first one is to establish an additional feedback, which acts on the phase shifter. This feedback will — due to the construction type of the phase shifter — only be able to reduce slow phase drifts. In addition to that the learning feedforward will have to be redesigned, since the phase shifter primarily acts on the gun phase (the phase shifter is installed on the gun arm of the RF system), which changes the LFF's reference phase. Although this approach can minimize phase drifts, the short term RMS stability of the buncher phase cannot be improved easily. Therefore the stability of the buncher phase will rely heavily on the stability of external factors like the cavity temperature. A second approach would be to introduce the LFF to the buncher cavity and the slow feedback to the gun cavity. This could be a sensible solution, since this thesis showed that the time of flight stability strongly depends on the stability of the buncher phase.

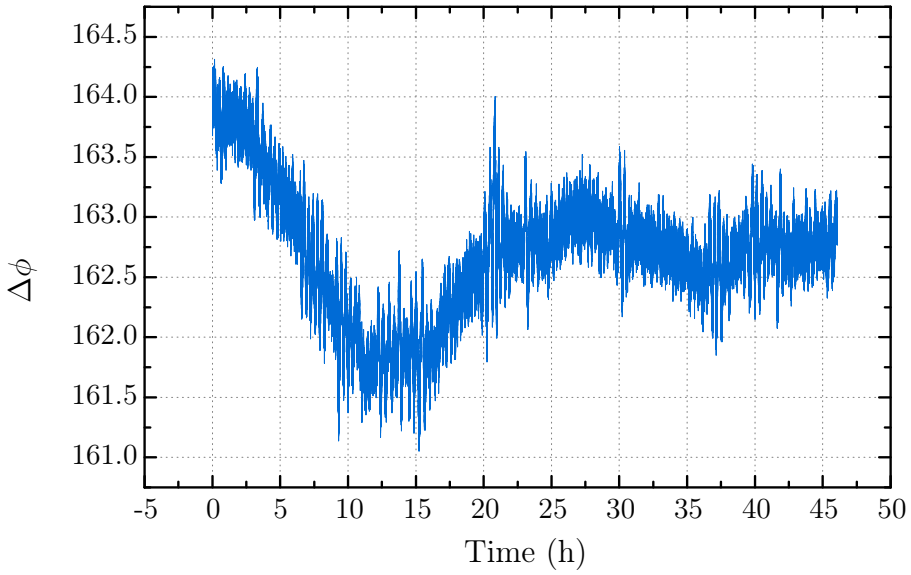

Figure 3.34: Difference between gun and buncher phase, measured over a period of 46 hours.

4

Conclusion and Outlook

In this thesis two main aspects of the REGAE machine have been discussed in detail. The first part focused on the high power RF system by first deriving the basic microwave circuit and resonator theory from first principles. In addition to that, CST simulations of the actual REGAE cavities have been presented and compared to measurements. Here it has been shown that in order to describe the exact mode structure of the highly optimized RF cavities, numerical calculations are necessary. This has been verified by comparison with actual measurements. Using the scattering matrix approach, an analytical model of the RF system, which includes a two arm phase shifter, has been derived and verified through comparison to phase shifter measurements at REGAE. Building on this theoretical model, the so called *Arbitrary Phase Tool* has been proposed and discussed. This tool could simplify the REGAE operation, by enabling the operators to adjust the cavity phases independently, making use of the theoretical model of the phase shifter system. Currently adjustment of the phases involves manual operation of the phase shifter motors and re-adjustment of the klystron phase. In the context of the arbitrary phase tool measurements of the reference phases for both the gun and the buncher cavity have been discussed. In order to be able to conduct these kind of measurements, a MATLAB tool has been implemented into the control system, which is now used in day-to-day operation for phase scan measurements. In the last part of the chapter, RF system characterization measurements for the — at the time of this thesis — current setup of the REGAE machine and the new *REGAE Gun Cavity II* have been presented and discussed. As part of this section the effect of the mode spacing on the REGAE RF pulses has been measured and theoretically described. From these measurements and calculations it can be seen

that in both cavities multiple modes are simultaneously excited. In this context the effect of the presence of multiple excited cavity modes on bunch parameters like energy spread and transverse emittance has been discussed. Although the mode spacing of the gun cavity is large enough (9.5 MHz), the relatively small mode spacing between the buncher π-mode and its adjacent mode (2 MHz) could affect the performance of the cavity in bunching mode. Fine tuning measurements via temperature scans have revealed the negative effect of the crosstalk between the cavities on the individual coupling coefficients. For the gun cavity the coupling is reduced by approximately 1 %, whereas for the buncher cavity approximately 10 %. This chapter — in conclusion — provides an extensive overview of the current REGAE high power RF system and provides a solution for the problem of arbitrary phase control during machine operation. It has also been shown that even though the RF system incorporates two cavities both fed by a single klystron, the behavior of the system can be described by the relatively simple scattering matrix approach.

The second part of this thesis focused on stability of several REGAE machine parameters at the time of this thesis, as well as a discussion of several sensitivity analysis methods. It has been discussed what kind of analysis methods might be feasible to apply to a system like REGAE. To this end a global sensitivity analysis based on a method as proposed by Saltelli et al. has been performed and discussed. Even though the results of the analyses provide insight into the importance and interplay of different input parameters, the studies revealed that the sheer amount of required model runs limits these techniques to small machines like REGAE. Shifting the focus on the phase stability, which plays a key role for both experiments that have been introduced in the introductory chapter, a theoretical description of the physics behind the actual acceleration process is given. Because of changes in the bunch time of flight between the two cavities, phase jitter compensation can occur. This has been verified using a Monte Carlo experiment based on the theoretical considerations. The results of the theoretical derivation can be used to estimate the bunch time of flight jitter due to phase and amplitude jitter in the cavities. Bunch time of flight stability, according to these calculations, mostly depends on the buncher phase stability. In addition to that, phase stability measurements based on the phase scan method have been presented and discussed. This way the current state of the machine in terms of phase stability has been evaluated. As part of this section, problems with the low level RF electronics have been discussed. The measurements reveal that the current phase stability using both the analogue feedback and the learning feedforward allows for a time of flight stability of approximately 50 fs right after the gun. 2D-cross-covariograms are used to show a strong correlation of the bunch

charge measurements with the cathode laser power during this measurement. As a conclusion of this chapter, the stability of the magnet power supplies, as well as long term RF parameter stability measurements have been presented. This way the dipole stability has been revealed to be insufficient for accurate energy and especially energy stability measurements. It has also been revealed that the beam pointing is affected by the operation of DESY II magnets. The long term measurements show that the learning feedforward effectively suppresses slow gun phase and amplitude drifts. Additional thoughts on the current implementation of the learning feedforward correction in the context of the RF system layout are also given. It is suggested to implement an additional feedback on the buncher cavity phase in the future.

All in all this thesis provides an extensive overview of the theory behind the RF system at REGAE (chapter 2). In addition to that, a way to cope with the problem of adjusting the cavity phases independently has been proposed. Characterization measurements have revealed the effect of the crosstalk between the cavities on coupling, pulse shape and the usage of the phase shifter. It can be concluded from the results presented in chapter 3 that the current state of the REGAE machine is close to design stability in terms of amplitude and phase stability for a single cavity. In order to be able to achieve this kind of stability at the target, additional modifications to the setup will be necessary.

Outlook

As it has been stated above, the phase stability of the REGAE machine is close to design stability for a single cavity. The second cavity — which is right now the buncher cavity — unfortunately suffers from long term drifts, which are caused by the overall phase drift in the system and in addition to that the regulation of the learning feedforward correction, which (currently) tries to minimize long term drifts on the gun phase and amplitude. Since the LFF acts on the klystron phase and amplitude, all regulation efforts also affect the other cavity. This problem needs to be addressed in the future by implementing a slow feedback on the phase shifter. The ideal implementation would be a feedback algorithm based on the analytical phase shifter model. In chapter 3 it has been shown that the overall time of flight stability mostly depends on the phase stability of the buncher cavity. Therefore is must be evaluated in the future, if the overall phase stability can be improved by applying the LFF to the buncher cavity signals. In order to further improve the phase stability measurements, a better readout system for the laser parameters needs to be included into the control system.

In terms of the RF system it must be further studied, whether the narrow mode

spacing between the buncher $2\pi/3-$ and π-mode has a negative effect on beam parameters like energy spread and emittance. This will be a crucial factor especially for the external injection experiment, where initial bunch parameters need be known as accurate as possible. In order to cope with the crosstalk between the cavities, it must be evaluated if the implementation of lossy elements or circulators into the waveguide system could mitigate this problem. Unfortunately — at the time of this thesis — circulators are not yet available for the REGAE high power RF system.

The next step in terms of the RF system following this thesis should be the implementation of the arbitrary phase tool, as proposed in chapter 2. In this context the analytical model for the phase shifter could also be further enhanced by implementing losses, etc.

As it has been stated above, the variance based sensitivity analysis techniques cannot be applied to more complex machines like FLASH, because the computation time is not feasible. Based on the results of this thesis however, it might be interesting to extend the scatter plot analysis to higher order polynomial fits. The results of the different orders could then be compared. This way it could be possible to apply this method to archived machine parameter data and to extract the mathematical dependence of output parameters on individual or sets of machine parameters. An analysis like this could then also be applied to more complex machines.

Bibliography

[1] A Saltelli. Making best use of model evaluations to compute sensitivity indices. *Computer Physics Communications*, 145(2):280–297, 2002.

[2] K Floettmann. Design and Performance of Printed Circuit Steering Magnets for the FLASH Injector. In *Proceedings of IPAC'10, Kyoto, Japan*, 2010.

[3] L Serafini and M Ferrario. Velocity bunching in photo-injectors. In *AIP Conf. Proc. 581*, pages 87–106, 2000.

[4] J Hirscht, D A Mazurenko, D Zhang, S Bayesteh, H Delsim-Hashemi, K Floettmann, M Huening, S Lederer, G Moriena, and R J D Miller. Relativistic electron gun for atomic exploration REGAE for femtosecond electron diffraction. In *1st CFEL symposium*, March 2011.

[5] H Delsim-Hashemi. Imaging Detector for Relativistic-Electron-Microscope REGAE. Technical Report 5, October 2012.

[6] J R Dwyer, C T Hebeisen, R Ernstorfer, M Harb, V B Deyirmenjian, R E Jordan, and R J Dwayne Miller. Femtosecond electron diffraction: 'making the molecular movie'. *Philosophical Transactions of the Royal Society A: Mathematical, Physical and Engineering Sciences*, 364(1840):741–778, March 2006.

[7] R Srinivasan, V A Lobastov, C Y Ruan, and A H Zewail. Ultrafast electron diffraction (UED). *Helvetica chimica acta*, 86(6):1761–1799, 2003.

[8] B Zeitler, M Schnepp, T Gehrke, M Hachmann, F Mayet, K Peters, F Grüner, J Grebenyuk, T Mehrling, J Osterhoff, and K Floettmann. Merging Conventional and Plasma Accelerators. In *Annual LAP Meeting*, September 2012.

[9] Microwave Studio. Version 2012.06. CST AG, Darmstadt, Germany, 2012. `http://www.cst.com`.

[10] J D Jackson. *Classical Electrodynamics*. John Wiley & Sons, 3 edition, December 1998.

[11] D L Hall. A review of the equivalent circuit model of RF accelerating cavities in the context of an analysis of the 1.3 and 3.9 GHz cavities at FLASH. Master's thesis, University of Manchester.

[12] K Floettmann. *Beam Dynamics in RF Guns and Injectors (Draft Version 25.01.11)*. January 2011.

[13] P Tenenbaum. Field in Waveguides - a Guide for Pedestrians (DRAFT June 13, 2003), June 2002.

[14] D E Nagle. Coupled Resonator Model for Standing Wave Accelerator Tanks. *Review of Scientific Instruments*, 38(11):1583, 1967.

[15] H Wiedemann. *Particle Accelerator Physics*. Springer Verlag, 2003.

[16] J H Han and K Floettmann. Half cell length optimization of photocathode RF Gun. In *Proceedings of ERL07, Daresbury, UK*, page 70, 2007.

[17] H Meinke and F W Gundlach. *Taschenbuch der Hochfrequenztechnik*. Springer, 5 edition, October 1992.

[18] J Frei, Xiao-Ding Cai, and S Muller. Multiport S-Parameter and T-Parameter Conversion With Symmetry Extension. *IEEE Transactions on Microwave Theory and Techniques*, 56(11):2493–2504.

[19] MATLAB. Version 7.12.0 (R2012a). The Mathworks Inc., Natick, Massachusetts. `http://www.mathworks.com`.

[20] M Hachmann. Transverse emittance measurement at REGAE via a solenoid scan (in preparation). Master's thesis, Universtät Hamburg.

[21] A Space Charge Tracking Algorithm. Version 3.0. K Floettmann. `http://www.desy.de/~mpyflo/`.

[22] M Bellaveglia, D Alesini, M Ferrario, and A Gallo. An RF gun pulse shaping system to increase the accelerating gradient. Technical Report RF-12/001, 2011.

[23] S Lidia, G Penco, and M Trovo. Technical Design and Optimization Study for the FERMI@Elettra FEL Photoinjector. Technical Report ST/F-TN-06/11, 2006.

[24] J F Schmerge, J Castro, J E Clendenin, D H Dowell, S M Gierman, and others. The S-Band 1.6 Cell RF Gun Correlated Energy Spread Dependence on pi and 0 Mode Relative Amplitude. *Int.J.Mod.Phys.*, A22:4061–4068, 2007.

[25] D Limborg-Deprey, L Xiao, D H Dowell, and J F Schmerge. Modifications on RF Components in the LCLS Injector. In *Proceedings of 2005 Particle Accelerator Conference*, pages 1–3, October 2005.

[26] K Floettmann. Personal Communication. October 2012.

[27] M Dohlus, V Kaljuzhny, and S G Wipf. Resonance frequencies and Q-factors of multi-resonance complex electromagnetic systems. Technical Report TESLA2002-12, 2002.

[28] A Brandt, P Pucyk, and S Simrock. Field estimation and signal calibration of RF guns without field probe. Technical Report FEL2007-01, 2007.

[29] T Schilcher. *Vector Sum Control of Pulsed Accelerating Fields in Lorentz Force Detuned Superconducting Cavities*. PhD thesis, Universität Hamburg, October 1998.

[30] V Pratt. Direct least-squares fitting of algebraic surfaces. *ACM SIGGRAPH Computer Graphics*, 21(4):145–152, 1987.

[31] L C Maier and J C Slater. Field Strength Measurements in Resonant Cavities. *Journal of Applied Physics*, 23(1):68, 1952.

[32] F Caspers and G Dôme. Precise perturbation measurements of resonant cavities and higher order mode identification. In *CERN SPS/85-46 (ARF)*. CERNSPS, 1985.

[33] A Saltelli, T Andres, and M Ratto. *Global Sensitivity Analysis: The Primer*. Wiley, Chichester, 2008.

[34] I M Sobol. Sensitivity Estimates for Nonlinear Mathematical Models. *Mathematical Modelling and Computational Experiment 1, 407–414*, October 1993.

[35] I M Sobol. Global sensitivity indices for nonlinear mathematical models and their Monte Carlo estimates. *Mathematics and computers in simulation*, 55(1-3):271–280, 2001.

[36] A B Owen. Better estimation of small Sobol' sensitivity indices. Technical Report 2012-06, April 2012.

[37] A Saltelli, T H Andres, and T Homma. Some new techniques in sensitivity analysis of model output. *Comput. Statist. Data Anal. 15*, pages 211–238, October 1993.

[38] J H Han and K Floettmann. Half cell length optimization of photocathode RF gun. In *Proceedings of ERL07, Daresbury, UK*, 2007.

[39] H Schlarb, N Heidbrook, H Kapitza, F Ludwig, and N Nagad. Precision RF gun phase monitor system for FLASH. In *EPAC 2006*.

[40] W Schottky. Über kalte und warme Elektronenentladungen. *Zeitschrift für Physik A Hadrons and Nuclei*, 14(1):63–106, 1923.

[41] J H Han. *Dynamics of Electron Beam and Dark Current in Photocathode RF Guns*. PhD thesis, Universität Hamburg.

[42] TINE. Version 4.3.2. DESY, Hamburg, Germany. `http://tine.desy.de`.

[43] H Delsim-Hashemi. Personal Communication. September 2012.

[44] T Gehrke. Design and characterization of permanent-magnetic solenoids at REGAE (in preparation). Master's thesis, Universität Hamburg.

[45] S Jolly. Focusing Properties of a Solenoid Magnet. In *UKNFIC Meeting 21/05/05*, pages 1–17, May 2005.

[46] V Kumar. Understanding the focusing of charged particle beams in a solenoid magnetic field. *American Journal of Physics*, 77(8):737, 2009.

[47] J Rossbach and P Schmüser. Basic Course on Accelerator Optics, September 2004. `http://adweb.desy.de/~rossbach/uni/cern.pdf`, last access: 28.10.2012.

Acknowledgments

First of all I would like to express my sincere gratitude to Klaus Flöttmann, who made this thesis possible by giving me the opportunity to work on a project like REGAE and also for being able to help me with almost every aspect of this thesis. I also like to thank Max Hachmann for a lot of fun measurement shifts at REGAE, as well as interesting discussions. Without the great work by Hossein Delsim-Hashemi and Shima Bayesteh on the diagnostics part of REGAE this thesis would not have been possible. The same is true for the Dongfang Zhang, who always kept the laser in sync and running during my measurements. Last but certainly not least I would like to thank Matthias Hoffmann and the MSK group for their help concerning the LLRF system.

Erklärung

Hiermit bestätige ich, dass die vorliegende Arbeit von mir selbständig verfasst wurde und ich keine anderen als die angegebenen Hilfsmittel — insbesondere keine im Quellenverzeichnis nicht benannten Internet-Quellen — benutzt habe und die Arbeit von mir vorher nicht einem anderen Prüfungsverfahren eingereicht wurde. Die eingereichte schriftliche Fassung entspricht der auf dem elektronischen Speichermedium. Ich bin damit einverstanden, dass die Masterarbeit veröffentlicht wird.

Ort, Datum	Unterschrift